NASA Contractor Report 180807

Thermal Barrier Coating Life Prediction Model Development

Final Report

R.V. Hillery, B.H. Pilsner, R.L. McKnight,
T.S. Cook, and M.S. Hartle
GE Aircraft Engines
Cincinnati, Ohio 45215

November 1988

Prepared for
Lewis Research Center
Under Contract NAS3-23493

NASA

National Aeronautics and
Space Administration

NASA CR 180807

R87AEB586

National Aeronautics and
Space Administration

THERMAL BARRIER COATING LIFE PREDICTION MODEL DEVELOPMENT

FINAL REPORT

FOREWORD

This is the Final Report covering the activities performed under NASA Contract NAS3-23943, "Thermal Barrier Coating Life Prediction Model Development." It was prepared by the Engineering Materials Technology Laboratories (EMTL) of GE Aircraft Engines, Cincinnati, Ohio. Dr. R.V. Hillery was the General Electric Program Manager and Mr. B.H. Pilsner was the Principal Investigator.

Dr. R.L. McKnight, Mr. T.S. Cook, and Mr. M.S. Hartle, in addition to conducting the model development effort described in Section 4.0 of this report, also performed finite element analyses and thermomechanical experiments. Dr. J.A. Nesbitt was the Project Manager for NASA Lewis Research Center.

Table of Contents

Table of Contents (Concluded)

List of Illustrations

List of Illustrations (Continued)

List of Illustrations (Continued)

List of Illustrations (Continued)

List of Illustrations (Concluded)

List of Tables

1.0 SUMMARY

This report describes the work performed on a program to determine the predominant modes of degradation of a plasma-sprayed thermal barrier coating (TBC) system and to develop and verify life prediction models accounting for these degradation modes. The primary TBC system consisted of a low pressure plasma-sprayed NiCrAlY bond coat, an air plasma-sprayed ZrO_2-Y_2O_3 top coat, and a René 80 substrate. The work was divided into three technical tasks.

It was established through a literature survey and through past experience that the primary failure mode that needed to be addressed was loss of the zirconia layer through spalling. Experiments were performed which showed that oxidation of the bond coat is a significant contributor to coating failure. It was evident from the test results that the species of oxide scale that is initially formed on the bond coat plays an instrumental role in coating degradation and failure. It was also shown that elevated temperature creep of the bond coat plays a role in coating failure.

Also as a part of the first task, several key properties of the bond coat and top coat were measured. These included tensile strength, elastic modulus, Poisson's ratio, and coefficient of thermal expansion. An empirical model was developed for predicting the test life of specimens with selected coating, specimen, and test condition variations.

In the second task, a coating life prediction model was developed based on the data from Task I experiments, results from thermomechanical experiments performed as part of Task II, and finite element analyses of the TBC system during thermal cycles. Both time-independent plastic flow and time-dependent creep deformation were included in the analyses. An inference method was used in the development of the model since the processes involved in TBC failure are not generally directly observable.

The effort in the third and final task attempted to verify the validity of the model developed in Task II. This was done by using the model to predict the test lives of several coating variations and specimen geometries, then comparing these predicted lives to experimentally determined test lives. It was found that the model correctly predicts trends, but that additional refinement is needed to accurately predict coating life.

2.0 INTRODUCTION

The objectives of this program were to determine the predominant modes of degradation of a plasma-sprayed thermal barrier coating system and to develop and verify life prediction models accounting for these degradation modes. The program was planned to be completed in two phases, each consisting of several tasks.

The work in Phase I was aimed at identifying the relative importance of the various failure modes for the selected thermal barrier coating system, and developing and verifying a life prediction model for the predominant mode. The TBC system consisted of a low pressure plasma-sprayed (LPPS) Ni-22Cr-10Al-0.3Y bond coat (0.13 mm thick) and a plasma-sprayed ZrO_2-8%Y_2O_3 top coat (0.25 mm thick) on conventionally-cast René 80 alloy substrate. Task I identified the relative importance of the various failure modes for the baseline coating system through the design and performance of a series of experiments. Preliminary models were developed and evaluated. Task I also included determination of several key properties of the coating materials such as tensile strength, Poisson's ratio, dynamic modulus, and coefficient of thermal expansion.

In Task II, life prediction models for the predominant failure modes were developed. This was accomplished by performing finite element analyses and thermomechanical fatigue experiments, thus creating a life prediction model by means of a combined analytical and experimental program.

These models were verified in Task III through a series of tests and analyses. The results obtained from this task provide a better understanding of the behavior of TBC systems and the suitability of the developed models. This understanding was used to formulate recommendations for further research required to arrive at a fully satisfactory engine life prediction methodology.

The work planned for Phase II would develop design-capable, causal, life prediction models for thermomechanical and thermochemical failure modes, and for the exceptional conditions of foreign object damage and erosion. The integration of appropriate combinations of models into a comprehensive life prediction model would be accomplished and the integrated model would be exercised through a combination of critical tests and analyses to determine its applicability and accuracy.

This report describes the work performed on the first phase of this project.

3.0 TASK I - FAILURE MECHANISM DETERMINATION

The objective of this task was to experimentally and analytically identify the relative importance of the various degradation and failure modes of the selected TBC system. First, a literature search was performed to assess the available knowledge on potential failure mechanisms of plasma-sprayed TBC systems and how bond coat and top coat modifications affect these failure mechanisms. Spalling of the ceramic layer was considered the primary problem to be addressed; therefore, initial Task I efforts were directed at evaluating failure mechanisms associated with spallation.

3.1 Literature Review

Generally, state-of-the-art thermal barrier coatings utilize two-layer coating systems. The systems consist of MCrAlX (M = Ni or Co or both; X = Hf, Zr, or Y) bond coats and ZrO_2-Y_2O_3 top coats. Three-layer systems have been investigated, (1,2) where an extra layer of "graded" bond coat and top coat material is incorporated between the bond coat and the top coat (to reduce the effect of thermal expansion mismatch). However, these three-layer systems have resulted in a shorter thermal cycle life than two-layer systems (2). The shorter life is associated with significant oxidation of the metallic bond coat material in the graded layer resulting from larger bond coat material surface area. Numerous studies have also shown that the composition and physical characteristics of both the bond coat and top coat are extremely important in determining thermal cycle life.

3.1.1 Bond Coating

The primary role of the bond coat in a TBC system is to provide good adhesion between the metal substrate and the ceramic top coat, while providing good oxidation protection to the underlying substrate alloy. Numerous studies have demonstrated that oxidation of the bond coat can significantly affect spalling (3-6). For this reason, bond coat compositions have evolved from early Ni-Cr and Ni-Al compositions to the currently used MCrAlX compositions. Similarly, dense and more oxidation-resistant (lower levels of internal oxidation) bond coat layers produced by the low pressure plasma spray (LPPS) process have been shown to have longer thermal cycle life than porous air plasma-sprayed bond coat layers of the same chemical composition (1, 7). Hence, both chemical and processing changes have resulted in TBCs with longer thermal cycle lives.

Small changes in bond coat composition can also strongly affect thermal cycle life. Studies by Stecura have shown that the presence of small quantities of yttrium (0.1-1.0 wt.%) in the bond coat are critical (3). His studies indicate that TBC systems that utilize bond coats without yttrium fail very rapidly. Investigations have also shown that critical levels of Cr and Al are necessary to produce TBCs with long lives (3, 8). The same holds true for bond coat thickness, where a certain minimum thickness is required (3, 8). In all cases, changes to the bond coat have been linked primarily to improving the oxidation resistance of that layer.

Several studies have been aimed at evaluating the effects of bond coat oxidation and developing models based on oxidation as a primary TBC failure mechanism (9-11). In one study, Miller noted similar weight gains (due to oxidation) at failure of specimens with a $CaSiO_4$/MCrAlY TBC regardless of test temperature (9). Miller has also developed models based on thermal cycle and oxidation data (9, 11). His work has been based primarily on air plasma-sprayed bond coats, but more recent work has shown that these models are applicable to LPPS bond coats (10). One model held that oxidation strains are similar to thermal expansion mismatch strain (10). Thus, the strains of oxidation and the strains developed by thermal expansion mismatch are additive, and failure occurs once a certain total strain level is reached.

There is evidence that stronger bond coat alloys can extend the thermal cycle life of TBC systems (12). TBCs with bond coat compositions of NiCrAlYZrB and NiCrAlYTaC (compositions based on NiCrAlY with additional grain boundary and solid-solution strengthening elements) had longer lives in thermal cycle testing than the conventional NiCrAlY bond coat. Two additional bond coats with different creep strength were tested, and again, higher thermal cycle life was observed for the TBC system with the higher bond coat creep strength.

Bonding between the bond coat and ceramic layer of plasma-sprayed TBCs is largely mechanical, and the roughness of the bond coat is critical to keeping the ceramic layer attached (7). Therefore, the bond coat powder size and spray parameters must be adjusted to produce bond coat surfaces that have significant levels of surface roughness. However, care must be taken so that higher levels of porosity do not develop in the bond coat which would reduce its oxidation resistance.

3.1.2 Top Coatings

State-of-the-art TBC's generally utilize ZrO_2 top coatings that have been partially stabilized with Y_2O_3 (13, 14). Recent investigations have shown that the optimum content is 6-8 w/o Y_2O_3 (15). Long thermal cycle lives have been obtained when these yttria-partially-stabilized zirconia TBCs contain a large amount of the tetragonal phase, small but not zero (approximately 5%) monoclinic phase, and little or none of the cubic phase (16, 17). Stecura also noted that when no monoclinic zirconia phase was present and/or free yttria was present in yttria-stabilized zirconia containing 12% Y_2O_3 or more, the TBC fails rapidly (15). Unfortunately, little is known on how top coat phase changes actually affect thermal cycle life. Although, zirconia can be toughened by phase transformations (18, 19), it is doubtful that plasma-sprayed zirconia is toughened since it has been shown that grinding of the yttria-partially-stabilized zirconia into a powder did not cause a significant amount of metastable tetragonal to transform to monoclinic (20). Also, fracture toughness was found to be rather insensitive to aging treatments (20).

The characteristics of the top coat powder can significantly affect thermal cycle life. In one study (21), nine different ZrO_2-8%Y_2O_3 top coat powders produced by various processes (spray-dried, sintered, etc.) were applied to TBC specimens and tested in a thermal cycle test under identical conditions. The thermal cycle life for these specimens ranged from 40 to

1000 cycles. These results demonstrate the importance of differences resulting from changes in top coat powder processing.

The levels of porosity and microcracking in the top coat can strongly affect thermal cycle life (22-24). Studies utilizing acoustic emission techniques have indicated that significant levels of microcracking, resulting from thermal expansion mismatch, occur during the first few thermal cycles of testing of zirconia TBCs (25). It is believed that a ceramic coating that exhibits a high density of microcracking can better accommodate the differences in thermal expansion. Thus, the differences in thermal expansion are relieved by either the degree of plastic deformation or microcracking (26). Also, by decreasing top coat density, and thus hardness, the thermal shock resistance is enhanced with a concurrent increase in critical quench temperature *(23). In these cases, controlled porosity and microcrack levels increase the toughness of the ceramic (24).

3.1.3 Bond Coat/Top Coat Interface

Generally, most authors have associated TBC failure with the development of compressive stresses that occur in the ceramic layer during cooling (5, 27). These stresses can be attributed to the thermal expansion mismatch between the ceramic top coat and metal bond coat (23, 26, 28, 29). However, these stresses may also be developed by plastic anisotropy and thermal gradients introduced into the ceramic during plasma spraying (21). The importance of the stress has been shown by correlating TBC behavior to the substrate temperature during application of the top coat. By utilizing lower substrate temperatures, longer thermal cycle lives have been achieved (30, 31).

Most TBC system failures appear to originate with the formation of a crack or cracks within the ceramic with failure occurring in the ceramic near the bond coat/top coat interface (17, 27). Analysis has indicated that, due to the development of temperature gradients in the ceramic, a state of biaxial compression and radial tension develops in the ceramic (5). This analysis also indicates that cooling stresses are more compressive at the bond coat/top coat interface and diminish toward the surface. Thus, failure can be attributed to the high stress state at this interface. As indicated, this higher stress state at this interface is primarily due to the thermal expansion mismatch which is probably affected by bond coat oxidation of the roughened bond coat surface.

3.1.4 Temperature and Thermal Cycle Duration

Higher temperatures and more rapid thermal cycling result in shorter TBC lives (5, 27).Stress calculations and experiments have indicated that repeatedly subjecting ceramic coatings to high rates of heating and cooling has a more destructive influence on coating life

*In this study (23), the effect of zirconia coating density on thermal shock resistance was evaluated by rapidly quenching the coating into a water bath. The critical quench temperature was defined as the temperature required to cause coating failure or a large drop in coating hardness when quenched into the water bath.

than isothermal exposure at temperature (27). Higher substrate temperatures dramatically decrease thermal cycle life. This can be attributed to higher oxidation rates, larger Δ Ts (the differences between maximum and minimum substrate temperature during a thermal cycle which create larger stresses due to thermal expansion mismatch), and increased rates of other thermomechanical and thermochemical processes (such as interdiffusion, sintering, and corrosion).

3.1.5 Other Thermochemical Processes

Other thermochemical factors which can potentially affect TBC life include sintering of the ceramic layer and interdiffusion between the bond coat and substrate. Because the plasma-sprayed zirconia layer consists of large particles (splats) and relatively large pores, shrinkage forces due to sintering are probably small. The more likely effect of sintering on TBC behavior is that which results from increased interparticle cohesion which, while increasing the strength of the ceramic layer (positive factor), may also reduce its strain tolerance (negative factor).

Interdiffusion of bond coat and substrate elements at elevated temperature does occur and has been documented (32), but the effect of such interdiffusion on TBC failure is not well defined. Clearly, the loss of aluminum from the bond coat by diffusion into the substrate can alter the oxidation behavior of the bond coat and in the extreme may lead to the formation of less adherent oxide species. Changing the composition of the bond coat layer and outer surface of the substrate through interdiffusion may also alter their physical and mechanical properties, and thus influence TBC behavior.

Corrosion of the bond coat, another thermochemical effect, can also lead to TBC failure. Corrosive attack of TBCs has not generally been a problem in aircraft engines, but can be a significant problem in marine and industrial applications. An additional mode of failure in corrosive environments is condensation of corrodant species in the pores of the ceramic layer, where it can do mechanical damage resulting from thermal expansion mismatch and/or volume changes associated with phase changes in the condensate. Corrosive environments containing Na and V have also been observed to leach Y from yttria-stabilized zirconia leading to failure resulting from destabilization of the zirconia (33, 34). Reducing access of corrodants by partially sealing the surface of the zirconia coating by laser glazing has been shown to extend the life of TBCs in corrosive test environments (31), and the use of CeO_2 stabilized ZrO_2 has reduced destabilization in V containing environments (32).

3.1.6 Other Failure Modes

Although spallation of the ceramic layer is the primary mode of TBC failure in current applications, erosion and impact damage are also important and potentially life-limiting causes for TBC degradation in engine environments. Loss of some of the ceramic layer by erosion has been observed in several engine tests of TBCs, particularly on the outer bands of HPT nozzles. A plasma-sprayed ceramic layer of ZrO_2-Y_2O_3 has relatively low erosion resistance due to its unique structure and large amount (10% to 15%) of porosity, the same features that

contribute to its ability to withstand thermal strain. It has been demonstrated that fusing the top few mils of the surface of the zirconia layer by a laser glazing process can increase the erosion resistance by a factor of 8 or more (31). Since only the outer few mils of coating are fused, the bulk of the zirconia layer retains the original strain tolerance (Cf. sintering effects discussed above).

3.1.7 Summary

It is apparent from the above that failure of TBCs can be related to and influenced by a large number of factors. It was concluded from this survey that the primary failure mode of interest is loss of the ceramic layer by spalling and that many factors contribute to this loss. Among the more important factors which contribute to stress in the coating layers, and thus to coating failure, are the significant differences in the coefficients of thermal expansion of the zirconia layer and the underlying bond coat and substrate, and the growth of oxide scale on the bond coat at its interface with the zirconia layer. It is commonly believed that the spalling occurs during cooling as a result of compressive (buckling) stress in the zirconia layer. Another factor thought to have significant effect on coating life is stress relaxation via creep at service temperature, which results in higher compressive stress in the zirconia layer during cooling. Other factors which may play roles in coating failure include coating microstructure, composition, inherent strength, and residual stress.

3.2 Experimental Procedures

The baseline system in this effort consisted of a low pressure plasma-sprayed (LPPS) Ni-22Cr-10A1-0.3Y (wt. %) bond coat and an air plasma-sprayed (APS) yttria partially stabilized zirconia (ZrO_2-8 wt% Y_2O_3) top coat on conventionally cast René 80 alloy substrate*. Bond coat thickness was 0.13 mm (0.005 inch), and zirconia thickness was 0.25 mm (0.010 inch).

3.2.1 Specimen Preparation

Two types of specimens were used in the Task I efforts. One was a tube specimen (Figure 1) which simulates the curvature of engine components, and the second was a button specimen (Figure 2) which has become a standard test specimen at GE for evaluating TBCs. The specimens were given the standard René 80 solution heat treatment [1204°C (2200°F) for 2 hours, followed by 1093°C (2000°F) for 4 hours, both in vacuum] and the substrate surface was then grit blasted and vapor honed prior to application of the bond coat. The bond coat was applied on four tube specimens at a time using a planetary holder, and was applied on 35 button specimens at a time using a rotating drum. Both types of specimens were coated in an automated LPPS system. A bond coat powder size of -230 + 400 mesh (see Appendix A for powder characteristics) was used
to produce surface roughnesses greater than 400 μin Ra** (necessary to produce good bond coat/top coat bonding). Next, the bond-coated specimens were cleaned in acetone. Tube

* Ni-14Cr - 9.5Co - 5Ti - 4W - 4Mo - 3Al - 0.17C - 0.03Zr - 0.015B.
**Ra is the average peak and valley height of the surface.

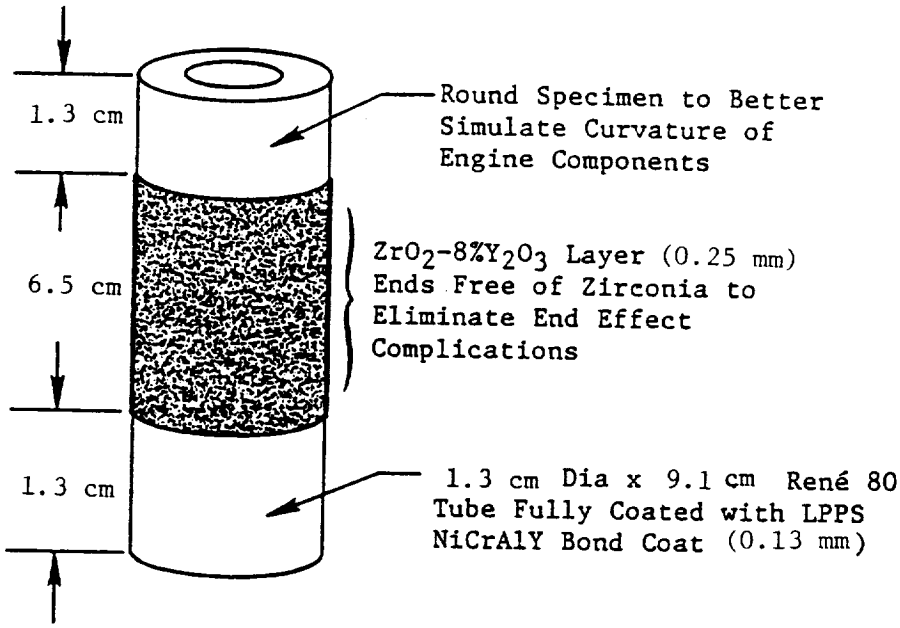

a. Test Specimen Configuration

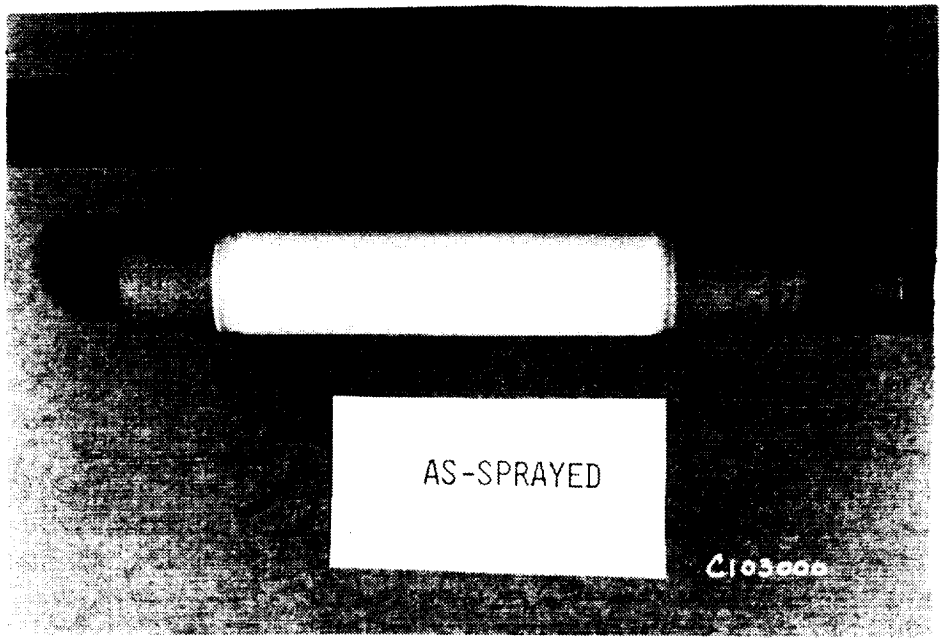

b. As-Sprayed Specimen

Figure 1. Thermal Barrier Coated Tubular Specimen.

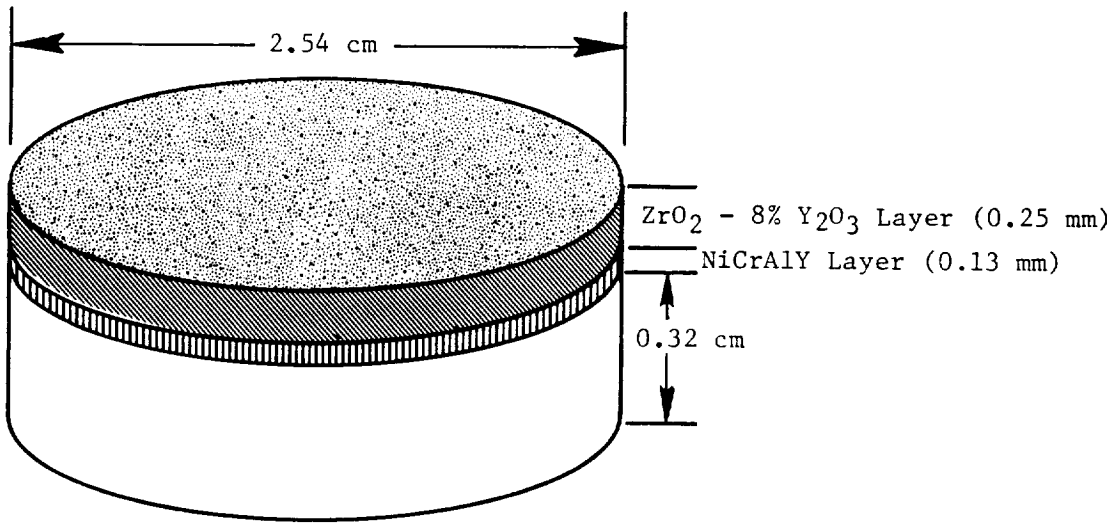

a. Test Specimen Configuration

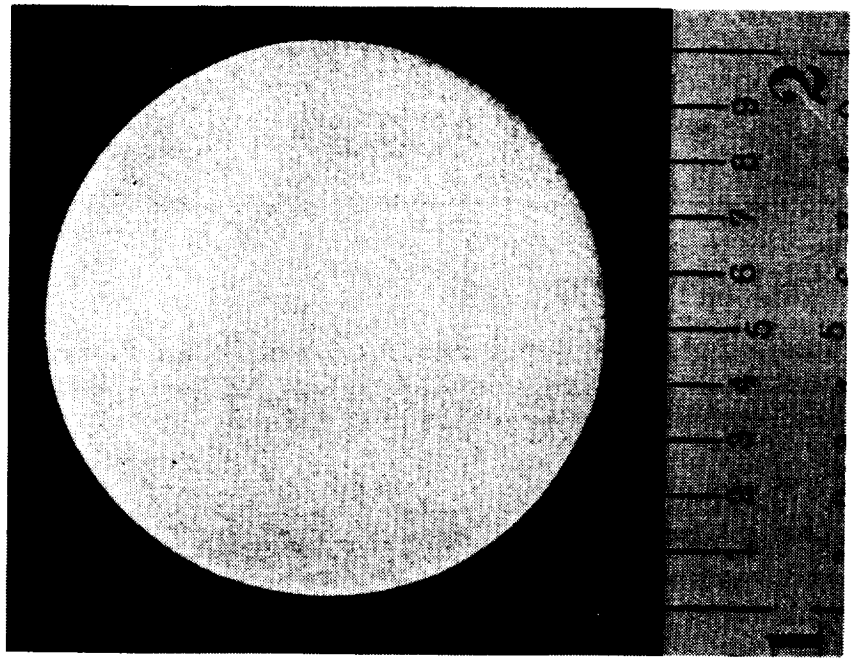

b. As-Sprayed Specimen

Figure 2. Thermal Barrier Coated Button Specimen.

specimens were also shadow masked prior to the top coat application to produce a tapered edge (Figure 3) on the zirconia coating layer. The top coat was applied to each tube specimen individually using a robot and a Metco Computerized Plasma Process Controller Spray System. The robot controlled the plasma torch manipulations, while the Metco system controlled the spray parameters. The top coat was deposited on up to 100 button specimens simultaneously using a semiautomated Metco APS System. The spray parameters used for both the bond coat and top coat are listed in Table I. The microstructure of the resultant TBC System is shown in Figure 4.

Table I. Plasma Spray Parameters

	APS	LPPS
Plasma Gun	Metco 7MB	Metco 7MB
Primary/Secondary Gas	N_2/H_2	Ar/H_2
Gun Power	36 kw	50 kw
Powder Feed Rate	6 lb/hr	5 lb/hr
Preheat	---	1800°F
Spray Distance	5 in.	12 in.
Other	90° air impingement, and center of tube cooling.	$A1_2O_3$ grit blast and vapor hone cleaning

3.2.2 Thermal Cycle Testing

Two types of thermal cycle tests were utilized in the Task I effort. The majority of the testing to identify failure mechanisms was a furnace cycle test. Another type of test that was used to a lesser degree for the same purpose was the JETS test.

Furnace Cycle Test

Furnace cycle testing was accomplished in a programmable, microprocessor-controlled, rapid-heating furnace with $MoSi_2$ heating elements (Figure 5a). Up to 36 tubular specimens or up to 60 button specimens were cycled simultaneously in the furnace. The thermal cycle, shown in Figure 5b, was approximately 70 minutes long; it consisted of approximately 10 minutes heat up, 45 minutes at a test temperature of 1093°C (2000°F), and 15 minutes forced-air cooling. Tube specimens were removed from the test after every fifth cycle and visually examined for evidence of cracking and loss of the zirconia layer. Button specimens were examined after every 20 cycles. Each specimen was removed from test when 10% (surface area) of the zirconia layer had spalled. Selected specimens were evaluated metallographically.

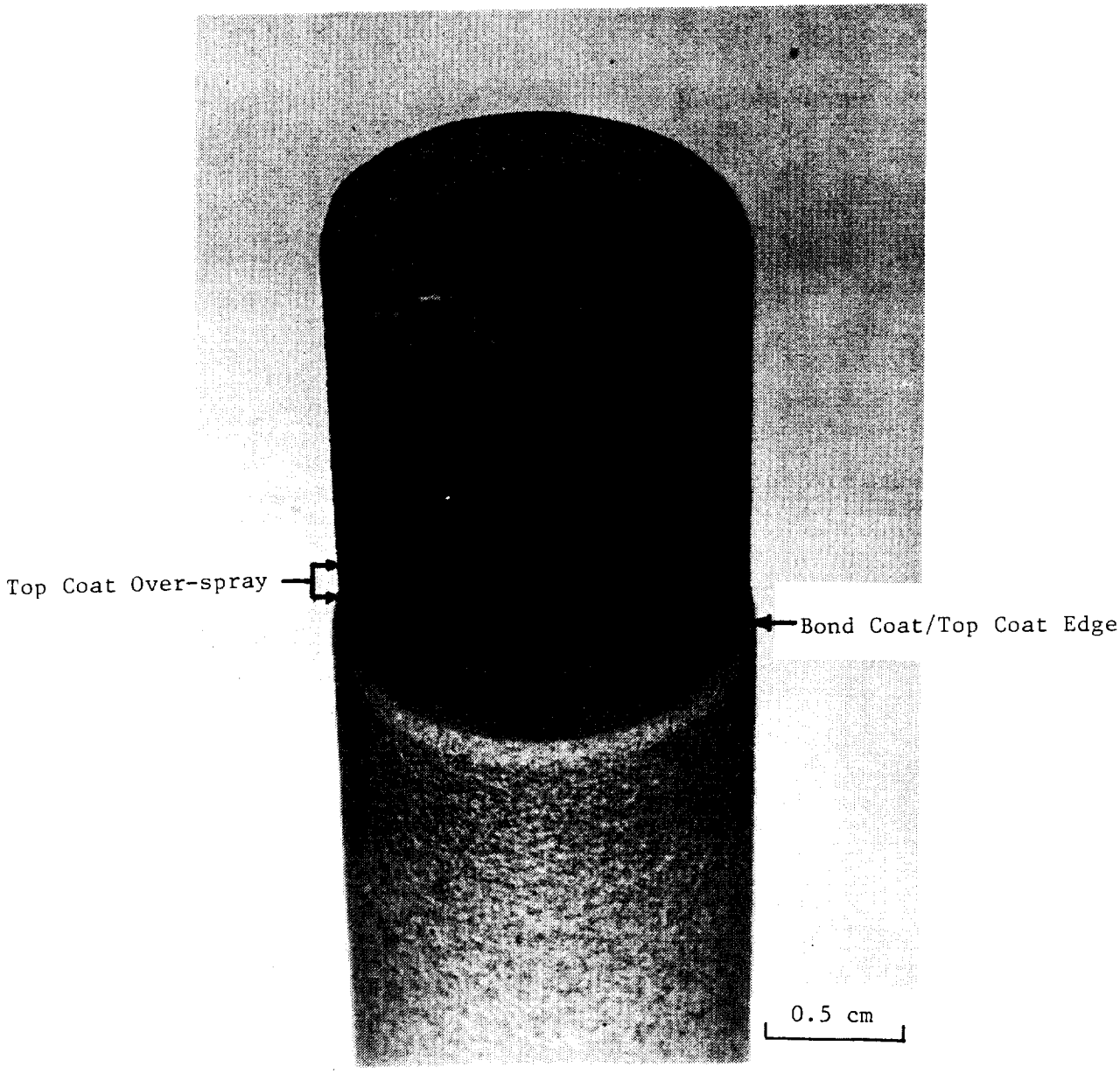

Figure 3. Tapered Top Coat Edge Produced by Shadow Masking.

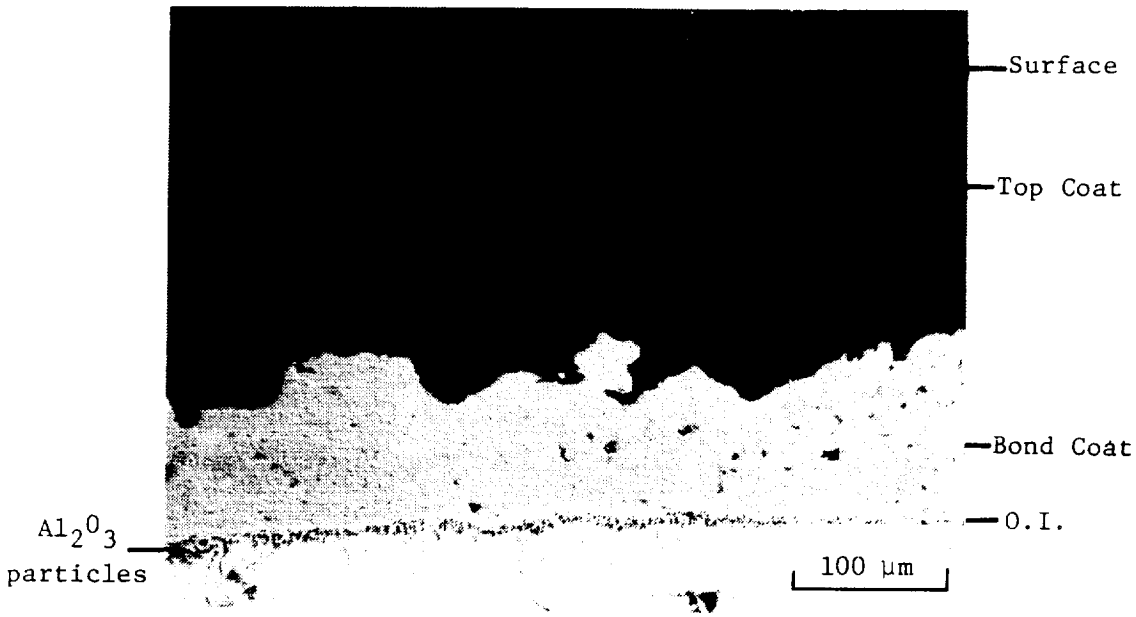

a. As-Sprayed Microstructure

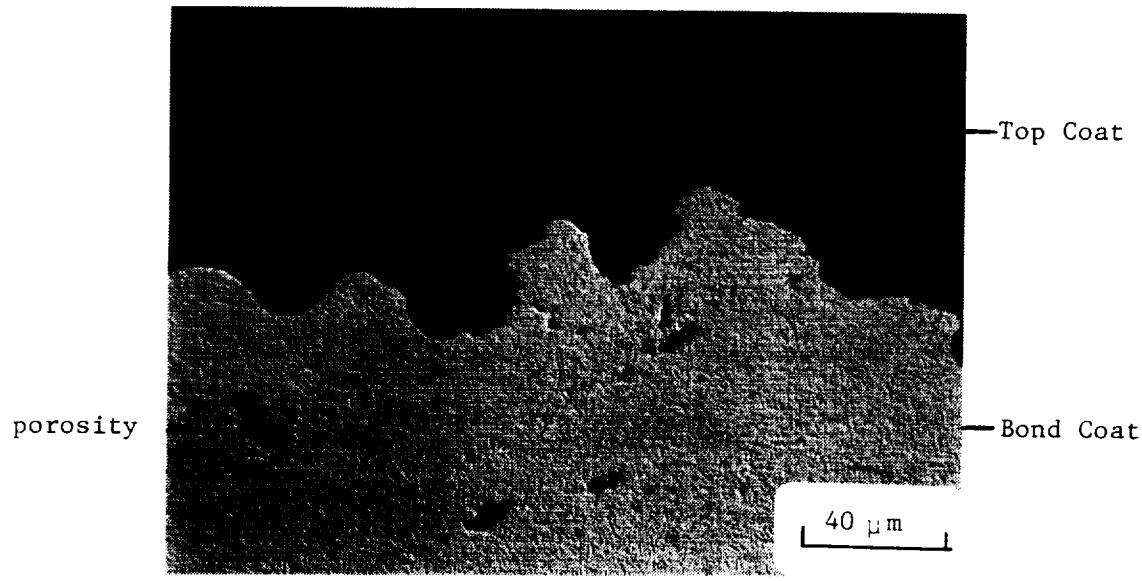

b. Bond Coat/Top Coat Interface

Figure 4. As-Sprayed Microstructure of Baseline TBC (René 80, NiCrAlY, ZrO_2-Y_2O_3).

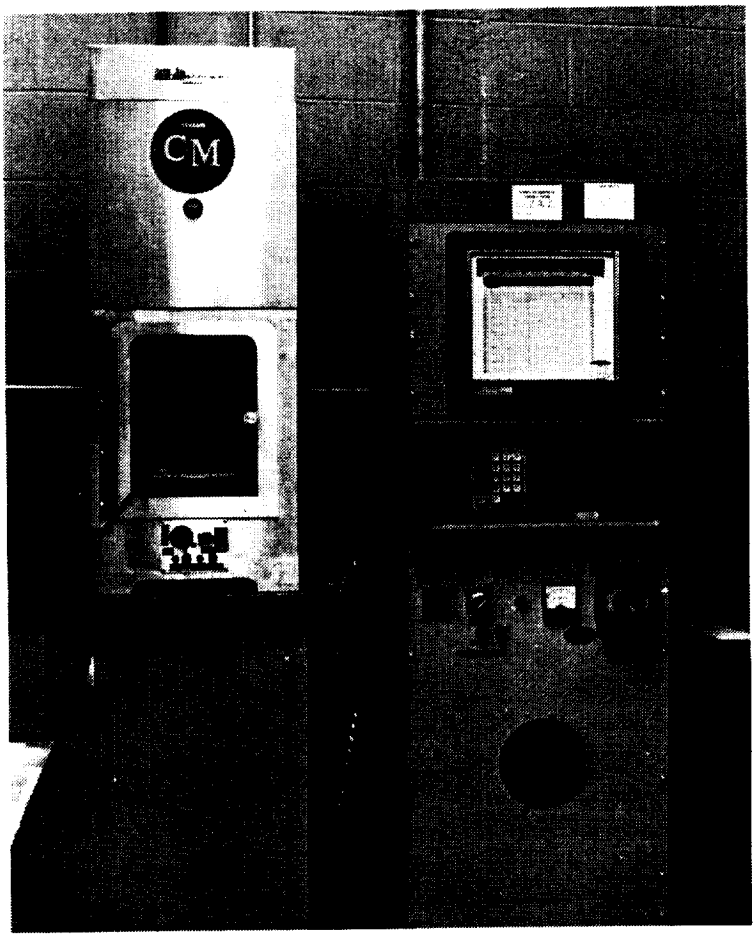

a. Thermal Cycle Test Furnace

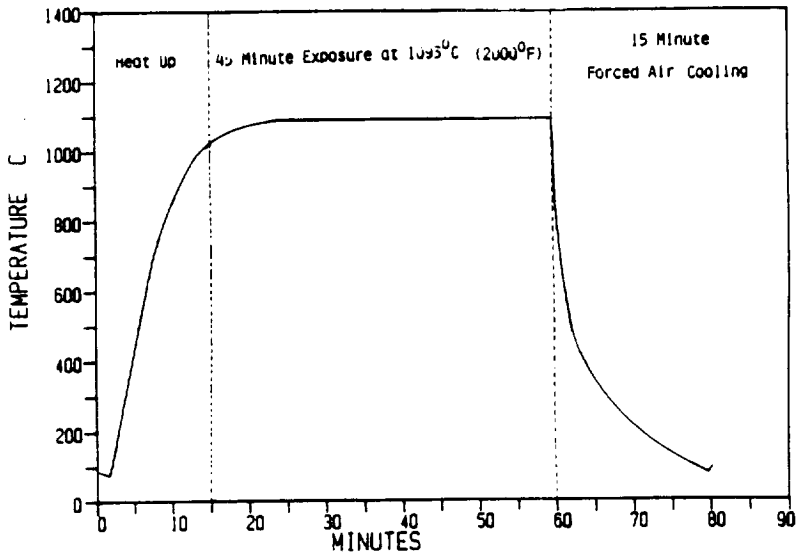

b. Schematic of Thermal Cycle.

Figure 5. Thermal Cycle Test Furnace and Schematic of Thermal Cycle.

JETS Test

The Jet Engine Thermal Shock (JETS) test rig was designed and built specifically for cyclic testing of thermal barrier coated specimens. Large thermal gradients through the coating are generated while cycling the temperature between preset values. The rig, shown in Figure 6, consists of a heating/cooling assembly, a test specimen support on a vertical carrousel, an electronic indexing system, and temperature measuring and recording equipment. Oxygen-propane torches provide rapid heating of the TBC face of button specimens while the back, uncoated side of the specimen is air cooled. The specimens are then cooled by a compressed air blast at the next station. In the testing conducted in Task I, face temperatures ranged from 1375° to 1520°C (2510° to 2765°F) and back side temperature ranged from 890° to 1015°C (1630° to 1860°F).

3.3 Bond Coat Oxidation

One of the potential failure mechanisms investigated in Task I was bond coat oxidation. As discussed above, many studies indicate that oxidation of the bond coat may be a major contributor to coating failure. To gain additional insight on this, experiments were conducted with the goal of comparing the magnitude of the effect of bond coat oxidation on coating life to the magnitude of the aggregate effect of the other phenomena that can occur in the coating at use temperature.

In the first of these experiments, thermal cycle tests were performed in air on specimens that had received isothermal pre-exposures in either oxidizing (static air) or inert (static argon) atmospheres at 1093°C (2000°F) for times of 10, 50, 100, and 500 hours. It was assumed that all pre-exposed specimens, whether pre-exposed in an oxidizing or an inert environment, contained "predamage" resulting from the thermally activated processes other than oxidation, whereas only specimens pre-exposed in air contained, in addition, the predamage due to oxidation (oxide scale growth on the bond coat). Thus, the difference in thermal cycle test lives of the two groups should reflect the effect of bond coat oxidation and allow evaluation of the magnitude of the other thermally-activated phenomena (sintering of the bond coat and zirconia layer, bond coat and ceramic coat creep, and bond coat/substrate interdiffusion). Tube specimens were utilized in this experiment.

The results from this experiment were not as expected in that the specimens which had been pre-exposed in argon failed (failure was defined as spallation of 10% of the ceramic top coat) with thermal cycle lives less than those of specimens pre-exposed in air (Figure 7). Failures in all cases occurred in the ceramic top coat approximately 0.025-0.050 mm (0.001-0.002 inch) from the bond coat/top coat interface (this is the normal TBC failure location in plasma-sprayed coatings). Continuous oxide scales of approximately 4 μm were observed at the bond coat/top coat interface for the as-sprayed and air pre-exposed specimens at failure after thermal cycle testing (excluding the 472 hour pre-exposure specimens - Figure 8). This is contrasted with the specimens pre-exposed in argon where oxide scales generally less than 1 μm developed and appeared noncontinuous as determined by optical microscopy (the

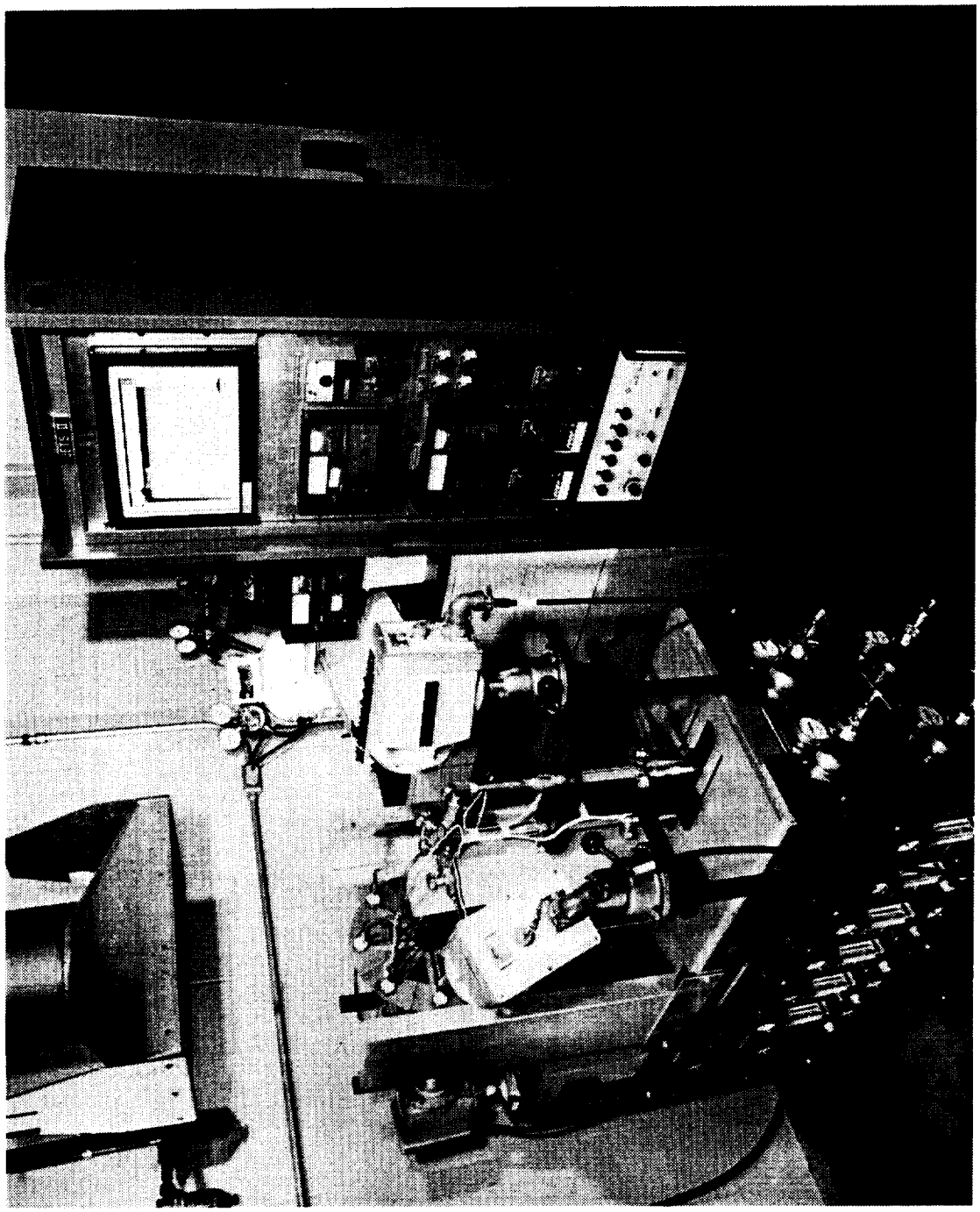

Figure 6. Jet Engine Thermal Shock (JETS) Test Rig.

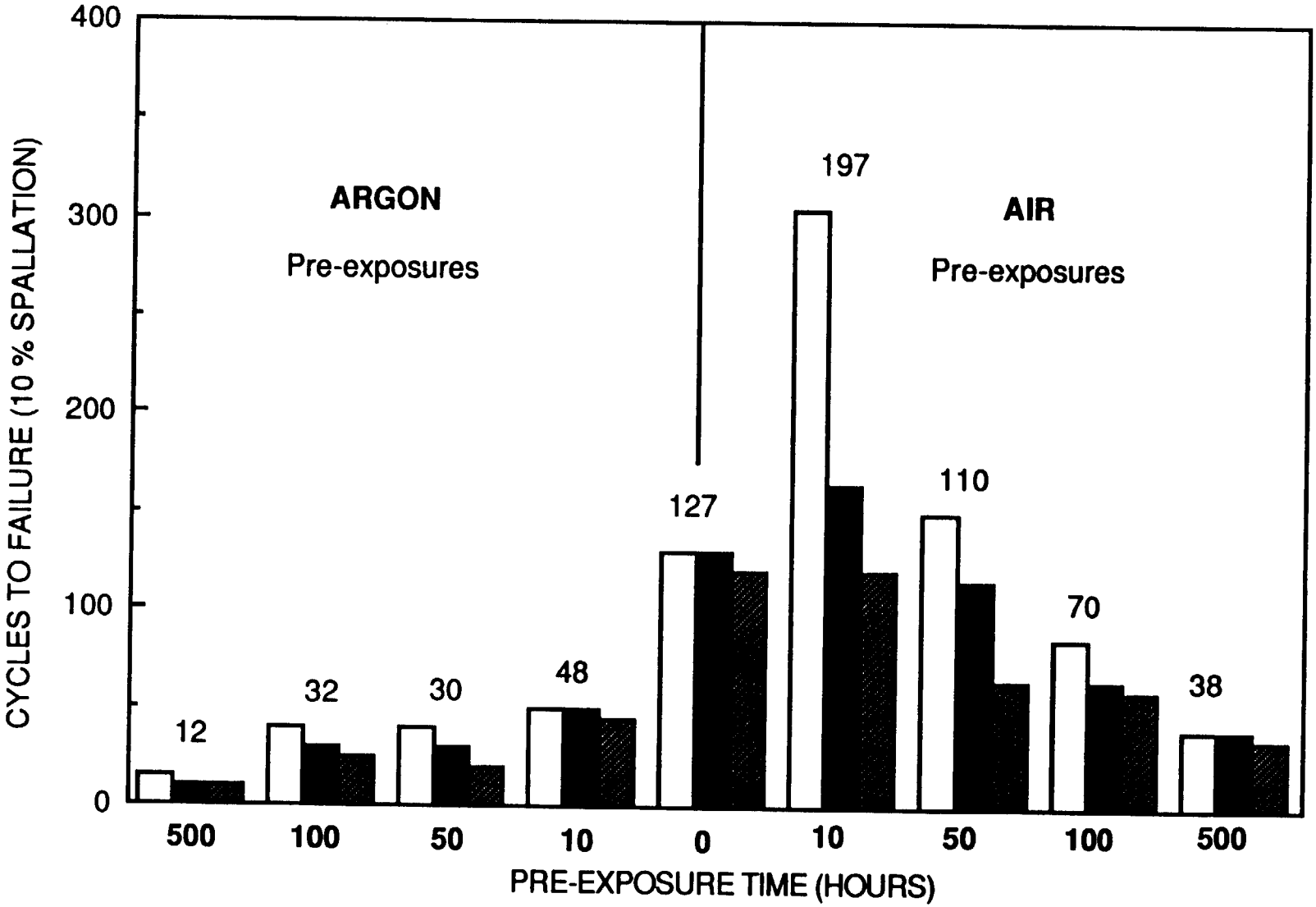

Figure 7. Furnace Cycle Test (1093°C) Lives of Specimen with Pre-Exposures at 1093°C in Air or Argon (First Experiment). (Numbers Above Bars are Averages.)

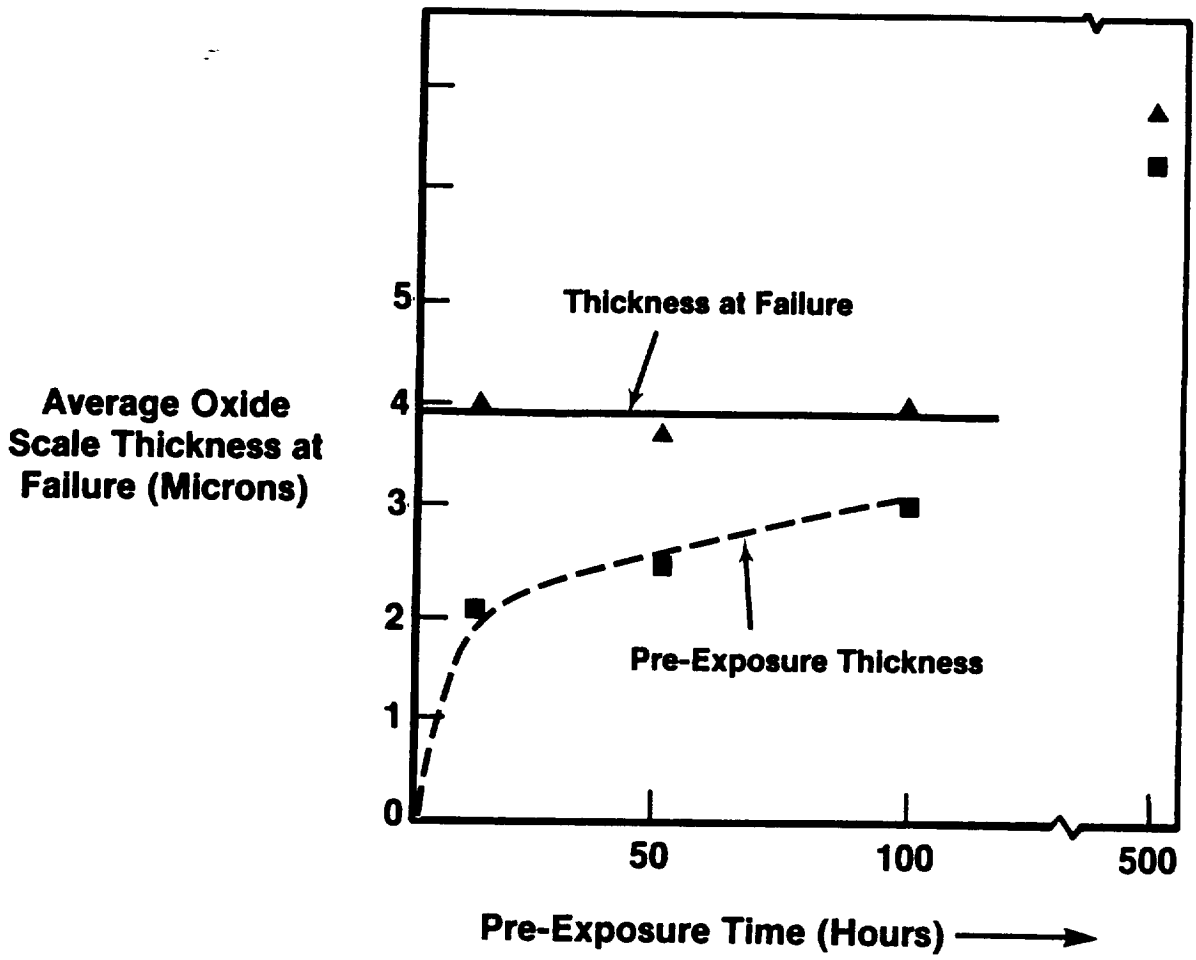

Figure 8. Oxide Scale Thickness at the Bond Coat/Top Coat Interface After Thermal Cycle Testing at 1093°C (First Experiment).

microstructures of pre-exposed specimens are shown in Figures 9 and 10). The observation that, at failure, the bond coat oxide scale thicknesses were essentially identical for the specimens that were not pre-exposed or were pre-exposured in air is consistent with the work of Miller (35), who noted similar weight gains (oxidation) at failure of specimens with a $CaSiO_4$/MCrALY TBC regardless of test temperature.

A second experiment was similar to the first except that some of the specimens were thermal cycle tested in argon, and the effect of different pre-exposure temperatures was evaluated. Thermal cycling in argon was achieved by sealing specimens in argon-filled Inconel 718 canisters (Figure 11) and testing them in the thermal cycle furnace. Argon pressure in the canisters was adjusted to be approximately 1 atmosphere at test temperature 1093°C (2000°F). Some specimens received no pre-exposure (as-sprayed), and others received 100-hour isothermal pre-exposures at 1093°C (2000°F) in either static air or static argon (Table II). Baseline specimens with similar histories were thermal cycle tested in unsealed canisters so that they would experience heating and cooling rates similar to the specimens sealed in argon-filled canisters. The unsealed canisters also contained specimens that had been pre-exposed at 982°C (1800°F) for 250 hours in either static air or static argon to assess the effect of different pre-exposure temperatures. By thermal cycling in argon, minimum scale growth occurred during cycling. Button specimens were utilized in this experiment. To compensate for the slower cooling rate of the specimens enclosed in canisters, the cooling period was increased from 15 minutes to 30 minutes.

The test results again indicate that exposing TBCs in argon can substantially decrease thermal cycle life, and the decrease in life is probably associated with an effect on bond coat oxidation. In this test, the longest thermal cycle lives were associated with specimens that received a pre-exposure in air prior to thermal cycling in argon (Figure 12, left side). Their lives were longer than those of the specimens that received no pre-exposure and specimens that had been pre-exposed in argon. The longer life of specimens pre-exposed in air may be associated with the development of a more continuous adherent Al_2O_3 scale prior to thermal cycling in argon.

Microstructural examination indicated that thermal cycling in argon was highly effective in minimizing bond coat oxidation. For the specimens that received no pre-exposure (Figure 13a) or received pre-exposures in argon, essentially no oxide scale was present at the bond coat/top coat interface (less than 1 μm of noncontinuous oxide scale), while no measurable increase in oxide scale thickness during thermal cycling was noted for the specimens that had been pre-exposed in air (Table II and Figure 13b).

The results for the specimens thermal cycled in the unsealed canister indicate that pre-exposures in argon were detrimental for this TBC system regardless of pre-exposure temperature. For both the 982°C (1800°F) and the 1093°C (2000°F) pre-exposures, the specimens pre-exposed in argon failed before the specimens pre-exposed in air.

Another interesting result was the extremely short lives exhibited by the specimens that received no pre-exposure or pre-exposures in air that were thermal cycled in the unsealed (air)

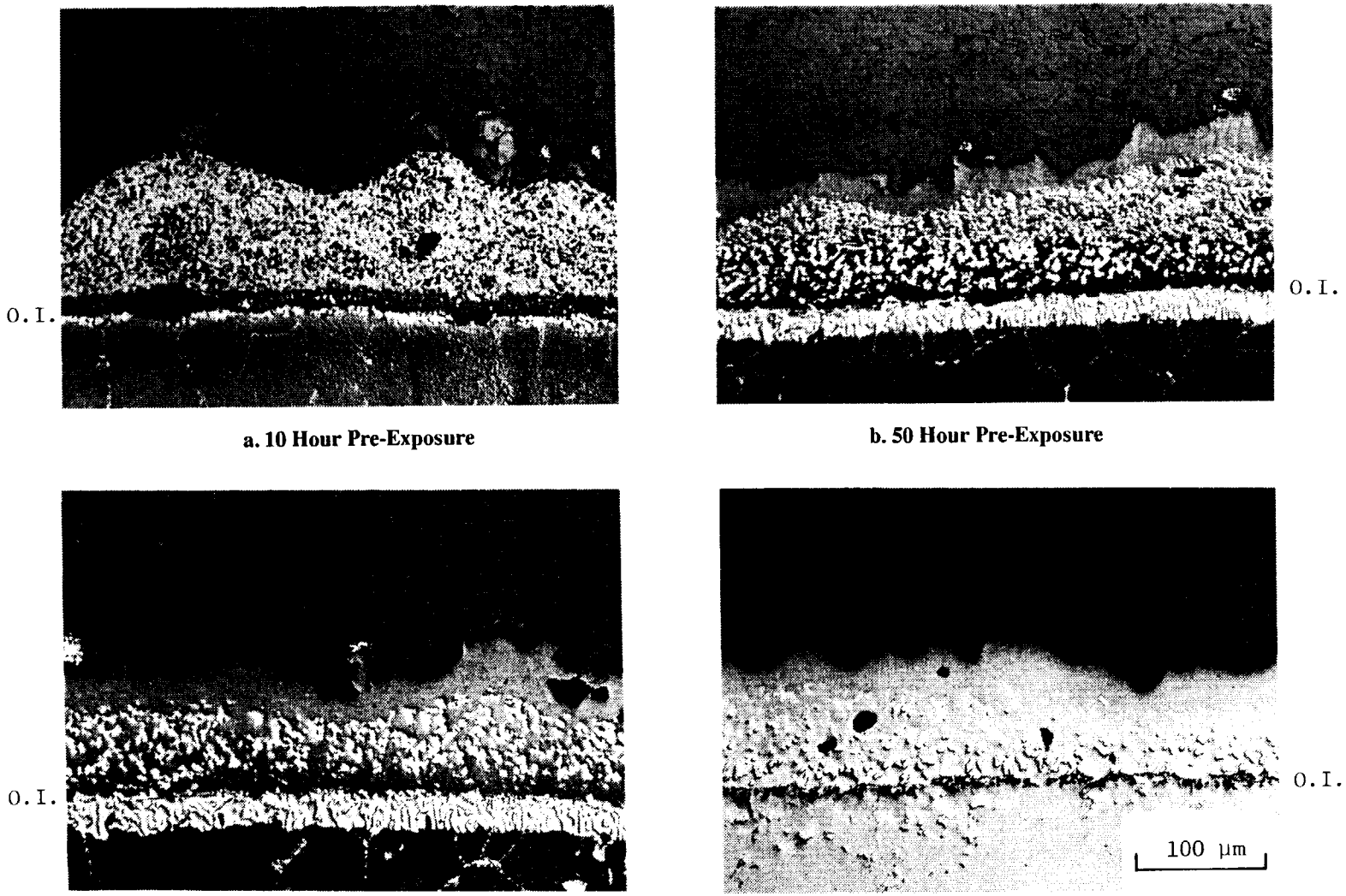

a. 10 Hour Pre-Exposure

b. 50 Hour Pre-Exposure

c. 100 Hour Pre-Exposure

d. 472 Hour Pre-Exposure

Figure 9. Microstructures of Specimens Pre-Exposed in Air at 1093°C (2000°F).

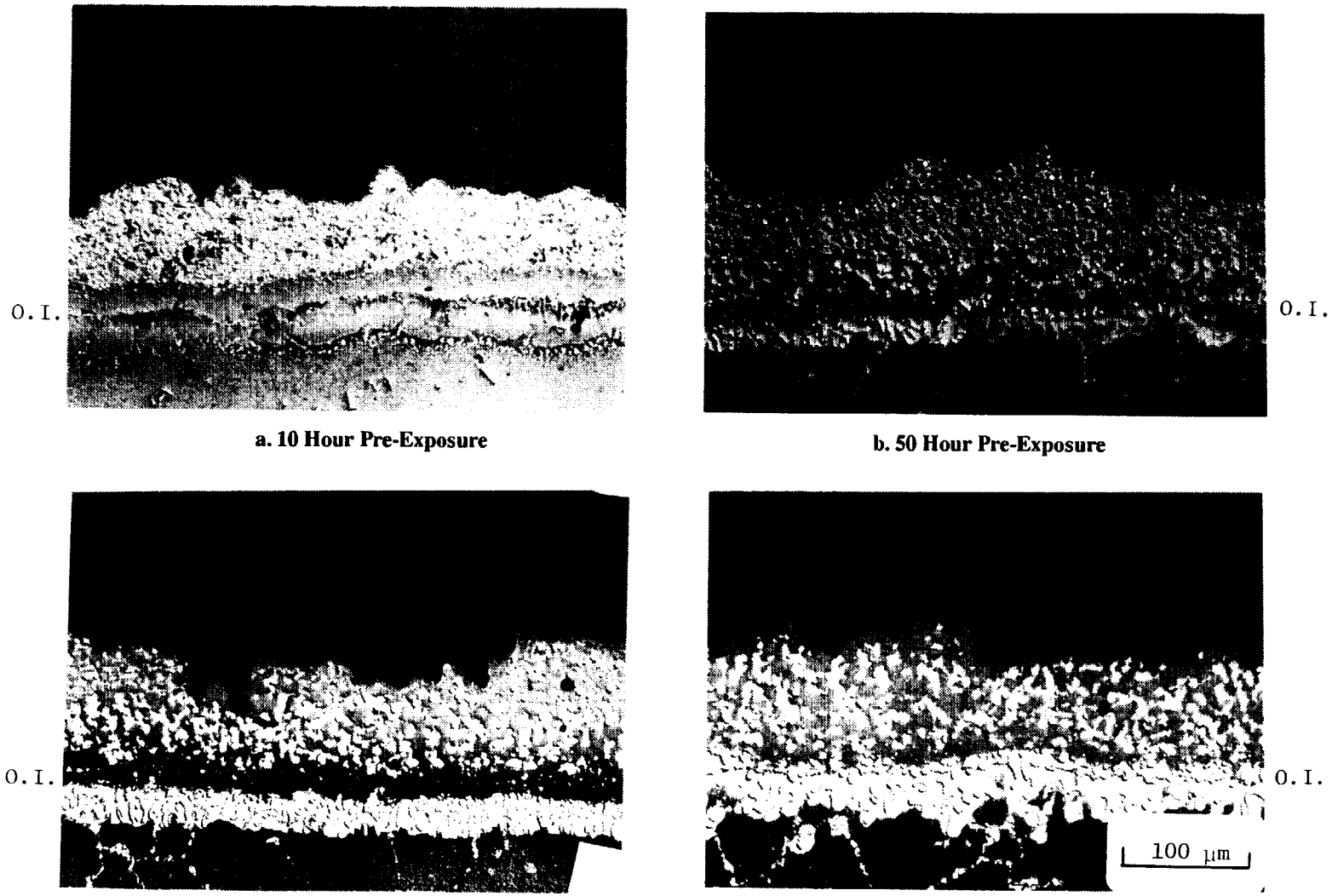

a. 10 Hour Pre-Exposure

b. 50 Hour Pre-Exposure

c. 100 Hour Pre-Exposure

ETCHED

d. 472 Hour Pre-Exposure

Figure 10. Microstructures of Specimens Pre-Exposed in Argon at 1093°C (2000°F).

Figure 11. Inconel 718 Canister Utilized for Thermal Cycle Testing in Argon.

TABLE II. Pre-Exposure and Test Conditions of Specimens[a] in Second Thermal Cycle Test.

Pre-exposure[b] Environment	Pre-exposure Temperature	Pre-Exposure Time (Hr)	Thermal Cycle Test Environment	Oxide Thickness Before Cycling (μm)	Oxide Thickness After Cycling (μm)	Cycles
As-sprayed	----	----	Argon	0	1	46
Air	1093°C (2000°F)	100	Argon	4.3	4.3	94
Argon	1093°C (2000°F)	100	Argon	1	1	46
As-sprayed	----	----	Air	0	6.4	94
Air	1093°C (2000°F)	100	Air	4.6	6.4	78
Argon	1093°C (2000°F)	100	Air	1	1.0	15
Air	982°C (1800°F)	250	Air	4.1	7.1	78
Argon	982°C (1800°F)	250	Air	1	3.6	38

[a]René 80 buttons coated on one face with LPPS NiCrAlY and APS ZrO_2-8% Y_2O_3.

[b]All pre-exposures occurred after the top coat was applied.

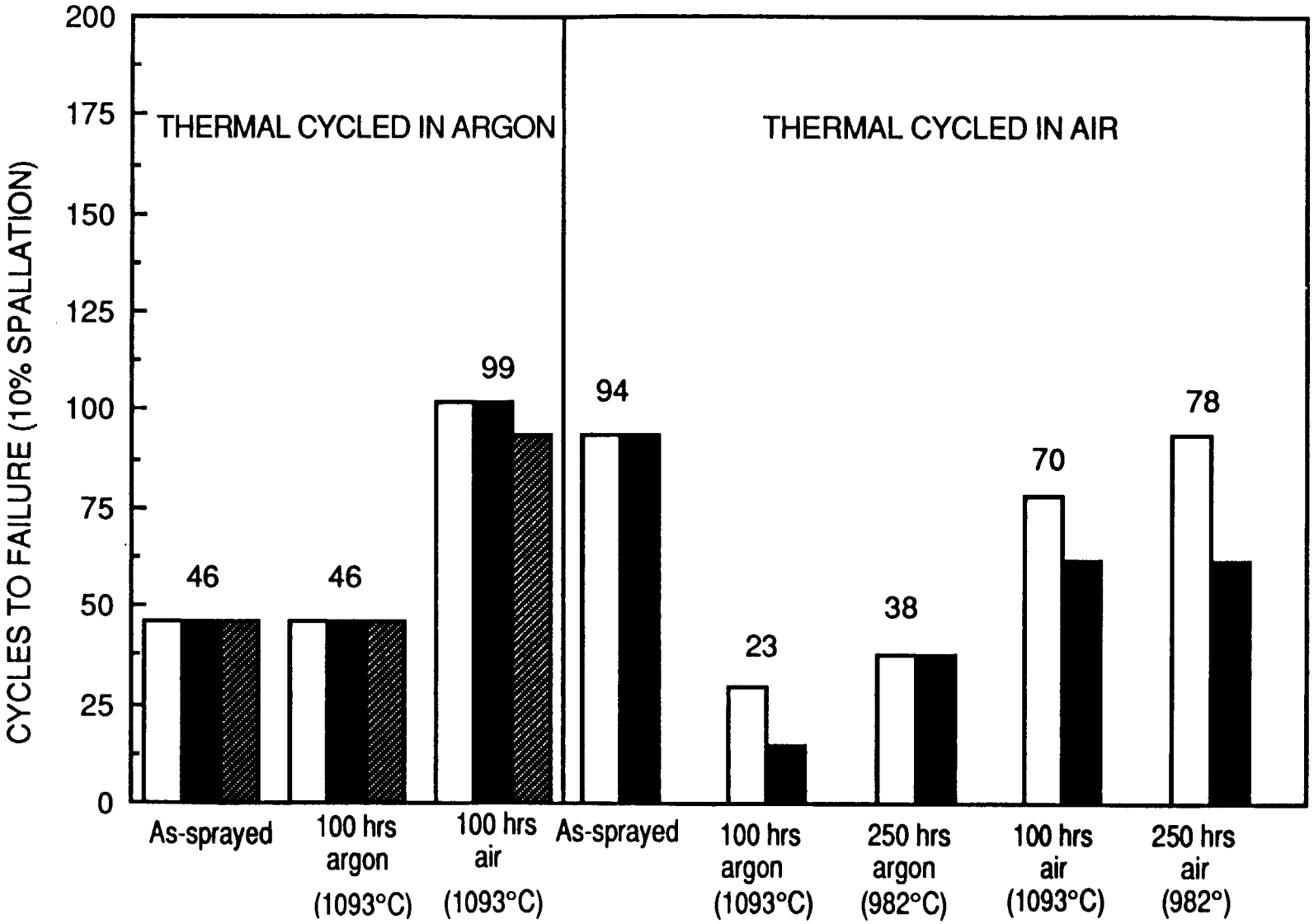

Figure 12. Furnace Cycle Test Lives in Air and Argon at 1093°C of Specimens with Various Pre-Exposures in Air or Argon (Second Experiment). René 80 Button Specimen Coated on One Face with LPPS NiCrAlY and APS ZrO_2-8% Y_2O_3 (Numbers above Bars are Averages.)

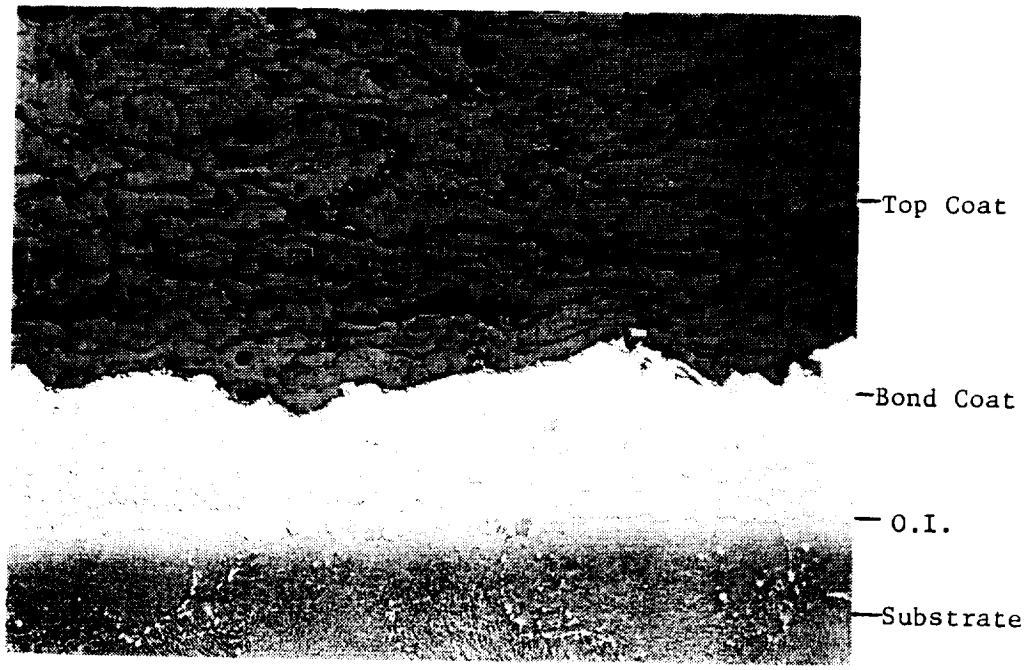

a. No Prior Pre-Exposure

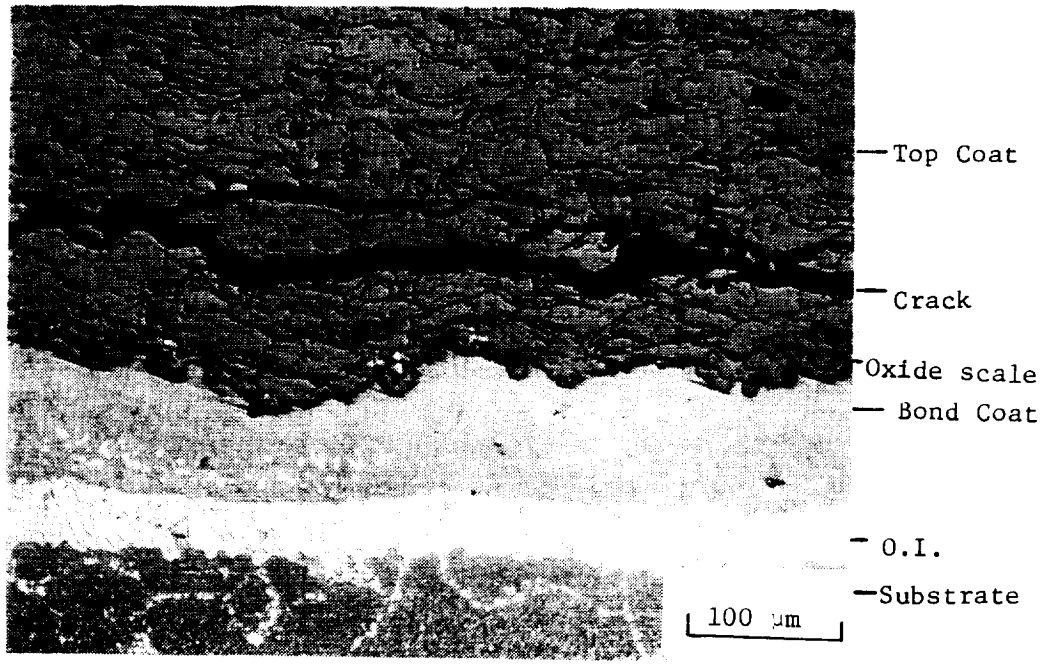

b. 100 Hour Air Pre-Exposure at 1093°C

Figure 13. Microstructure of Specimens (René 80/NiCrAlY/ZrO_2-Y_2O_3) After Thermal Cycle Testing in a Sealed Canister Containing Argon in the 1093°C Test.

canister. Typically, button specimens of this type with no prior pre-exposure will have thermal cycle lives of approximately 400 cycles when cycled outside the canister. However, in this test, specimens with no pre-exposure failed in less than 100 cycles when cycled in this unsealed canister (Figure 12, right side). Microstructural examination of these specimens indicated that significant frontal oxidation of the bond coat had occurred. Electron microprobe mapping of these oxide scales revealed that they contained high levels of Cr and Ni. This indicates that less protective oxide scales with higher growth kinetics had formed on the bond coats of these specimens cycled in the unsealed canister. The cause of the formation of Cr and Ni oxides is not understood, but may be related to the presence on the surface of the TBC of oxide scale which spalled from the inside of the open Inconel canister during the thermal cycle test. Discoloration of the surface of the TBC due to this material was observed during the course of the testing. Baseline specimens (Hasteloy-X/NiCrAlY/ZrO_2-8Y_2O_3), which are included in all furnace cycle tests, also failed early in this test. These baseline specimens, which normally last 400-450 cycles, failed in only 60 cycles when tested in the canister. Significant frontal oxidation of the bond coat also occurred in these specimens. These results clearly demonstrate the importance of bond coat oxidation. In this case, thick Cr and Ni scales formed which resulted in significantly shorter thermal cycle life.

In the third experiment, a slightly different approach was used to evaluate bond coat oxidation and determine if the detrimental effect of argon could be more definitely traced to bond coat or top coat changes. In this experiment, combinations of pre-exposures in air and/or argon were performed before and after the top coat application (Table III). This experiment was run concurrently with the second experiment in the same test furnace but without using the canister (the same, 30 minute cool down period was used). In this test, the specimens with no prior exposure had the expected thermal cycle life of approximately 400 cycles.

Two sets of specimens were given 100-hour pre-exposures in both air and argon after the top coat was applied. One set received the air pre-exposure first and then the argon pre-exposure, while the other set of specimens received the argon pre-exposure first. The hypothesis was that if the detrimental effect of argon pre-exposure is due to argon effects in the top coat ZrO_2-Y_2O_3 (stoichiometry), any reduction of the oxide state of the zirconia by the argon pre-exposure should be eliminated by the subsequent air pre-exposure, hence the subsequent thermal cycle life of specimens pre-exposed in argon first should be longer than those of specimens pre-exposed in air first. On the other hand, pre-exposing in air first should form the more protective Al_2O_3 scale prior to the argon pre-exposure and provide a chemical bond similar to that normally observed. If the greater effect of argon pre-exposures is related to whether or not adherent Al_2O_3 scales are formed, then specimens pre-exposed in air first should have longer thermal cycle lives than those pre-exposed first in argon. The specimens pre-exposed in argon first had very short lives (14 cycles), while the specimens pre-exposed in air first had substantially longer lives (237 cycles), (Figure 14) indicating that the most significant effect of argon pre-exposure is its influence on oxide scale species. As further evidence, X-ray diffraction analysis of the ceramic top coat of specimens that were pre-exposed in air for 100 hours or pre-exposed in argon for 100 hours at 1093°C (2000°F) indicate that no major phase changes had occurred during the argon pre-exposure. Hence, the

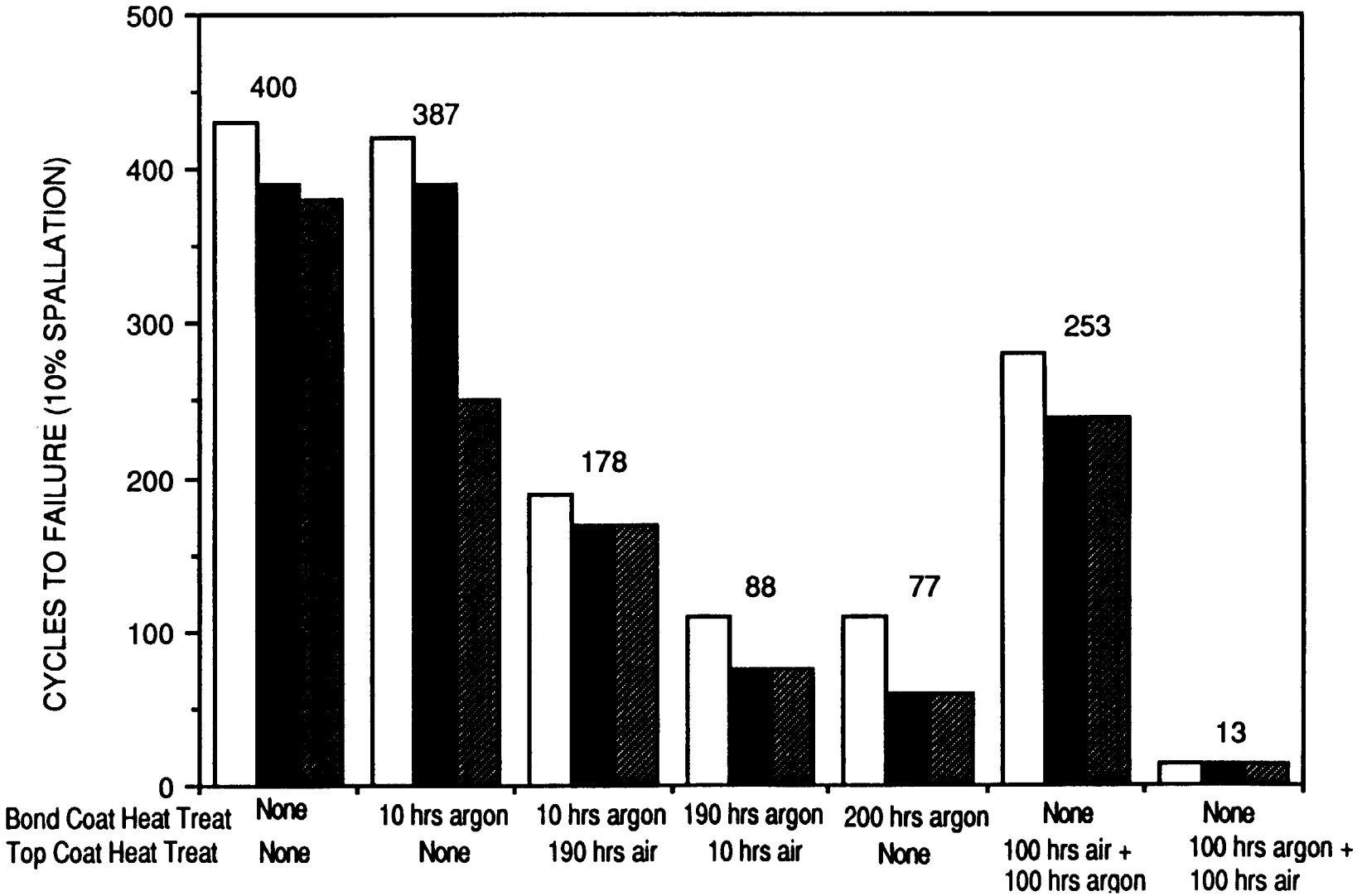

Figure 14. Furnace Cycle Test (1093°C) Lives of Specimens with Various Heat Treatments and Pre-Exposures in Air and/or Argon (Third Experiment). René 80 Button Specimens Coated on One Face with LPPS NiCrAlY and APS ZrO_2-8%Y_2O_3. (All Specimens Received a 1-Hour Vacuum Heat Treatment at 1093°C After Bond Coat Application and Prior to Noted Heat Treatments). (Numbers Above Bars are Averages)

Table III. Pre-exposure Conditions of Specimens[a] in Third Thermal Cycle Test.

Bond Coat Heat Treatment in Argon[b]	Top Coat Pre-Exposure
None	100 hr in argon plus 100 hr in air
None	100 hr in air plus 100 hr in argon
10 hr argon	190 hr in air
190 hr argon	10 hr in air
200 hr argon	None
10 hr argon	None
None	None

[a]René 80 buttons coated on one face with LPPS NiCrAlY and APS ZrO_2-8% Y_2O_3.

[b]All specimens received 1 hour vacuum heat treatment at 1093°C after bond coat deposition and prior to any heat treatment in argon.

results of this third experiment, combined with the X-ray results and results from the second experiment, clearly indicate that the detrimental effect of argon is primarily associated with its effect on bond coat oxidation.

Heating the bond coat of some specimens (groups 2 through 5 in Figure 14) in argon before the top coat was applied was also done to test whether the argon pre-exposure was affecting the bond coat or the zirconia. The foreshortened test lives of specimens which had been pre-exposed for long times (greater than 100 hours) in argon before the top coat was applied again indicates that the detrimental effect of argon pre-exposures is related to its effect on the bond coat rather than the top coat.

A GE-funded investigation (36) which was performed to further understand how argon may affect the thermal cycle life of TBCs, indicated that the shortened life may be the result of diffusion of Cr, Ta, W, and other substrate elements to the bond coat/top coat interface during the inert atmosphere pre-exposure prior to significant bond coat oxidation. In most cases, carbide precipitates (presumably $M_{23}C_6$ carbides) were observed in the bond coat at the bond coat/top coat interface (also noted in other locations in the bond coat). This was observed to a greater degree in specimens that had been pre-exposed in argon. Thus, the

decrease in life of specimens pre-exposed in argon may be associated with the formation of Cr, Ta, W, and other less protective oxides which interfere with the formation of stable, adherent Al_2O_3 scales. This lack of formation of an Al_2O_3 scale may also be affected by the low oxygen partial pressure present in the argon atmosphere exposures. A less protective oxide could contribute to earlier failure of the TBC if its presence results in faster scale growth and/or results in poorer bonding between the zirconia, oxide scale, and bond coat.

Based on the above results, a fourth experiment was performed where all specimens received a 10 hour pre-exposure in air at 1093°C prior to other air or argon pre-exposures, and thermal cycle testing. The goal was to develop the same oxide scale on all specimens and therefore more completely evaluate the contribution of bond coat oxidation to coating failure. The results (Figure 15) indicate air pre-exposures are more detrimental than argon pre-exposures when each is preceded by an air pre-exposure. The larger decrease in thermal cycle life for the air pre-exposures is attributed to the growth of oxide scale during that pre-exposure. These results conclusively demonstrate the importance of bond coat oxidation.

3.4 Bond Coat Creep

Another phenomenon that is a potential contributor to TBC failure is that of creep of the bond coat. It is believed that creep of the bond coat at elevated temperatures leads to an upward shift of the stress-free temperature and hence to larger compressive stresses in the zirconia layer on return to room temperature, thus causing a greater propensity for spalling.

An experiment was conducted to evaluate the effect of bond coat creep strength on thermal cycle life. It included TBCs with four different bond coat alloys (Table IV) that have different creep strengths. The modified NiCoCrAlY bond coats include various additions of Mo, Ta, W, Re, Hf, C, B, Si, Zr, and Ti. The bond coat layers on these specimens also received an aluminide (Codep) coating (Figure 16) before the ceramic layer was deposited in order to reduce the effect of any differences in oxidation resistance on thermal cycle life. All specimens were coated with the same ZrO_2-8%Y_2O_3 ceramic layer. Six specimens of each TBC system were thermal cycle tested. Two specimens were exposed in argon for 100 hours at 1093°C (2000°F), two were exposed in air for the same time and temperature, and two specimens received no pre-exposure. The difference in thermal cycle lives should be a function of bond coat creep strength and pretest conditions. The intent of this experiment was to evaluate the effect of bond coat creep strength on TBC failure and to obtain a measure of its effect relative to that of oxidation. Tube specimens were utilized in this test.

3.4.1 Coating Microstructures

The as-sprayed microstructures (Figure 17) contain small differences in structure associated with the changes in composition. In all of the systems, an aluminide overcoat is present and is clearly evident in the photomicrographs. Bond coat No. 1, which is the baseline system, plus an aluminide overcoat, has a microstructure consisting of $\gamma' + \beta + \gamma$. The aluminide coating produces a NiAl(β) coating at the surface of the bond coat. The other three bond coats, which contain numerous alloy strengthening additions, have a bond coat consisting

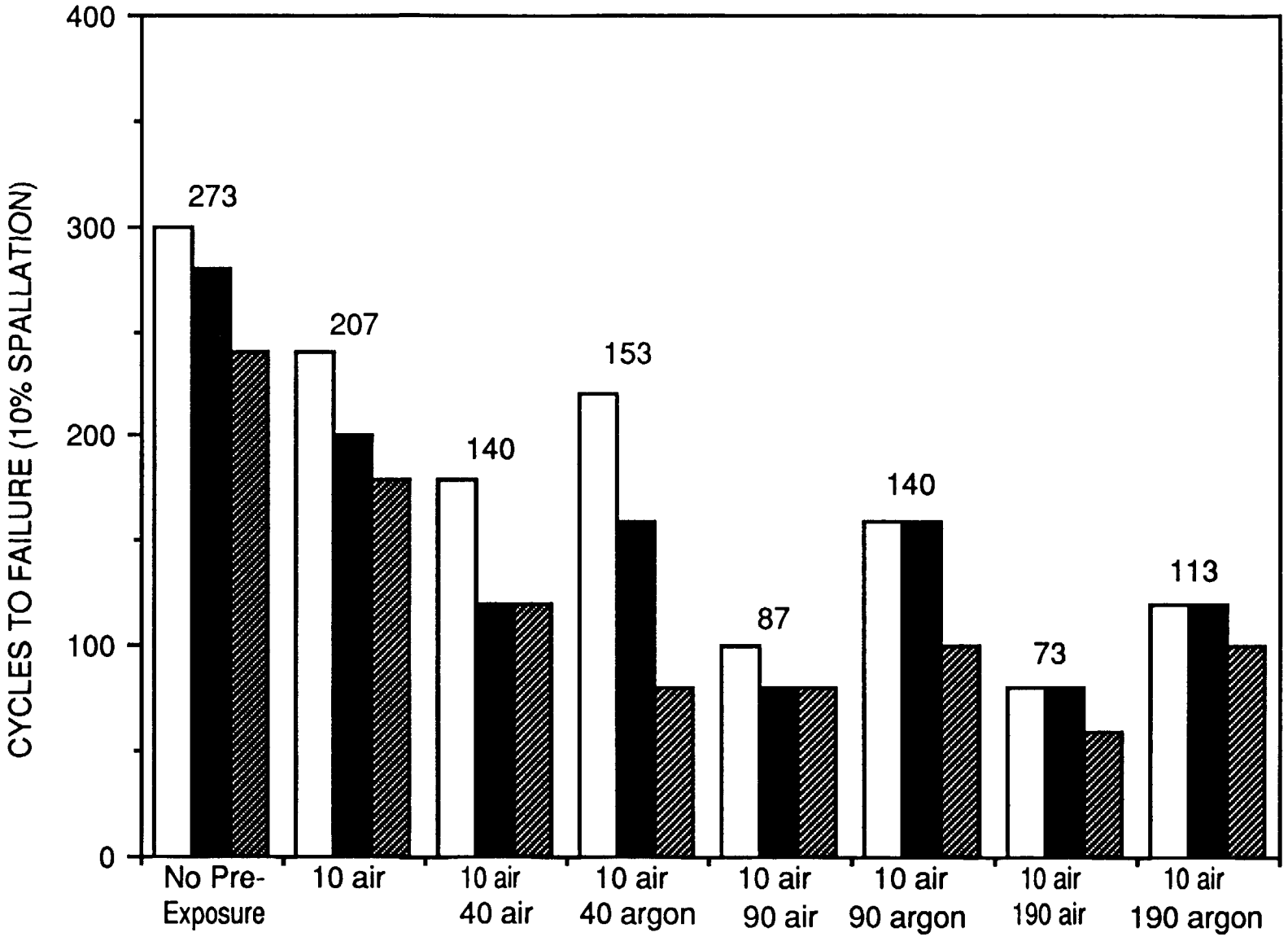

Figure 15. Furnace Cycle Test (1093°C) Lives of Specimens Pre-Exposed in Air or Argon After Initial 10-hour Exposure in Air at 1093°C (fourth Experiment). (Numbers Above the Bars are Averages.)

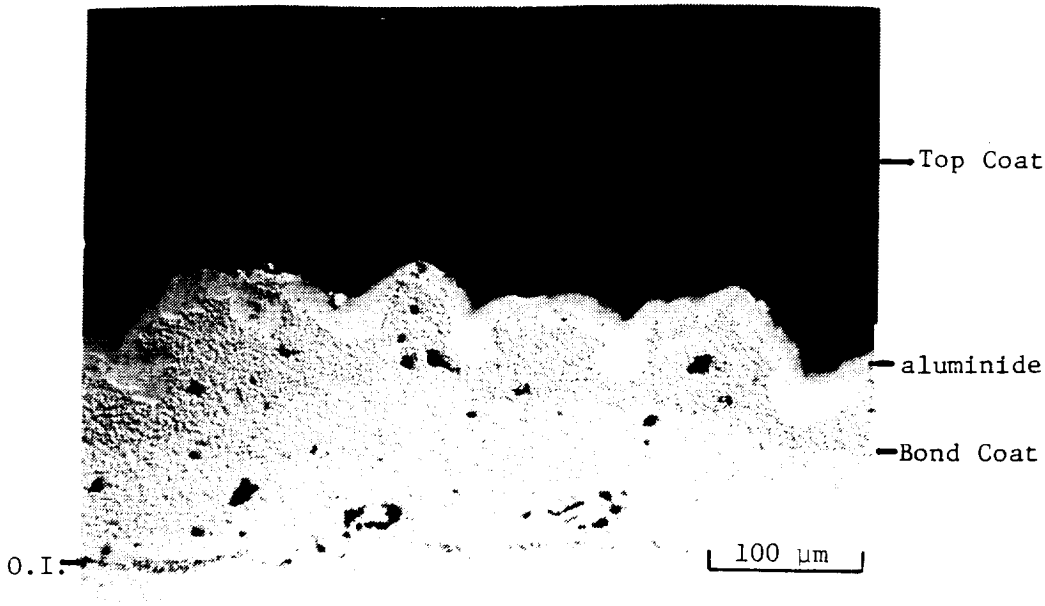

a. As-Sprayed Microstructure

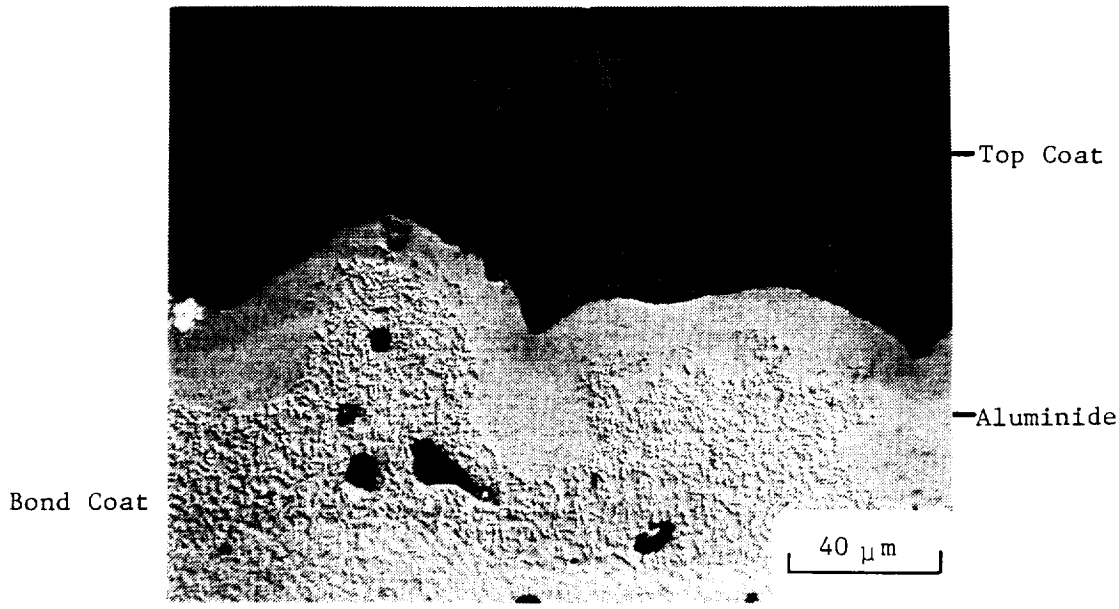

b. Bond Coat/To Coat Interface

Figure 16. Microstructure of As-Sprayed TBC with Aluminide-Coated Bond Coat (René 80/NiCrAlY/Aluminide/ZrO_2-Y_2O_3).

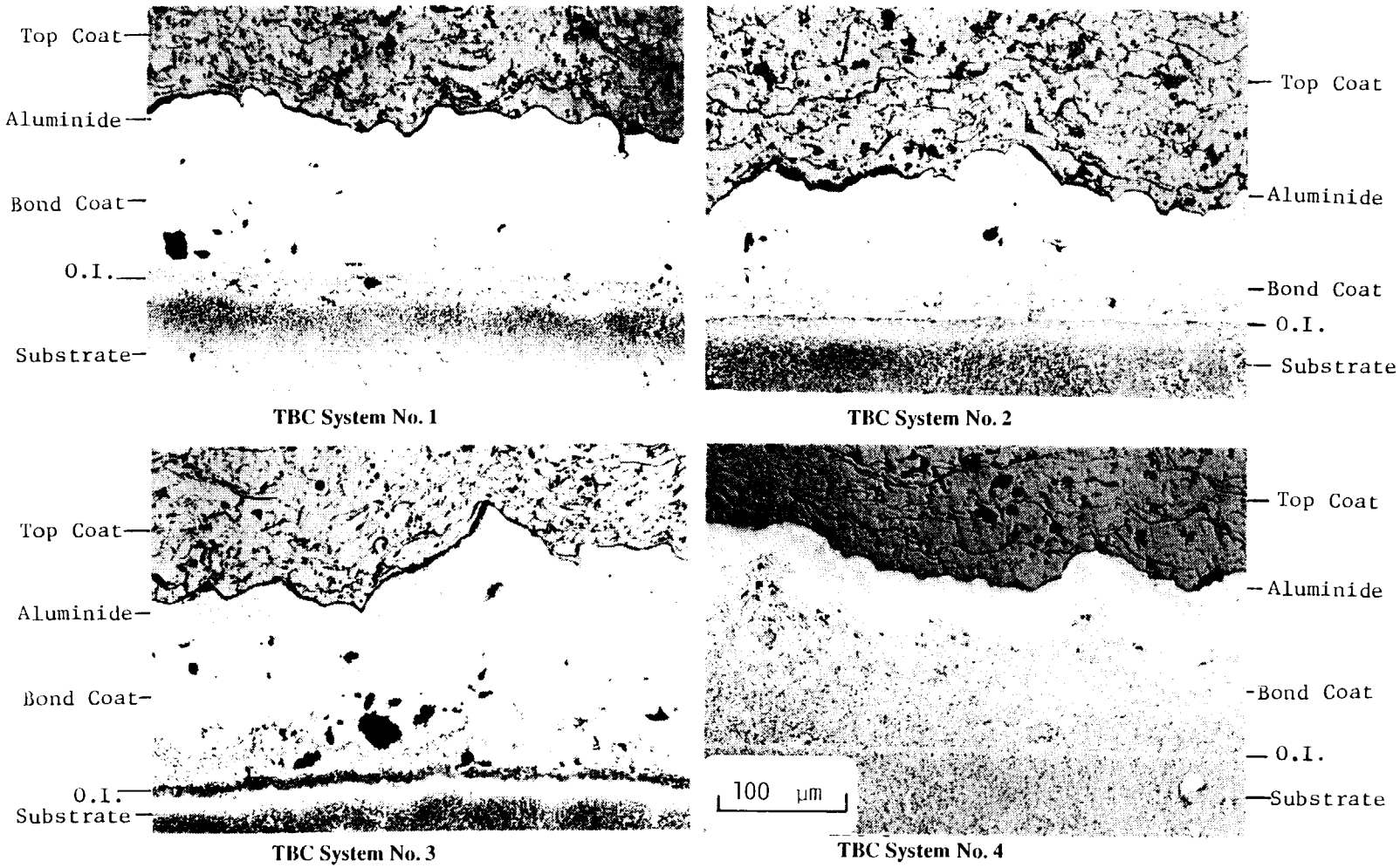

Figure 17. Microstructure of Four As-Srayed TBC Systems Tested in Bond Coat Creep Effect Experiment (René 80/Bond Coat/Aluminide/ZrO_2-Y_2O_3).

Table IV. TBC Systems Used to Evaluate Bond Coat Creep Effect on Coating Life.

Systems	Substrate	Bond Coating	Over Coating	Top Coating	Bond Coat Creep (Laron/Miller Parameter @ 3 ksi - rupture)
1	René 80	Bond Coating 1[a]	Aluminide	ZrO_2-Y_2O_3	39.0
2	René 80	Bond Coating 2[b]	Aluminide	ZrO_2-Y_2O_3	45.7
3	René 80	Bond Coating 3[b]	Aluminide	ZrO_2-Y_2O_3	47.0
4	René 80	bond Coating 4[b]	Aluminide	ZrO_2-Y_2O_3	48.4

[a]Ni-22Cr-10A1-0.3Y
[b]Modified NiCoCrAlY bond coats

of $\gamma' + \beta + \gamma$ carbides. The aluminide also produces a NiAl(γ) coating at the surface of bond coats No. 2, 3, and 4.

In all cases, a continuous Al_2O_3 scale formed at the bond coat/top coat interface in specimens that were pre-exposed in air for 100 hours at 1093°C (2000°F) (Figure 18)*, and the oxide scale thickness varied from 3 to 5 μm for the four different bond coat systems. The presence of a continuous carbide layer (presumably $M_{23}C_6$ [9]) was also noted at the bond coat/substrate interface for the NiCrAlY + aluminide system (TBC System No. 1). The aluminide in all cases was significantly depleted due to bond coat oxidation and bond coat/substrate interdiffusion. Bond coat No. 3 also developed blocky carbides during the pre-exposure. Unique changes in structure and morphology for each bond coat were expected due to the significant differences in bond coat compositions.

In assessing the effect of argon pre-exposure on these specimens, canisters were again used successfully to retard oxidation at 1093°C (2000°F). In all cases, essentially no Al_2O_3 scale was detected at the bond coat/top coat interface by optical microscopy after pre-exposure (Figure 19). The aluminide in all systems did not appear depleted since little bond coat oxidation had occurred. Interestingly, a continuous carbide layer was not present at the bond coat/substrate interface in bond coat No. 1 although the presence of significant quantities of (presumably) $M_{23}C_6$ carbides were noted at this interface following air pre-exposure. The presence of blocky carbides was again noted in bond coat No. 3 following the argon exposure.

*Phase identification of bond coat microstructure after pre-exposure and thermal cycle testing is shown in Appendix B.

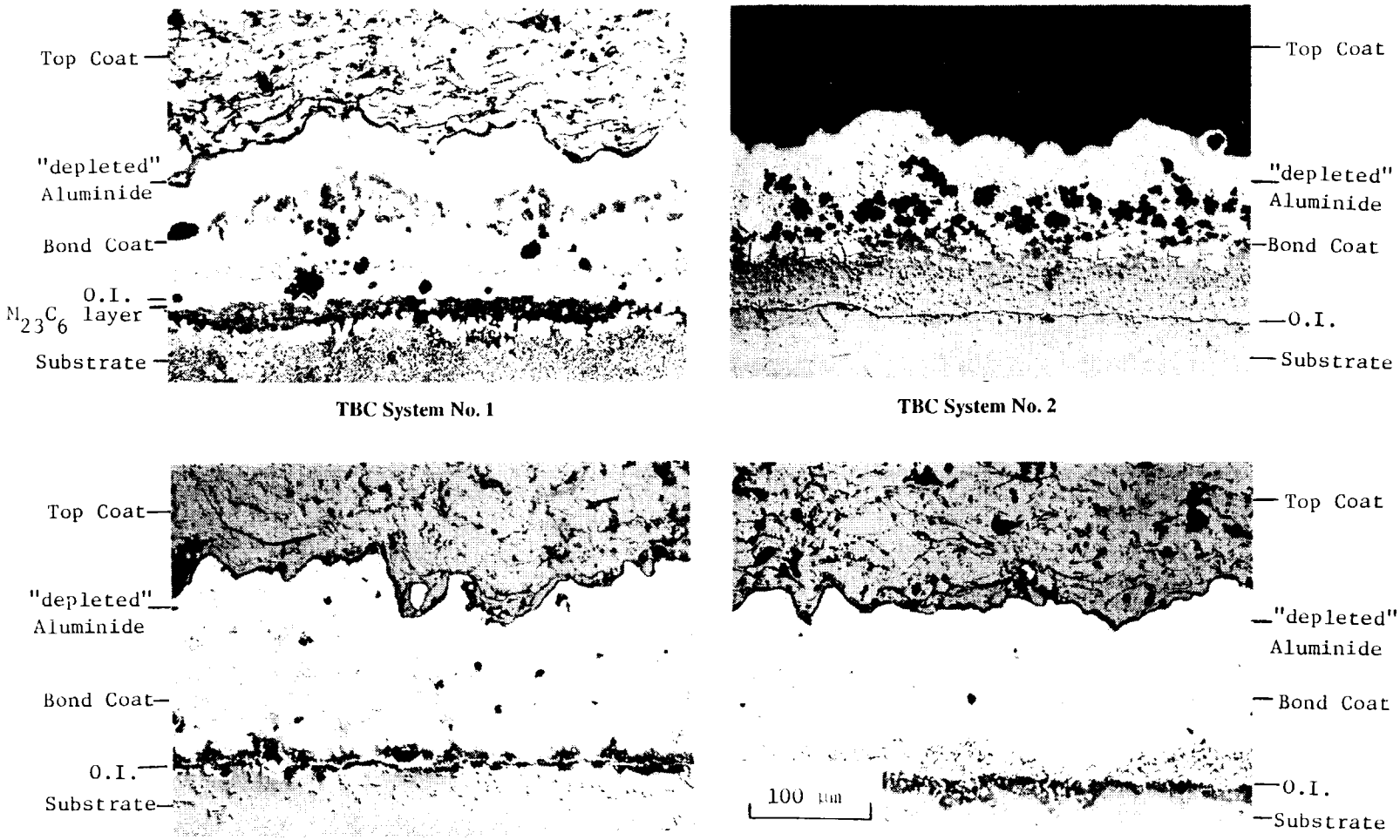

Figure 18. Microstructure of Four Bond Coat Creep Effect TBC Systems (René 80/Bond Coat/Aluminide/ZrO_2-Y_2O_3) After 100 Hour Pre-Exposure in Air at 1093°C.

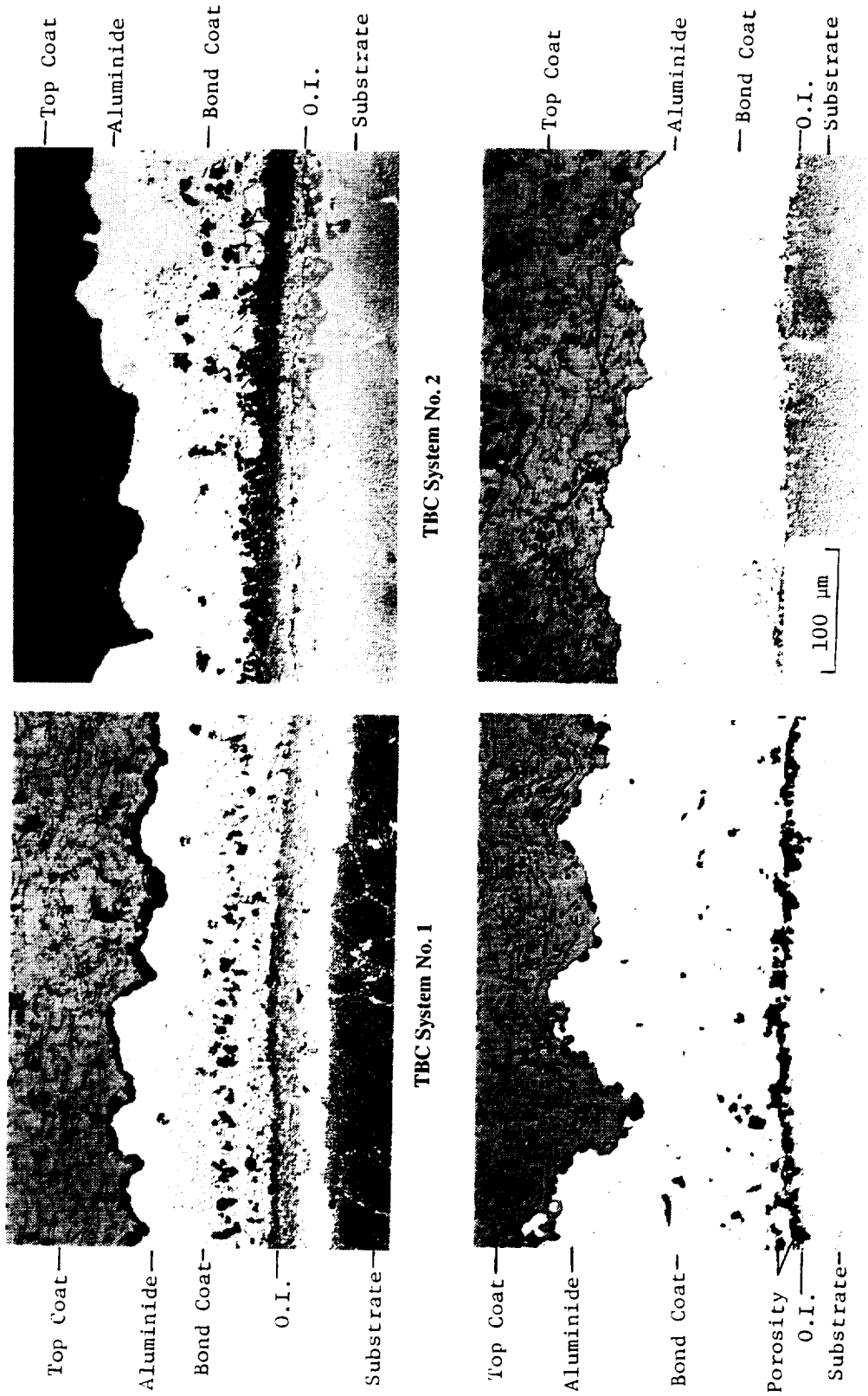

Figure 19. Microstructure of Four Bond Coat Creep Effect TBC Systems (René 80/Bond Coat/Aluminide/ZrO_2-Y_2O_3) After 100 Hour Pre-Exposure in Argon at 1093°C.

3.4.2. Thermal Cycle Testing

Duplicate specimens with each of the four coating systems, as-deposited and with each of the two pre-exposures, were thermal cycle tested at 1093°C (2000°F). The results clearly show that the TBC specimens with the NiCrAlY + aluminide bond coat, which has the lowest creep strength, resulted in the shortest thermal cycle life for all pre-exposure conditions (Figure 20). However, the thermal cycle life differences for the other TBC systems appears to be minimal. This may indicate that the bond coat creep strength differences (Table IV) for these materials were not large enough to offset the effect of other contributions to coating failure (NiCrAlY is significantly lower in strength than the other three).

Interestingly, the 100 hour air pre-exposure did not significantly affect the thermal cycle life of these systems with "high strength" bond coats (2, 3, and 4). This indicates that, as the thermal cycle life increases as a result of the increased bond coat creep strength, the relative contribution of the pre-exposure to the overall oxidation of the bond coat is reduced. The data suggest that bond coat creep can play a significant role in overall TBC life.

A weakness of this experiment was the potential for different interactions between the aluminide overcoat and the various bond coats and the potential for creep of the relatively weak aluminide layer to nullify the effect of the strong bond coats. To eliminate this effect, a recent study at GE (37) evaluated different bond coat creep strengths produced by applying various heat treatments to the same bond coat (Bond Coat No. 4). In this study, bond coat No. 4 was heated in vacuum at each of four temperatures, 1079°C (1975°F), 1148°C (2100°F), 1204°C (2200°F), and 1260°C (2300°F). The creep strength of the bond coat heat treated at these temperatures varies by approximately 5 Larson-Miller parameter units. The bond coat was also given the aluminide overcoat (after vacuum heat treatment) prior to the top coat application. The thermal cycle lives of these specimens and similar specimens not given the bond coat heat treatment are shown in Figure 21. The results indicate that TBC thermal cycle test life increases with heat treatment temperature (and creep strength), indicating that creep strength of the bond coat does indeed influence TBC life. The beneficial effect was not observed on specimens with bond coats treated at 1260°C (2300°F). This very high temperature may have resulted in rapid loss of strengthening elements from the bond coat by diffusion into the substrate.

3.5 Other Efforts

Another experiment was run using disk (button) specimens, in which coating variations included thicker than standard bond coats and top coats, and larger diameter disks. Testing variations included furnace cycle testing and burner rig (JETS) testing. The specific variations included in the experiment are given in Table V. The goals of these tests were to (1) evaluate the effect of bond coat creep through different bond coat thicknesses, and (2) evaluate the effect of different strains resulting from different top coat thicknesses and specimen diameters.

Results from the furnace cycle test are shown in Figures 22 and 23. The thermal cycle life of the disk test specimens was evaluated to both 10% and 20% spallation as the failure criteria

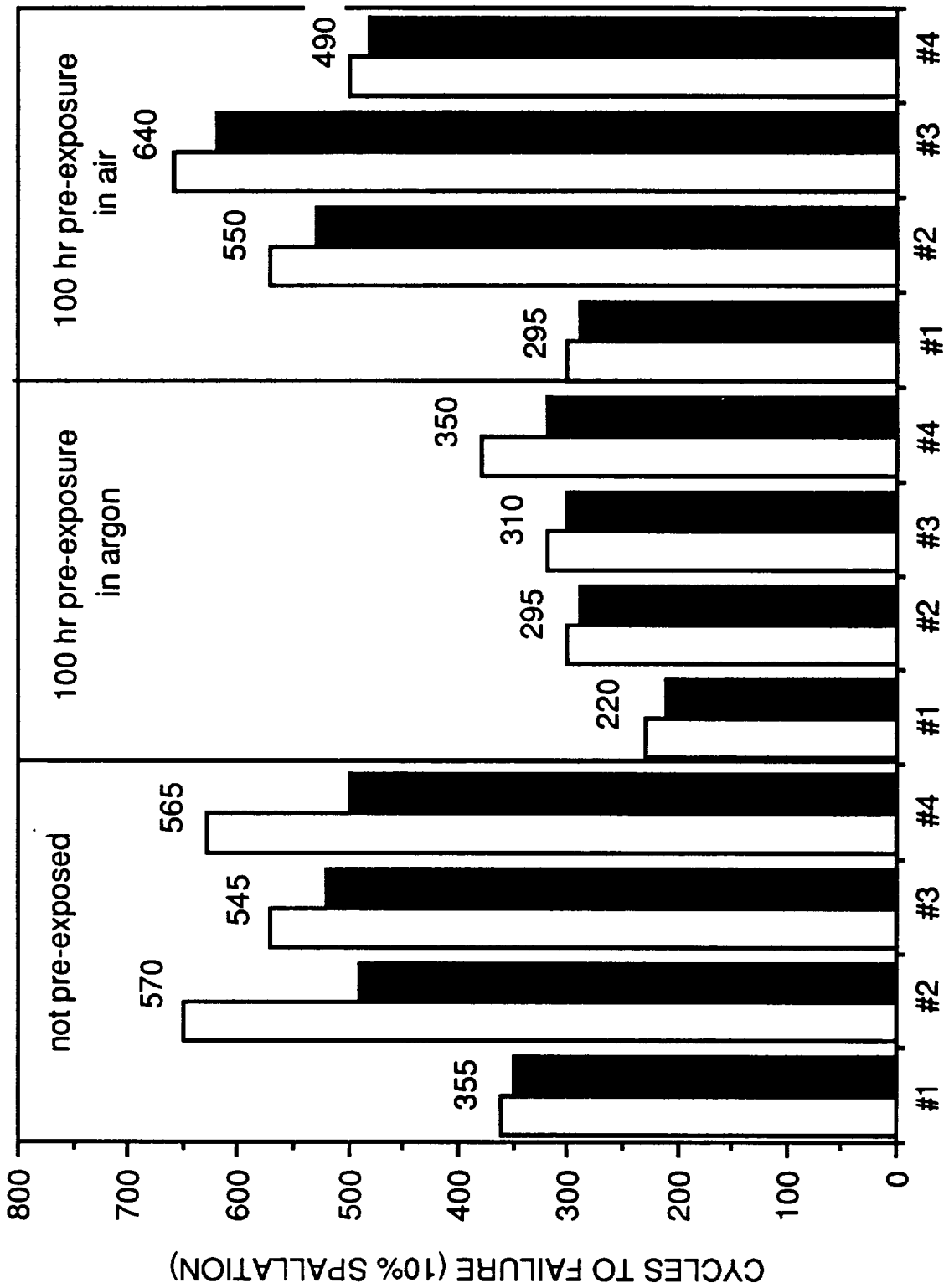

Figure 20. Furnace Cycle Test (1093°C) Lives of Specimens Coated with Various TBC Systems for Evaluating Bond Coat Creep Effects (see Table IV for Description of TBC Systems). (Numbers Above the Bars are Averages.)

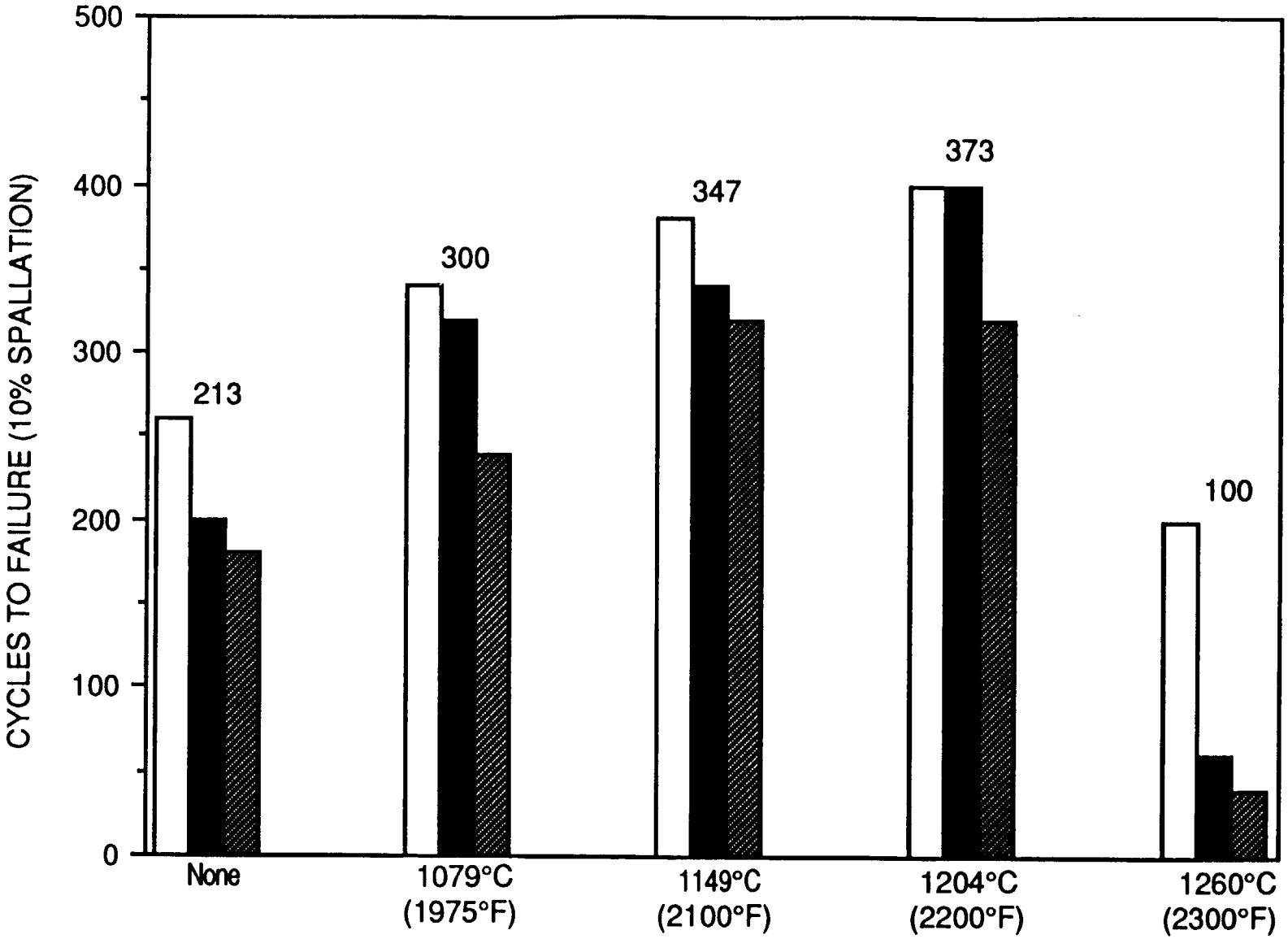

Figure 21. Effect of Heat Treatment of Bond Coat No. 4 on Thermal Cycle Life of TBC (René N4/Bond Coat No. 4/Aluminide/ZrO_2-Y_2O_3). Furnace Cycle Test at 1135°C (2075°F).(Numbers Above the Bars are Averages.)

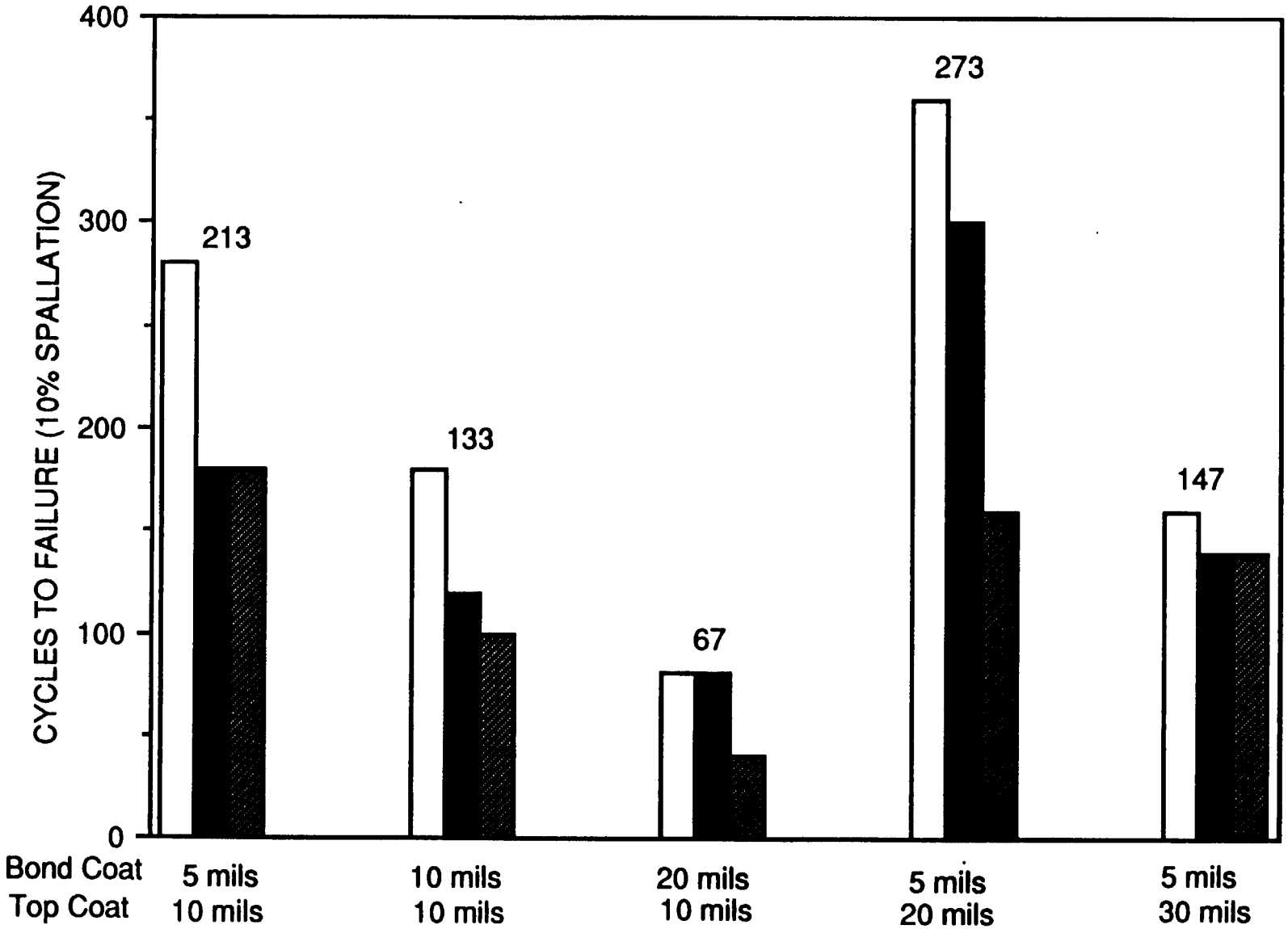

Figure 22. Furnace Cycle Test (1093°C) Life to 10% Coating Loss for Specimens with Various Coating Layer Thicknesses. Button Specimens Coated on One Face with LPPS NiCrAlY and APS ZrO_2-8%Y_2O_3. (Numbers Above the Bars are Averages.)

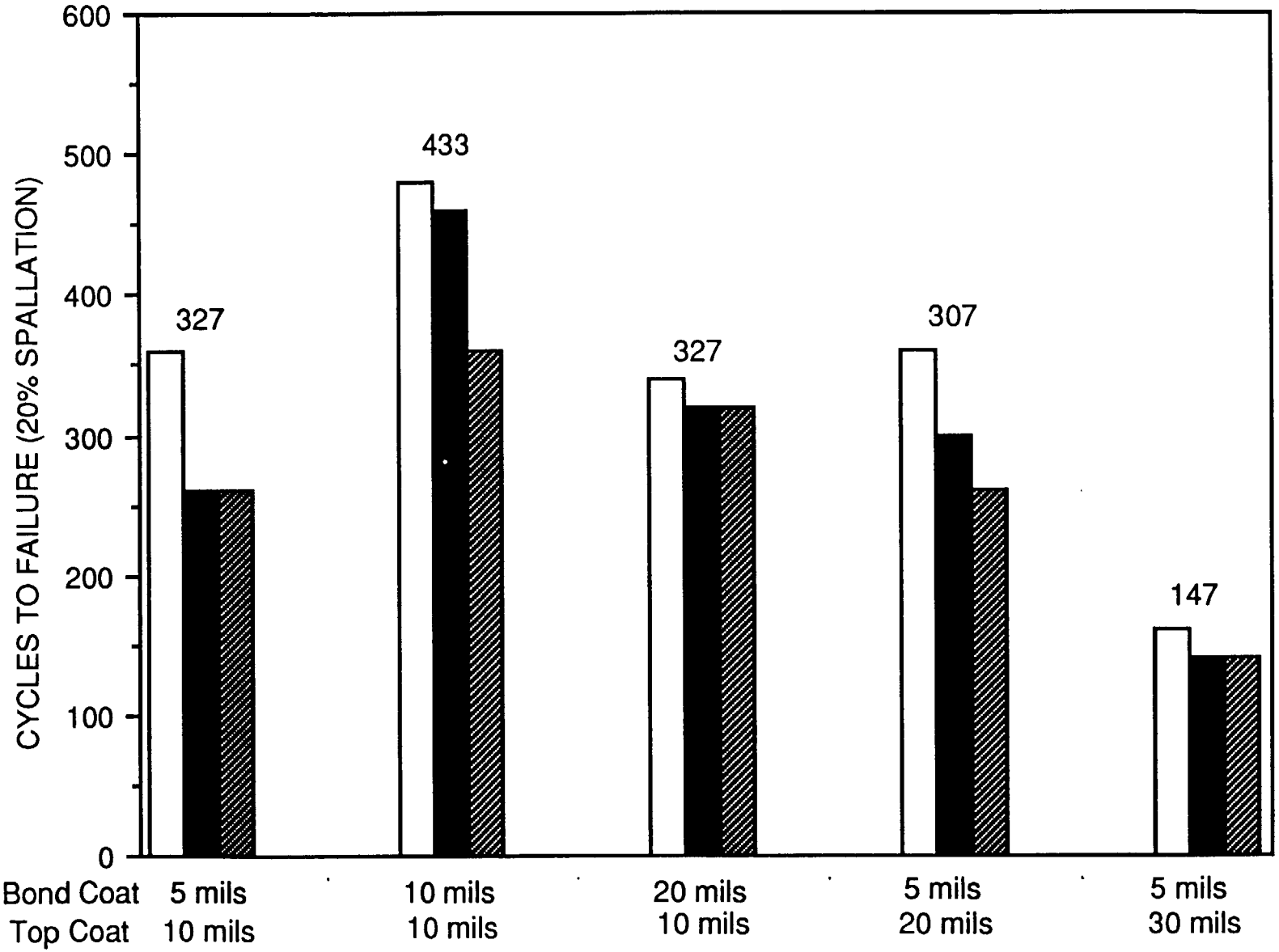

Figure 23. Furnace Cycle Test (1093°C) Life to 20% Coating Loss for Specimens with Various Coating Layer Thicknesses. Button Specimens Coated on One Face with LPPS NiCrAlY and APS ZrO_2-8%Y_2O_3. (Numbers Above the Bars are Averages.)

Table V. Specimen, Coating, and Testing Variations.

Specimen No.	Bond Thickness, mm	Top Coat Thickness, mm	Specimen Diameter, cm	Substrate Material	Number of Specimens	
					JETS Test	Furnace Cycle Test
1	0.13	0.25	2.54	René 80	1	3
2	0.25	0.25	2.54	René 80	1	3
3	0.51	0.25	2.54	René 80	1	3
4	0.13	0.51	2.54	René 80	1	3
5	0.13	0.76	2.54	René 80	1	3
6	0.13	0.25	2.54	Hastelloy X	1	--
7	0.13	0.25	3.18	Hastelloy X	1	--
8	0.13	0.25	3.81	Hastelloy X	1	--

in the furnace cycle test (10 minute heat up, 45 minutes at 1093°C, 10 minute cool). Normally, there are only small differences in ranking when the specimens are evaluated at the two failure criteria; however, in this experiment, the results from the two different criteria yield different conclusions. The 10% spallation failure criterion indicates that thermal cycle life decreases with increasing bond coat thickness, while the 20% failure criteria indicates that bond coat thickness does not significantly affect thermal cycle life. In general (except in the case of the 0.051 mm (0.20 inch) top coat, 10 failure criterion), the results indicate that thermal cycle life decreases with increasing top coat thickness. However, it was not anticipated that this essentially isothermal test would discriminate between ceramic thicknesses to the extent that the highly cyclic JETS test would.

JETS testing (30 second heat up, no hold time, 30 second cool down) through 18,000 cycles was performed. In this test, the face of the button specimen is heated by a propane-oxygen flame, while an air blast is used on the back of the specimen to develop large gradients across the ceramic. Two air blasts, one on each side, are then imposed on the specimens at the cooling station. The specimen cools down to approximately 250°C. The average peak face and back temperatures for each specimen at the heating station are shown in Table VI (note that the face temperatures and thermal gradients were changed at 5,000, 16,000, and 20,000 cycles to allow completion of the test in a reasonable period of time). The results in Table VII show the amount of spallation after each 1,000 cycles. The JETS test clearly demonstrates the strong dependence of thermal cycle life on top coat thickness and coating edges. Comparison of TBC specimens with 0.25, 0.51, and 0.76 mm thick top coats clearly showed that TBC life decreases with increasing ceramic thickness. Comparison of TBC specimens with 2.54, 3.18 and 3.81 cm

Table VI. Specimen Temperature During JETS Test[a]

Specimen Number	Cycles 0-5,000 Average Temperatures (°C)		Cycles 5,000-16,000 Average Temperatures (°C)		Cycles 16,000-20,000 Average Temperatures (°C)		Cycles 20,000-27,000 Average Temperatures (°C)	
	Face	Back	Face	Back	Face	Back	Face	Back
1	1395	925	1450	995	1480	925	1515	990
2	1420	930	1465	995	1510	925	---	---
3	1355	930	1430	990	1500	930	---	---
4	1485	925	---	---	---	---	---	---
5	1490	880	---	---	---	---	---	---
6	1395	925	1450	985	1505	945	1520	1015
7	1400	910	1460	990	1505	930	1510	990
8	1375	880	1430	950	1495	920	1515	980

[a]Specimens cool to about 260°C

Table VII. Coating Loss During JETS Test, Percent Spallation (Surface Area)[a]

Specimen #	Cycles x 10^{-3}																										
	1	2	3	4	5	6	7	8	9	10	11	12	13	14	15	16	17	18	19	20	21	22	23	24	25	26	27
1	--	--	--	--	--	--	--	--	--	--	--	--	--	--	--	--	1	2	6	6	13	17	17	23			
2	--	--	--	--	--	--	--	--	5	13	14	17	18	18	18	18	18	18	18	20							
3	--	--	--	--	--	--	--	--	--	--	--	--	--	--	1												
4	(b)	2	8	12	22																						
5	(b)	45																									
6	--	--	--	--	--	--	--	--	--	--	--	--	--	--	5	5	9	9	9	12	13	13	13	13	20		
7	--	--	--	--	--	--	--	--	--	--	--	--	--	--	--	--	--	--	--	--	--	1	3	3	3	3	4
8	--	--	--	--	--	--	--	--	--	--	--	--	--	--	--	--	--	--	--	--	(c)	(c)	(c)	(c)	(c)	(c)	(c)

(a) Specimen is removed at 20% spallation
(b) Bondline cracks at edge of specimen
(c) Pin holes in center of top coat (surface)

Table VIII. Effect of Specimen Size (Diameter) on Edge Temperature.

Specimen Diameter cm (in)	Face Temperatures °C (°F)		Back Temperature °C (°F)
	Center	Edge	Center
2.54 (1.00)	1488 (2710)	1441 (2625)	921 (1690)
3.18 (1.25)	1510 (2750)	1399 (2550)	918 (1685)
3.81 (1.50)	1499 (2730)	1224 (2235)	913 (1675)

diameters clearly showed that life was extended as the edge of the specimen moved away from the hot spot resulting in lower edge temperatures. The temperature of the edges and center at one JETS setting are given in Table VIII. Lower temperatures at the high stress location (edges) thus results in lower stresses and longer life. The results also indicate that bond coat thickness is not significant in this test, which would be expected since elevated temperature duration for the substrate is minimal and therefore oxidation is also minimal.

3.6 Key Property Determinations

To provide data useful to the modeling to be performed later in this study, several physical and mechanical properties of the bond coat and top coat layers were measured.

3.6.1 Bond Coat Properties

Tensile strength, Poisson's ratio, dynamic elastic modulus, and coefficient of thermal expansion were determined from room temperature to approximately 1093°C (2000°F). Standard testing procedures and test specimens (Figure 24) were utilized for the NiCrAlY bond coat specimens. These specimens were machined from 5.1 cm (2 inch) by 15.2 cm (6 inch) heat treated LPPS NiCrAlY billets of various heights. The as-sprayed billets received a 4 hour vacuum heat treatment at 1093°C (2000°F) to increase the machinability of the billets. The 1093°C heat treatment was chosen since this is the soak temperature utilized in thermal cycle testing.

Tensile Strength - Tensile strength was determined at room temperature, 538°C (1000°F), 760°C (1400°F), 982°C (1800°F), and 1093°C (2000°F). Strain rate was 0.0005 in./in./min. through 0.2% yield, then a cross head speed of 0.03 in./min. (0.013 mm/sec.) to failure. Some difficulties were encountered when testing at room temperature where NiCrAlY is extremely brittle; two of the three test specimens failed in the grips. A summary of the test results is listed in Table IX.

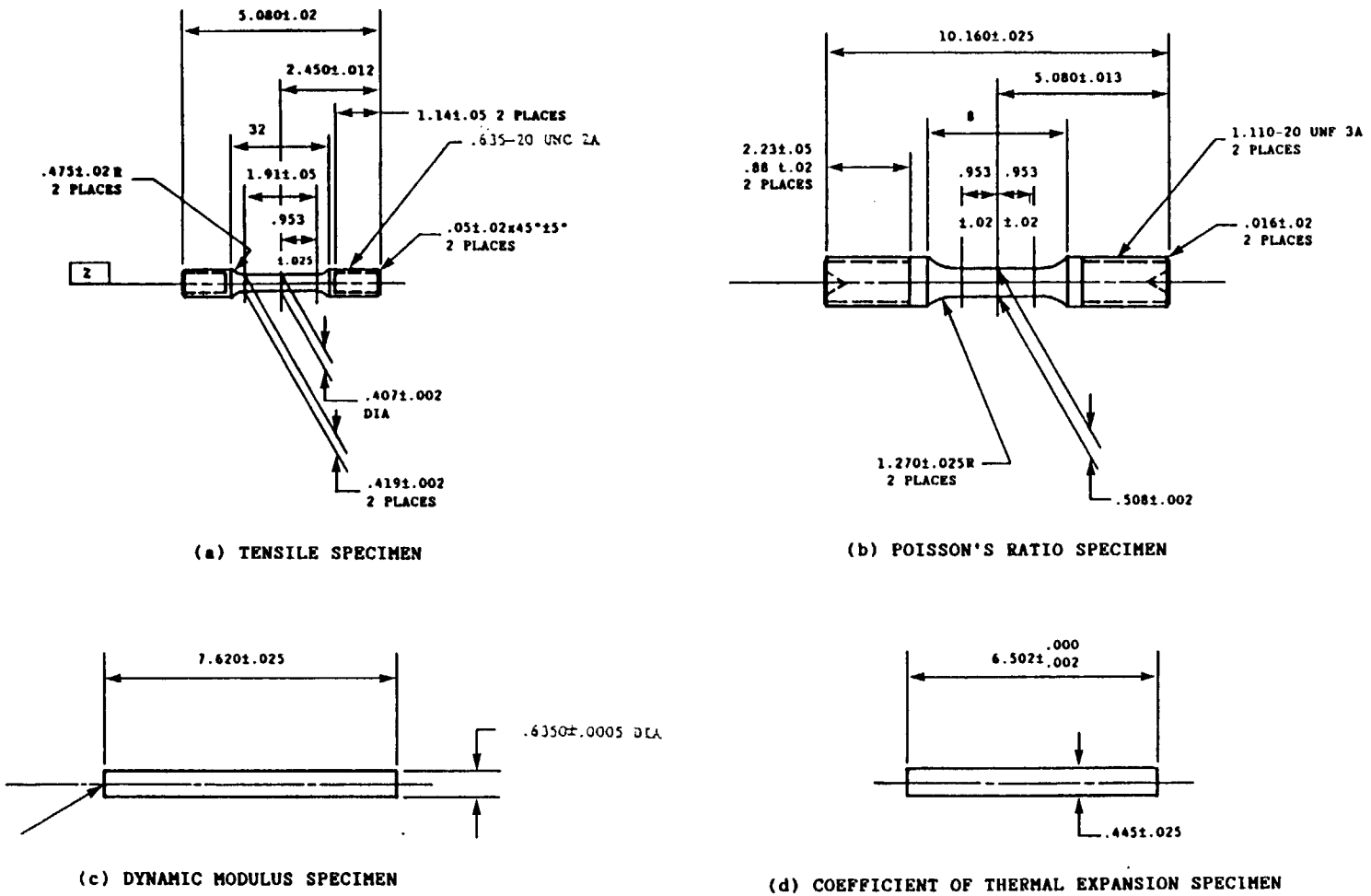

Figure 24. Specimen Configurations for Determining Properties of Bond Coat (All Dimensions in Centimeters).

Table IX. LPPS Ni-22Cr-10Al-0.3Y Bond Coat.

Test Temperature	Ultimate Strength MPa	0.2% Yield MPa	% Elongation	% Reduction in Area
Ambient 25° (77°F)[a]	1320 (191 ksi)	---	---	---
538°C (1000°F)[b]	1240 (179 ksi)	1120 (162 ksi)	5.2	6.2
760°C (1400°F)[b]	450 (65 ksi)	160 (23 ksi)	18.3	19.6
982°C (1800°F)[c]	16 (2.3 ksi)	13 (1.9 ksi)	149.3	95.6
1093°C (2000°F)[c]	4 (0.6 ksi)	3 (0.4 ksi)	248.3	92.4

[a]No measurable plastic deformation (1 specimen).
[b]Average of three test specimens.
[c]Average of two test specimens.

Poisson's Ratio - Poisson's ratio was determined at room temperature, 538°C (1000°F), and 760°C (1400°F) (Table X). Attempts were also made to obtain values at 982°C (1800°F), and at 1093°C (2000°F). However, due to the extremely ductile nature of the NiCrAlY material, the elastic region was not measurable at the elevated temperatures. A Poisson's ratio of 0.5 will be assumed for these temperatures, based on the laws of plasticity.

Dynamic Elastic Modulus - The dynamic elastic modulus was determined from room temperature to approximately 1075°C for two different specimens. A plot of the results for both specimens is shown in Figure 25. The dynamic elastic modulus varies from 200 GN/m^2 at room temperature to 20 GN/m^2 at 1075°C.

Coefficient of Thermal Expansion - Coefficient of thermal expansion was determined using the Chevenard dilatometer. The coefficient varies from approximately 11 x 10^{-6}/°C at room temperature to about 18 x 10^{-6}/°C at 1000°C (Figure 26). The same values were obtained when heating and cooling the specimens.

3.6.2 Top Coat Properties

Elastic modulus, shear modulus, Poisson's ratio, flexural (bend) strength, and coefficient of thermal expansion were determined for the top coat. These properties were determined from room temperature to approximately 1093°C (2000°F). In all tests, free-standing air plasma-sprayed (APS) specimens were utilized. Free-standing specimens were produced by depositing the ceramic material on stainless steel substrates and inducing a thermal shock to cause spallation of the intact ceramic sheet. Some final machining was required to achieve the desired specimen configurations (Figure 27). These specimens received a 4-hour heat treatment in air at 1093°C (2000°F) prior to testing.

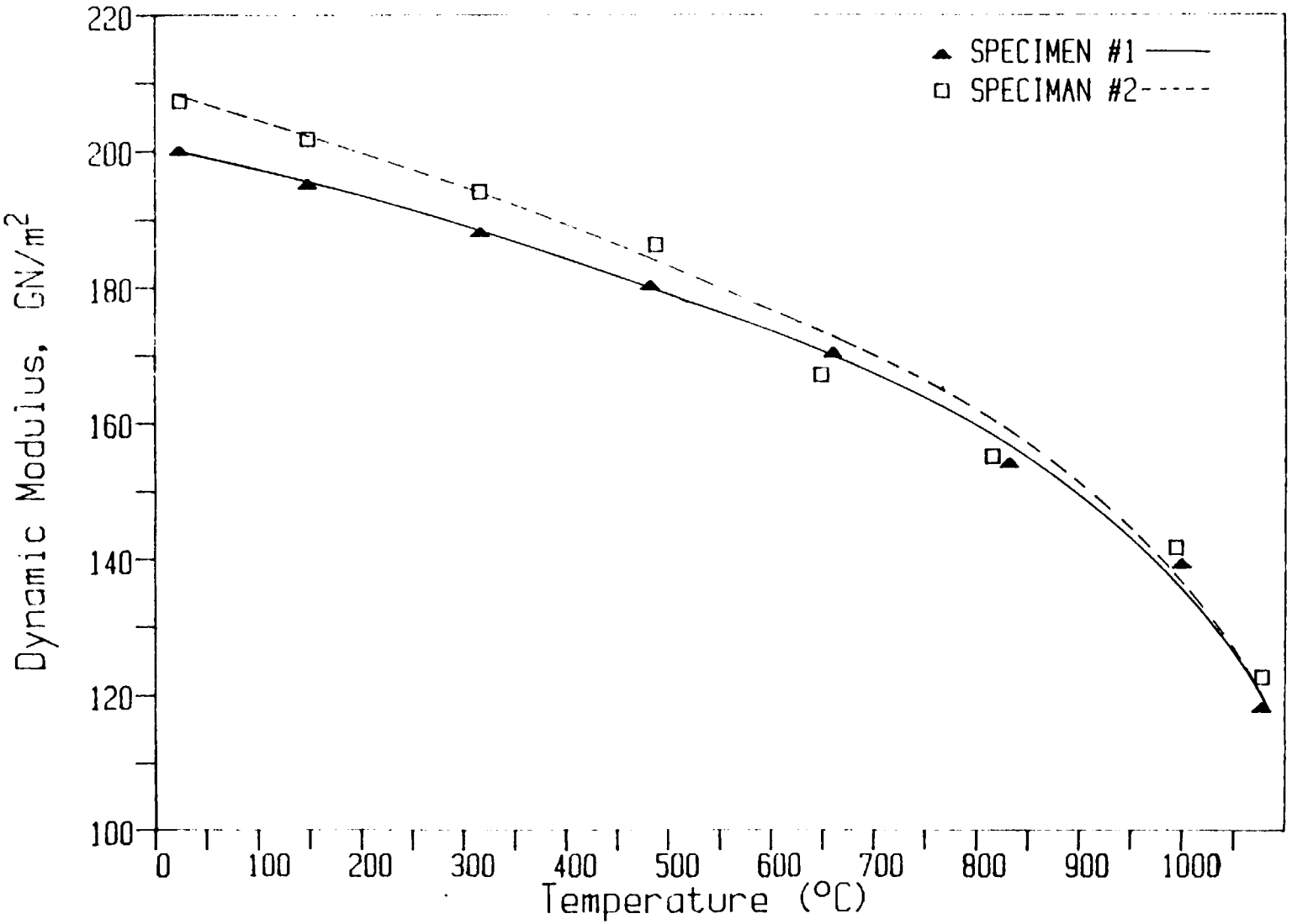

Figure 25. Dynamic Elastic Modulus of LPPS Ni-22Cr-10Al-0.3Y Bond Coat).

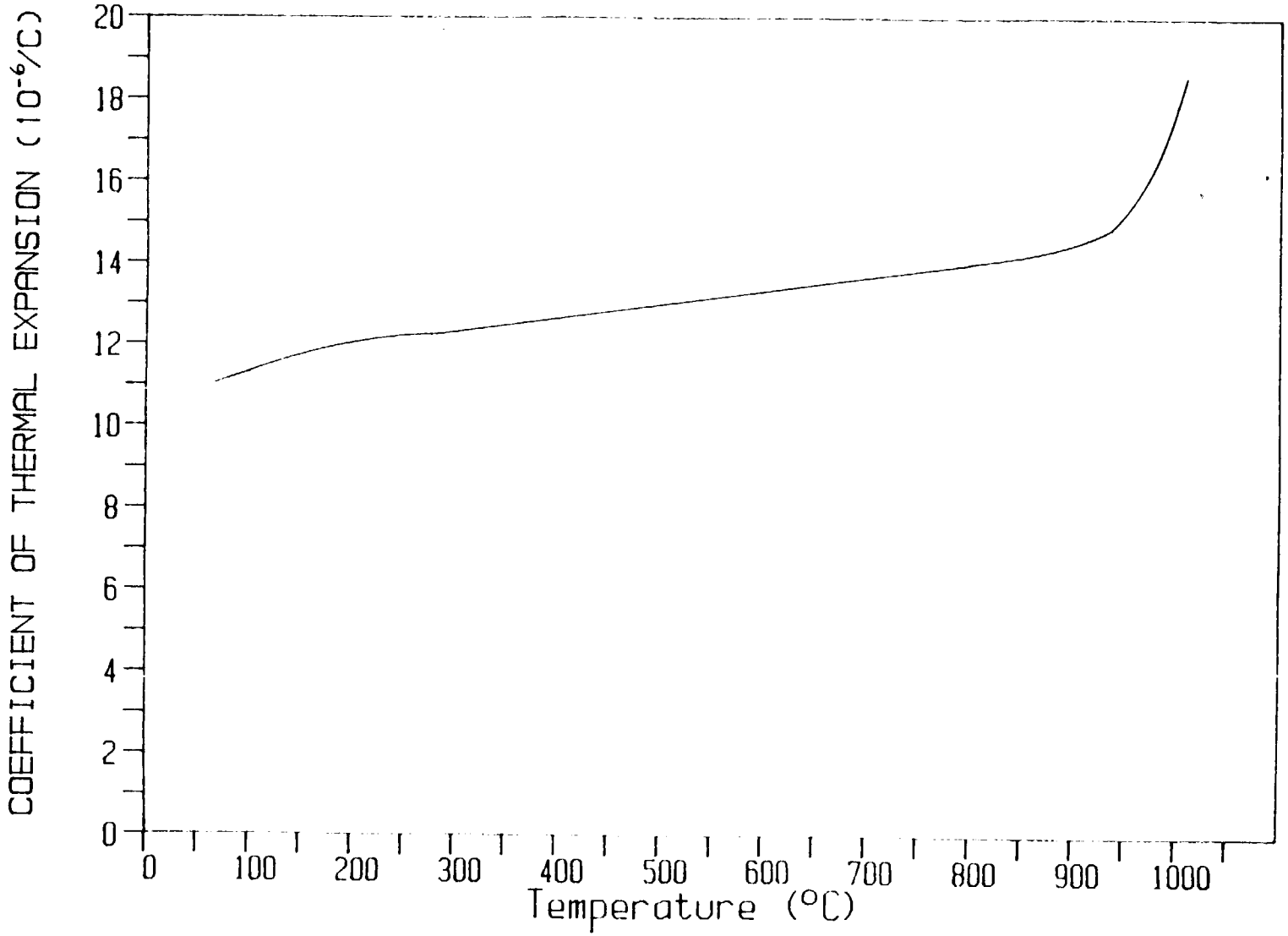

Figure 26. Thermal Expansion Results for LPPS Ni-22Cr-10Al-0.3Y Bond Coat.

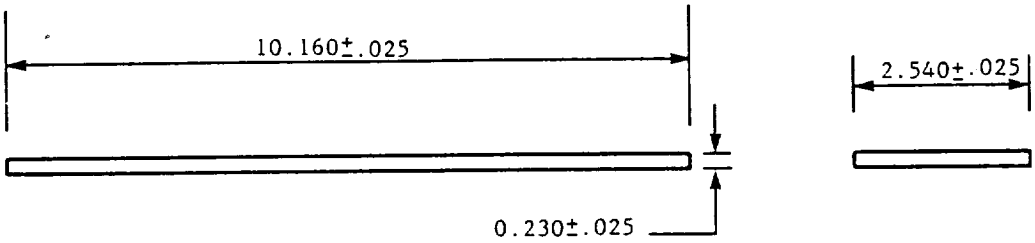

(a) DYNAMIC MODULUS AND POISSON'S RATIO SPECIMEN

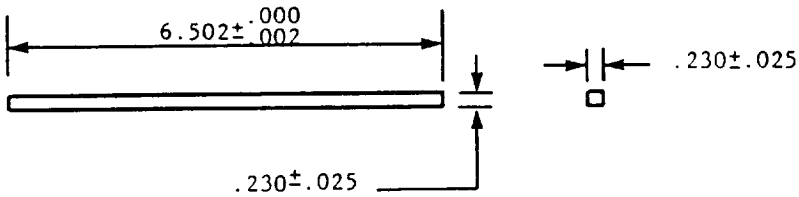

(b) COEFFICIENT OF THERMAL EXPANSION SPECIMEN

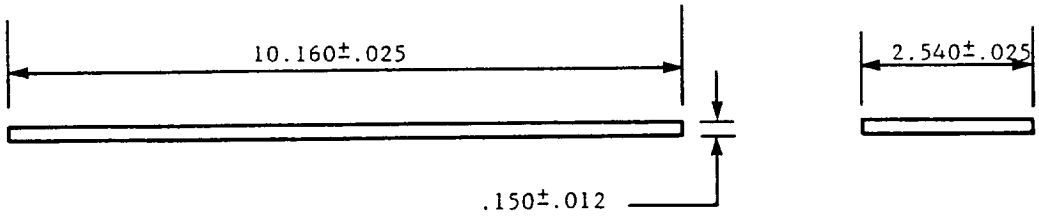

(c) BEND STRENGTH SPECIMEN

Figure 27. Specimen Configurations for Determining Properties of Top Coat (All Dimensions in Centimeters).

Table X. Elastic Moduli and Poisson's Ratio of LPPS Ni-22Cr-10Al-0.3Y.

Temperature°C	E (Axial) GPa	E (Diametral) GPa	Poisson's Ratio
20 (R.T.)	206 (29.9 MSI)	696 (100.8 MSI)	0.30
538 (1000°F)	180 (26.1 MSI)	602 (87.3 MSI)	0.30
760 (1400°F)	101 (14.7 MSI)	273 (39.6 MSI)	0.37
982 (1800°F)	---	---	---[a]
1093 (2000°F)	---	---	---[a]

[a]No linear portion to stress/strain curves.

Elastic Modulus, Shear Modulus, and Poisson's Ratio - The apparatus and methodology used for measurement of elastic modulus, shear modulus, and Poisson's ratio of the ceramic specimen conform to that of Spinner and Tefft (38).

The dynamic elastic and dynamic shear moduli were measured continuously from room temperature to 1093°C (2000°F) by a resonant frequency method*. Poisson's ratio (ν) was then calculated from the elastic and shear moduli.The values measured for elastic modulus and shear modulus, and calculated for Poisson's ratio are shown in Table XI.

A four-point (quarter flex) bend test was performed on specimen No. 1 to allow comparison of elastic modulus values measured from this test to the values measured from the resonant frequency test. Specimen No. 1 was sectioned into three flex specimens (nominally 0.635 cm x 0.229 cm x 6.35 cm) and strain gages attached. The average elastic modulus determined at room temperature was 20.6 GPa (2.99×10^6 psi), (Table XII). This average value is a factor of 10 less than the values measured by the resonant frequency method. The difference is possibly associated with the presence of cracks, porosity, and splats decreasing the apparent modulus in the bend test. These factors should play a smaller role in the resonant frequency method.

Flexural (Bend) Strength - Elevated flexural (four-point) bend tests were performed at Southern Research Institute on plasma-sprayed ZrO_2-$8Y_2O_3$. The results indicate (Table XIII) that flexural strength decreases from 44.2 MPa (6 ksi) at 20°C (70°F) to 27.7 MPa at 538°C (1000°F) and remains relatively constant at about 27.7 MPa from 538°C to 1093°C

*Testing performed at IIT Research Institute, Chicago, Illinois.

Table XI. Elevated Temperature Determination of Elastic Modulus, Shear Modulus, and Poisson's Ratio of APS ZrO_2-8%Y_2O_3.

Temp., °C	Resonant Frequency		E Elastic Modulus GPa (Msi)	G Shear Modulus GPa (Msi)	Poisson's Ratios
	Flexural	Torsional			
25[a]	1472	3697	210 (30.5)	91 (13.2)	0.15
25	1466	3672	208 (30.2)	90 (13.1)	0.16
100	1453	3630	205 (29.7)	88 (12.8)	0.16
150	1444	3610	202 (29.3)	87 (12.6)	0.16
200	1436	3573	200 (29.0)	86 (12.4)	0.17
300	1425	3443	197 (28.6)	79 (11.5)	0.24
400	1412	3343	193 (28.0)	75 (10.8)	0.29
450	1411	3325	193 (28.0)	74 (10.7)	0.31
500	1401	3299	190 (27.6)	72 (10.5)	0.31
538	1395	3281	189 (27.4)	72 (10.4)	0.31
600	1387	3265	187 (27.1)	71 (10.3)	0.31
700	1375	3209	184 (26.6)	69 (10.0)	0.33
800	1360	3160	179 (26.0)	67 (9.7)	0.34
900	1342	3135	175 (25.3)	66 (9.5)	0.33
982	1340	3122	175 (25.3)	65 (9.4)	0.34
1000	1362	3147	179 (26.1)	66 (9.6)	0.36
1038	1374	3163	183 (26.5)	67 (9.7)	0.37
1093	1342	3185	175 (25.3)	68 (9.8)	0.29

[a]Specimen suspended on cotton thread, all others suspended on Pt wire.

Table XII. Mechanical Properties of APS ZrO_2-8% Y_2O_3

Sample I.D.	Width, cm	Thickness, cm	Length, cm	Ultimate Load, Kg (lb)	Ultimate Stress MPa (ksi)	Strain to Failure in/in $\times 10^{-3}$	Elastic Modulus GPa (MSI)
1-1	0.648	0.238	5.746	7.03 (15.5)	53.3 (7.73)	2.89	19.9 (2.88)
1-2	0.648	0.235	5.747	6.21 (13.69)	56.7 (8.23)	3.07	20.1 (2.92)
1-3	0.648	0.232	5.746	5.26 (11.59)	49.3 (7.15)	2.59	21.7 (3.15)
					Average Elastic Modulus	20.6 ± 1.0	(2.99 ±0.15)

Table XIII. Flexural Properties of APS ZrO_2-8% Y_2O_3.

Temperature		Flexural Max. Load		Ultimate Flexural Strength		Total Midpoint Modulus		Deflection	
°C	(°F)	kg	(lb)	MPa	(psi)	GPa	(Msi)	mm	(inches)
20	(70)	11.34	(25.0)	44.2	(6410)	13.0	(1.89)	0.803	(0.0316)
538	(1000)	7.26	(16.0)	27.7	(4020)	13.0	(1.88)	0.668	(0.0263)
982	(1800)	7.71	(17.0)	30.0	(4350)	14.0	(2.03)	0.749	(0.0295)
1038	(1900)	6.80	(15.0)	26.5	(3850)	10.6	(1.54)	1.019	(0.0401)
1093	(2000)	6.21	(13.7)	17.1	(3480)	10.3	(1.49)	1.323	(0.0521)

(1000°F to 2000°F). The flexural modulus, however, remains constant at 13.0 GPa (1.9 Msi) from 20°C (70°F) to 982°C (1800°F) and then drops to 10.6 GPa (1.5 Msi) at 1038°C (1900°F).

Coefficient of Thermal Expansion - Coefficient of thermal expansion was determined using the Chevenard dilatometer from room temperature to 1073°C. Interestingly, the coefficient was essentially constant (Figure 28) over this temperature regime with a value of approximately 9×10^{-6}/°C. These results are quite similar to the results reported of DeMasi and Sheffler (39), but significantly different than those reported by Siemers (32).

3.7 Empirical TBC Life Prediction Model

An empirical TBC life prediction model was developed based on thermal cycle testing. The model (Figure 29), which predicts the life of a specimen in the furnace cycle test, includes parameters that take into account test temperature and several factors related to the test specimen. Among the specimen factors are (1) a geometry factor for button and cylindrical shapes, (2) a factor which compensates for whether the bond coat was deposited by the conventional (air) plasma spray or low-pressure plasma spray process, (3) a factor which corrects for the relative creep strength of the bond coat, and (4) factors which take into account the thickness of the oxide scale on the bond coat at the beginning of the test and at specimen failure. The factors used in the model are based on test results from this program and from internal programs. The geometry factors were based on the test results on tubular and button specimens shown in Figures 7, 14, and 20. These factors reflect the shorter coating life on tubes associated with their curvature. The bond coat application factor is based on internal test data on a TBC system with NiCrAlY bond coat where life was shortened by one half when specimens produced by air plasma spray were compared to where the bond coat was deposited by low pressure plasma spray. The bond coat creep factor is based on the results shown in Figures 7 and 20, and on data from an internal study of TBCs with bond coat No. 4 + Codep, NiCrAlY + Codep, and NiCrAlY bond coats tested at three temperatures (1093°, 1135° and 1177°C). In this model, NiCrAlY is assigned a creep factor of 1, while bond coat No. 4 is assigned a creep factor of 4. Bond coats with intermediate creep strengths are scaled between these values based on their creep strength. Therefore, based on creep strengths listed in Table IV, the bond coat creep factor is 3.1 for bond coat No.2, and 3.6 for bond coat No. 3. The decrease in life associated with pre-exposures in air at 1093°C (2000°F) is handled by the combination of oxide scale thicknesses after preoxidation and at failure. This combination allows determination of cycle life for pre-exposed specimens. This preoxidation term is based on data shown in Figures 7 and 8. Finally, the temperature factor is based on the same internal study used to determine the bond coat creep factor. This factor accounts for degradation in cycle life due to increased oxidation rates and other thermally activated phenomena as temperature increases. The data used to develop this model are labeled as correlation points and plotted against the predicted values in Figure 30. The model is a best fit of these correlation points.

Two approaches were planned to test the validity of the model. In one approach, other available data including those from other GE programs were evaluated using the model.

Figure 28. Thermal Expansion of APS ZrO_2-Y_2O_3 Top Coat.

$$\text{Cycle Life} = 400(GF)(CF)(TF)(BF) - 100(PF/FT)$$

Temperature(oxidation)Factor=TF

2000F=1

2075F=1/3

2150F=1/8

Bond Coat Creep Factor=CF

1−4(Function of bond coat creep strength −Larson Miller parameter)

Geometry Factor=GF

Button=1

Cylinder=1/3

Bond Coat Application Factor=BF

LPPS=1

APS=1/2

Pre−Oxidation Scale Thickness Factor=PF

Oxide Scale Thickness At Failure=FT

Figure 29. Empirical Life Prediction Model for TBCs (Model).

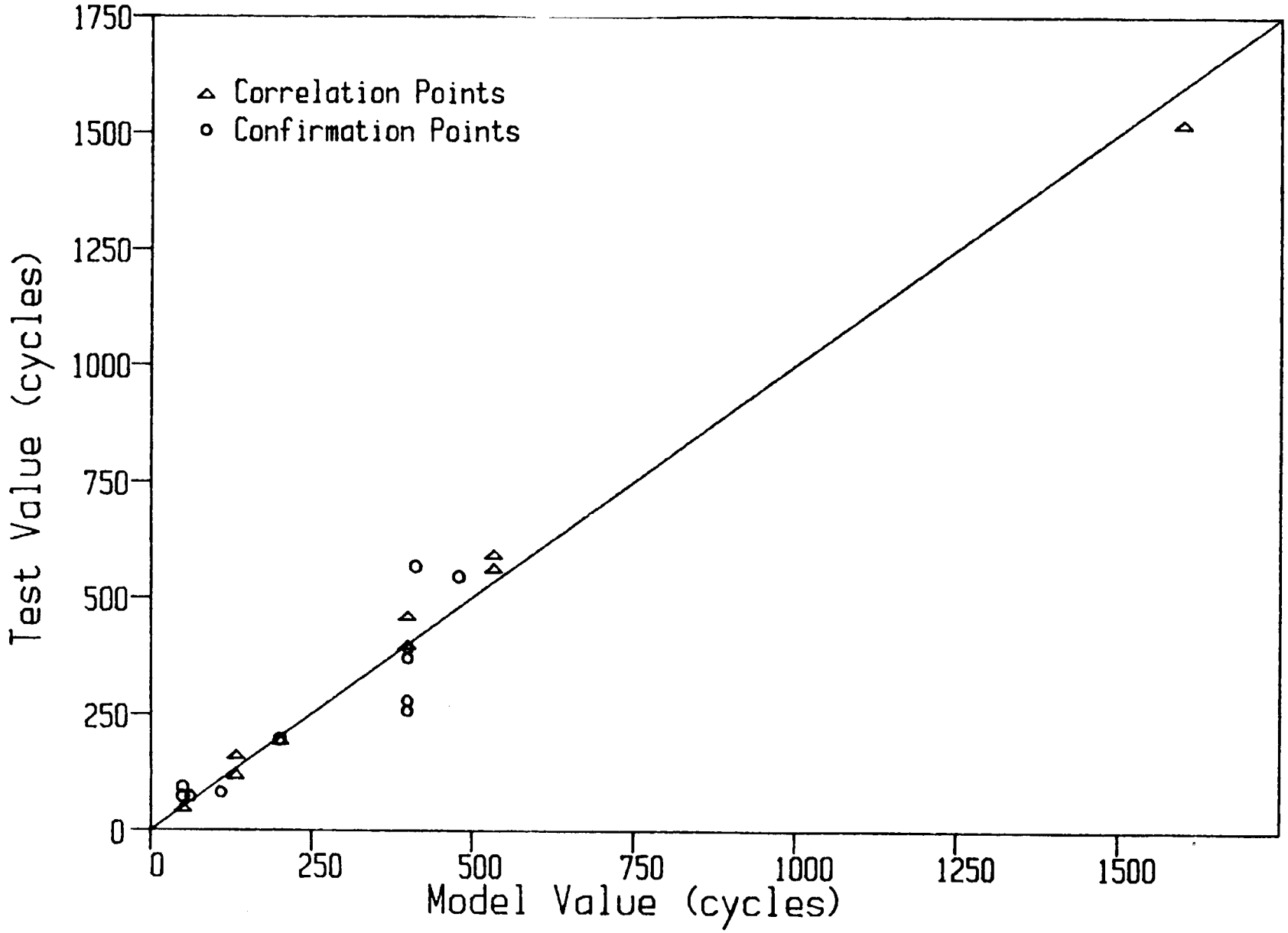

Figure 30. Empirical Life Prediction Model for TBCs (Test Vs Model Values).

These data are labeled as confirmation points in Figure 30 and indicate good agreement between predicted and actual values.

The second approach planned was to use the model to predict the life of a TBC using a bond coat that has similar oxidation resistance to NiCrAlY but a slightly higher creep strength. Since this bond coat had never been tested before, the goal was to test the model against a new TBC. Three attempts were made to apply this special bond coat, but in each case high levels of porosity occurred. Thermal cycle testing was performed on specimens from one coating run. As expected, the high levels of porosity resulted in shortened thermal cycle life (less than 100 cycles). The early failure was attributed to significant oxidation of the bond coat, thus a reasonable test of the life prediction model was not obtained by this approach.

The good agreement between predicted and actual values for existing data is promising. However, it is also disappointing that the new TBC system could not be utilized to further test this model. The advantage of this model is that it is simple to use and may be useful in initial predictions, prior to more comprehensive modeling (Task II modeling).

4.0 TASK II - MAJOR MODE LIFE PREDICTION MODEL

The objective of this task was to develop life prediction models for the plasma-sprayed TBC system. To accomplish this goal, finite element analyses were performed on the TBCs, and experiments were run to evaluate their thermomechanical characteristics. A life prediction model was developed based on the physical evidence accumulated during testing and the results of the finite element analysis.

4.1 TBC Finite Element Analysis

The analysis of the TBC specimen geometries was carried out using the finite element program CYANIDE (Cyclic Analysis of Inelastic Deformation). This is a finite element computer code with cyclic incremental plasticity and creep capability that has been developed at GE. The solution method used by CYANIDE is a right hand side method, meaning that the plasticity and creep response is included by the application of pseudo forces calculated from the plastic and creep strains. As a constitutive model, the plasticity analysis uses the Besseling subvolume method; the creep analysis can be performed using time hardening, strain hardening, or life fraction rules with a two-term creep equation modeling primary and secondary creep. For this program a strain hardening creep analysis was used, meaning that movement between creep curves at various stress levels is based on movement along a constant strain line. A more complete description of the code and its features is given in Appendix C.

The first finite element analysis which was carried out examined the stresses that occur during the fabrication cycle. This effort modeled the successive states of the specimens as they were coated, and showed that a considerable residual stress state exists in the fabricated specimen. Residual stresses exist in coated specimens because of the difference in thermal expansivities of the various materials involved. Consider a simple process in which the base metal is heated to some temperature (approximately 982°C), molten metallic coating material is applied to the base metal, then the coated metal is cooled to room temperature. If it is assumed that the part is stress free at the temperature at which the metallic coating material is applied, residual stresses will exist at room temperature. Subsequently, the part is heated to a different temperature (approximately 200°C), molten ceramic applied, then cooled to room temperature. If the ceramic coating is stress free at 200°C, it will be in a stressed state at room temperature, and the residual stresses that exist in the base metal and metallic coating layer are now different from what they were prior to the addition of the ceramic coating layer. The results of the analysis of stresses occuring during the fabrication process are given in Appendix D.

Because the initial state of stress in the TBC specimens is significant, it is important that its effect be included in the thermal cycle analysis. This could be done by incorporating an initial stress into the model but it is more economical to use the method of stress-free reference temperature. The stress-free reference temperature technique accounts for a residual stress/strain field due to the application of coatings at different temperatures without explicitly modeling the manufacturing process. The stress-free reference temperature technique

subtracts from the calculated thermal strain at any given temperature the calculated thermal strain at the stress-free temperature.

The stress-free reference temperature for a two-material system is computed using the equation:

$$\Delta T_{NR} = T_{NR} - T_R = \frac{\alpha_c - \alpha_s}{\alpha_{NR}} (T_{SF} - T_R), \qquad (4\text{-}1)$$

where

T_{NR} = Stress-free reference temperature
T_R = Reference temperature for thermal strain determination
T_{SF} = Stress-free temperature
α_c = Thermal expansion coefficient of the coating at T_{SF}
α_s = Thermal expansion coefficient of the substrate at T_{SF}
α_{NR} = Thermal expansion coefficient of the coating at T_{NR}

Equation (4-1) contains two unknowns, T_{NR} and α_{NR}, but the thermal expansion as a function of temperature is known. For present purposes, α_{NR} and T_{NR} are assumed to be linearly related; α_{NR} can then be expressed in terms of T_{NR} by linear interpolation. Hence, the equation becomes a quadratic equation of T_{NR} and can be solved easily. An example of the calculation of the stress-free reference temperature is given in Appendix G.

The analysis of the TBC coatings in Task II involved two basic configurations: a 1.3 cm OD tube and a 2.54 cm diameter button. Each of these geometries was analyzed with various differences in bond coat thickness, top coat thickness, and presence or absence of oxide scale. The effect of a chamfered top coat edge compared to a vertical edge was also investigated.

The cylindrical tube specimen modeled is shown in Figure 1. A typical finite element mesh using axisymmetric elements modeling this specimen is shown in Figure 31. The mesh was refined in the region of greatest interest (i.e. the top coat/bond coat interface) and was made coarse in areas far from this which were not of interest. The left end of the tube model was constrained from axial displacement.

Due to a present limitation in CYANIDE to a maximum of three materials, it was not possible to directly model the substrate, bond coat, oxide scale, and top coat, each as separate materials. However, it was found in some earlier analyses that accurate calculation of the top coat strain field could be obtained when substrate properties were substituted for the bond coat. Therefore, this was done in the Task II analyses in order that the effect of oxide scale presence could be included directly.

In those cases where the oxide scale was explicitly used in the analysis, this was accomplished by inserting several rows of very narrow elements at the top coat/bond coat interface. These elements displaced the top coat outward without introducing any stress that

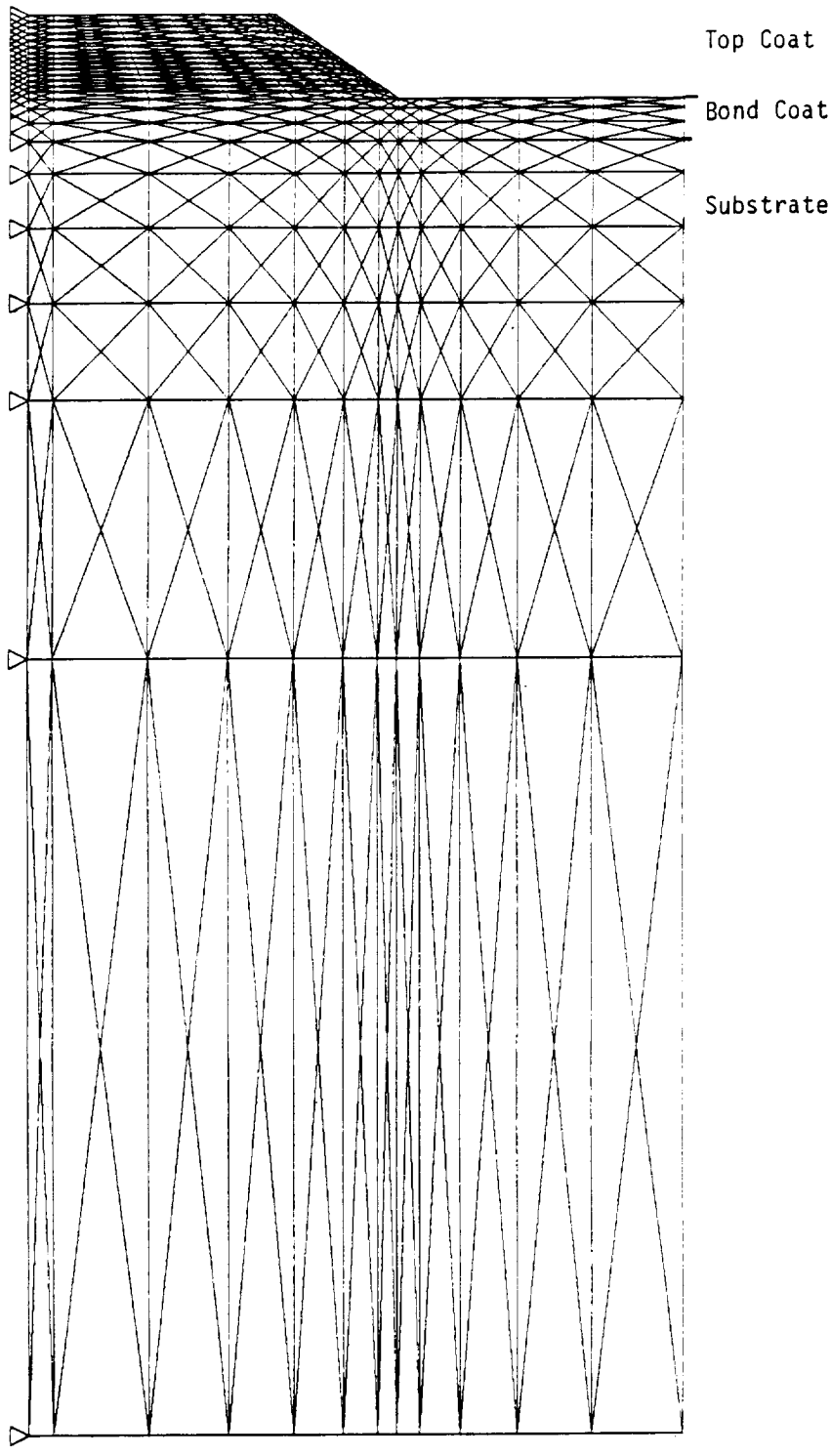

Figure 31. Finite Element Mesh for Thermal Barrier Coated Tubular Specimens.

might be expected to occur as a result of oxide scale growth at the interface. In order to model the growth of the oxide scale, it would be necessary to introduce some type of constraint into the finite element code. Carrying out such an analysis would require modifications beyond the scope of this contract.

The material properties used in the analyses are given in Appendix E. These were obtained from the references noted since the property data generated as a part of this program was not available when the analyses were started. For consistency, the same values were used throughout the analyses.

No mechanical loads were applied in the model. The loading was thermal only under the conditions of the furnace test cycle shown in Figure 32. The René 80 substrate and bond coat were allowed to undergo plastic deformation as well as creep whereas the top coating was assumed to creep only. The creep data of Hebsur and Miner (40) for NiCrAlY and the data of Firestone, et al. (41) for plasma-sprayed zirconia was used in these computations. It was found, however, that the plastic deformation of the substrate and bond coat was quite small.

The most severely strained top coat element was located at the top coat edge on the top coat/bond coat interface. The stress/strain history of this element was extracted from the finite element results and correlation of the stress and strain ranges with the observed failure mechanisms and times of the experimental specimens was examined.

The best correlation between analytical and experimental results was with normal and shear total strain ranges in the top coat at the maximum severity location. (Since this is an axisymmetric model, the normal strain is perpendicular to the bond while the shear strain component is parallel to it; total is used to connotate the sum of the elastic, plastic, and creep strains.) Figures 33 and 34 compare the difference in results obtained for the tube with and without a 4 micron oxide scale layer and a 0.25 mm (0.01 inch) top coat thickness, and also for a 0.75 mm (0.03 inch) top coat thickness with no scale [Appendix F contains more figures showing results for stress and creep strains]. It can be seen that in this case the presence of scale reduces the strain range. The reason for this appears to be in the differences in thermal expansion coefficients. It can be noted that the bond coat and René 80 substrate properties, shown in Appendix E, are fairly similar, while the top coat thermal expansion coefficients are very different from the bond coat but similar to the oxide scale thermal expansion coefficients. Thus, when oxide scale is present, the disparity between the top coat and bond coat expansions seems to be partially taken up by the scale, reducing the stress/strain state in the top coat. The thermal mismatch strains are the driving force in this specimen so the lower the mismatch, the less creep is observed.

Thus, when oxide scale is present, the severe mismatch in thermal expansion coefficients is not directly at the top coat interface, but occurs at the bond coat and oxide scale interface. This will begin to alleviate the strain in the top coat due to the attenuation of this mismatch through the scale. This effect of the scale was modeled using a separate layer of elements with elastic material properties for the scale.

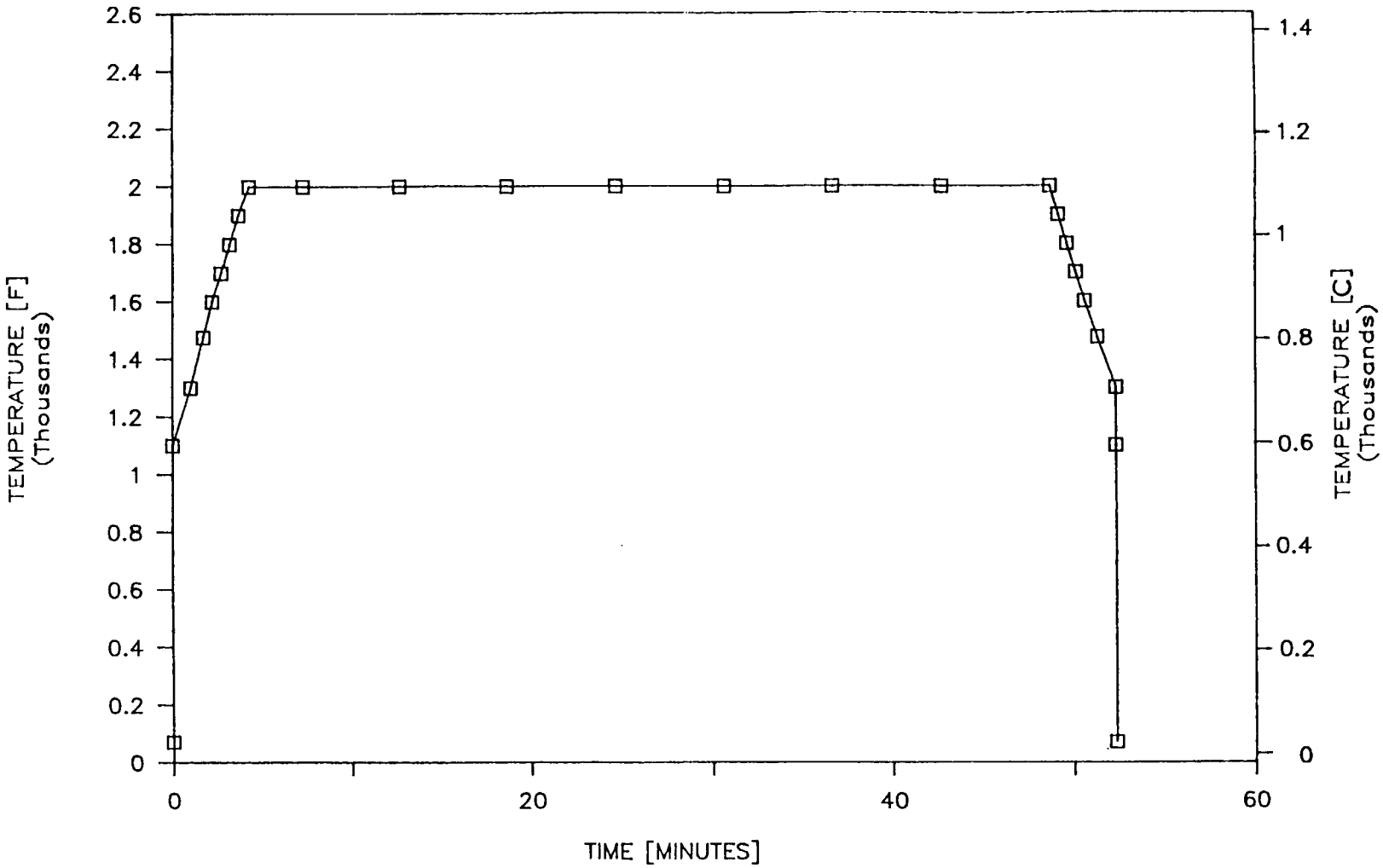

Figure 32. Thermal Loading Cycle.

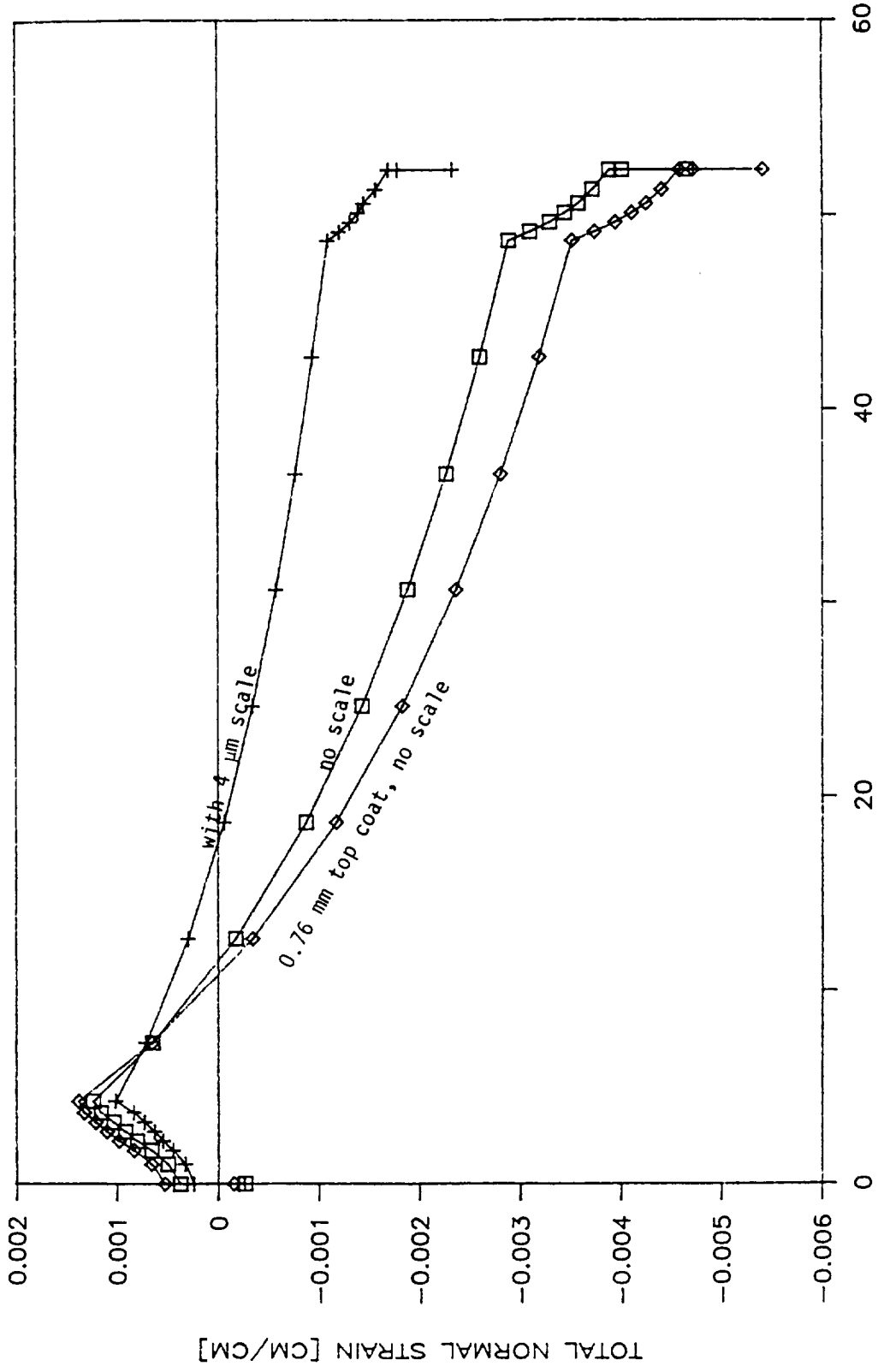

Figure 33. Calculated Total Normal Strain in Top Coat at Top Coat/Bond Coat Interface of Thermal Barrier Coated Tubular Specimen During Thermal Cycle Shown in Figure 32. Bond Coat Thickness 0.13 mm and Top Coat Thickness 0.254 mm Unless Indicated Otherwise.

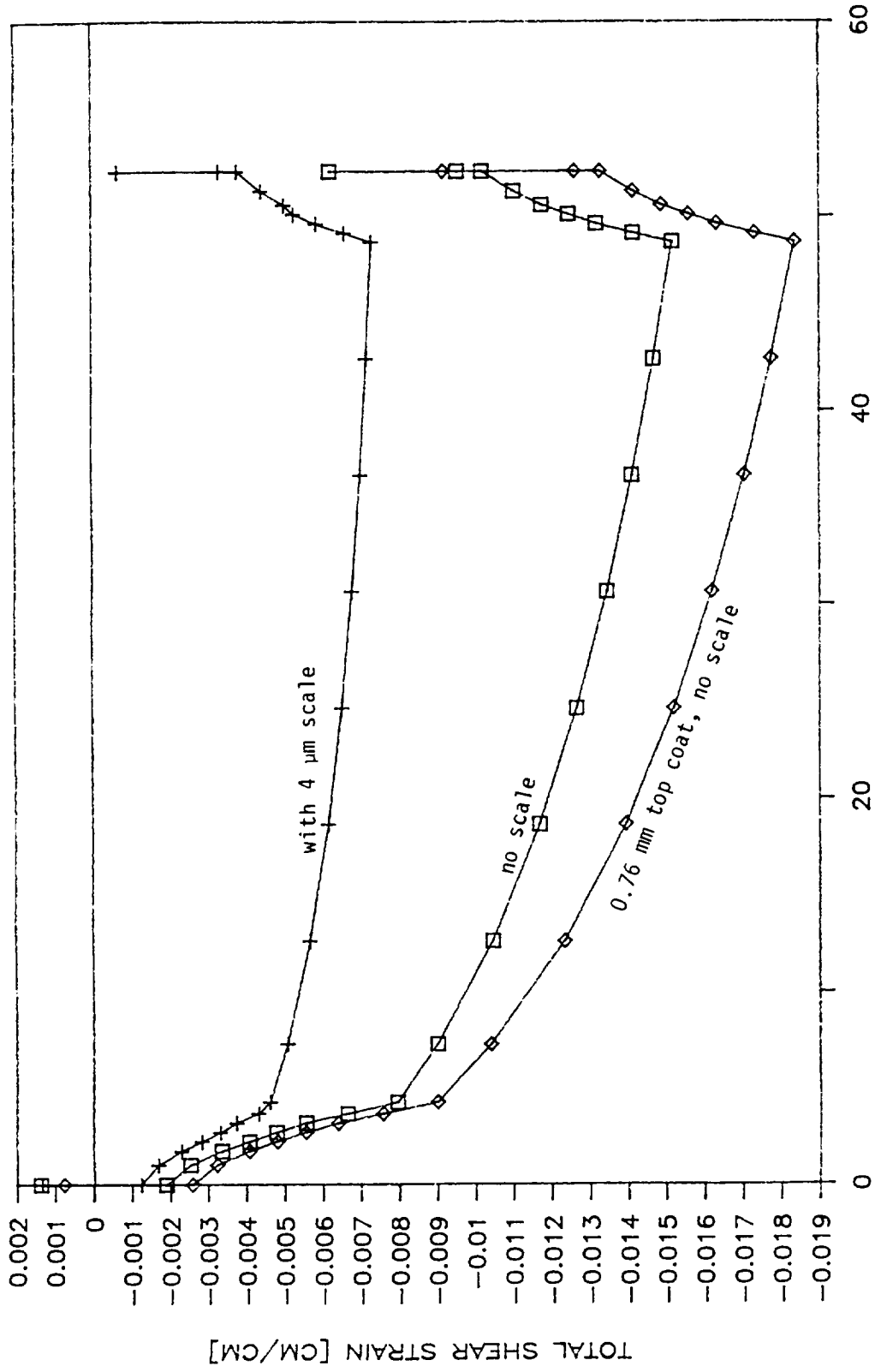

Figure 34. Calculated Total Shear Strain in Top Coat at Top Coat/Bond Coat Interface of Thermal Barrier Coated Tubular Specimen During Thermal Cycle Shown in Figure 32. Bond Coat Thickness 0.13 mm and Top Coat Thickness 0.254 mm Unless Indicated Otherwise.

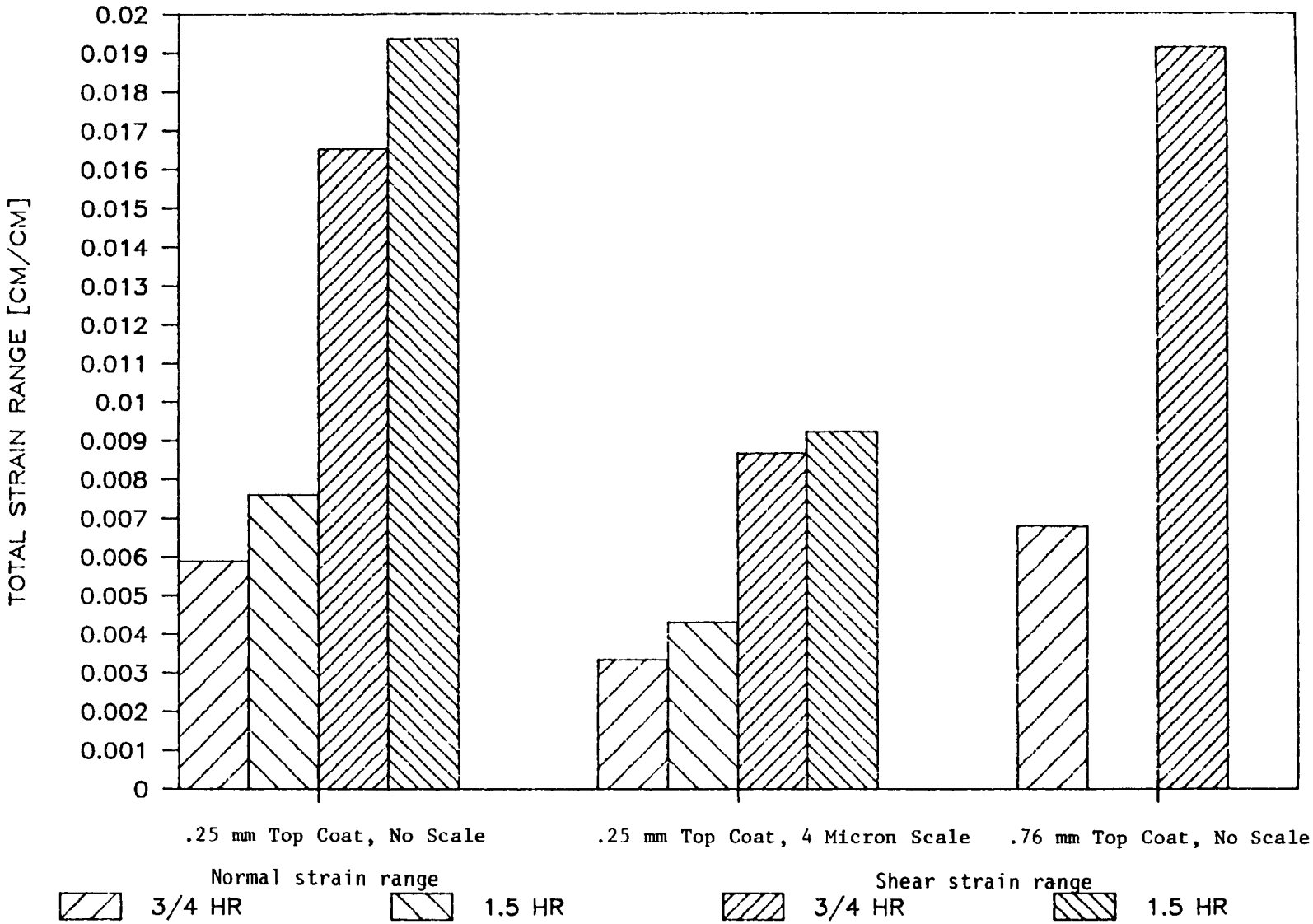

Figure 35. Effect of Length of Dwell Period at 1093°C During Thermal Cycle on the Total Strain Range in the Top Coat at Top Coat/Bond Coat Interface of Thermal Barrier Coated Tubular Specimen. Bond Coat Thickness 0.13 mm.

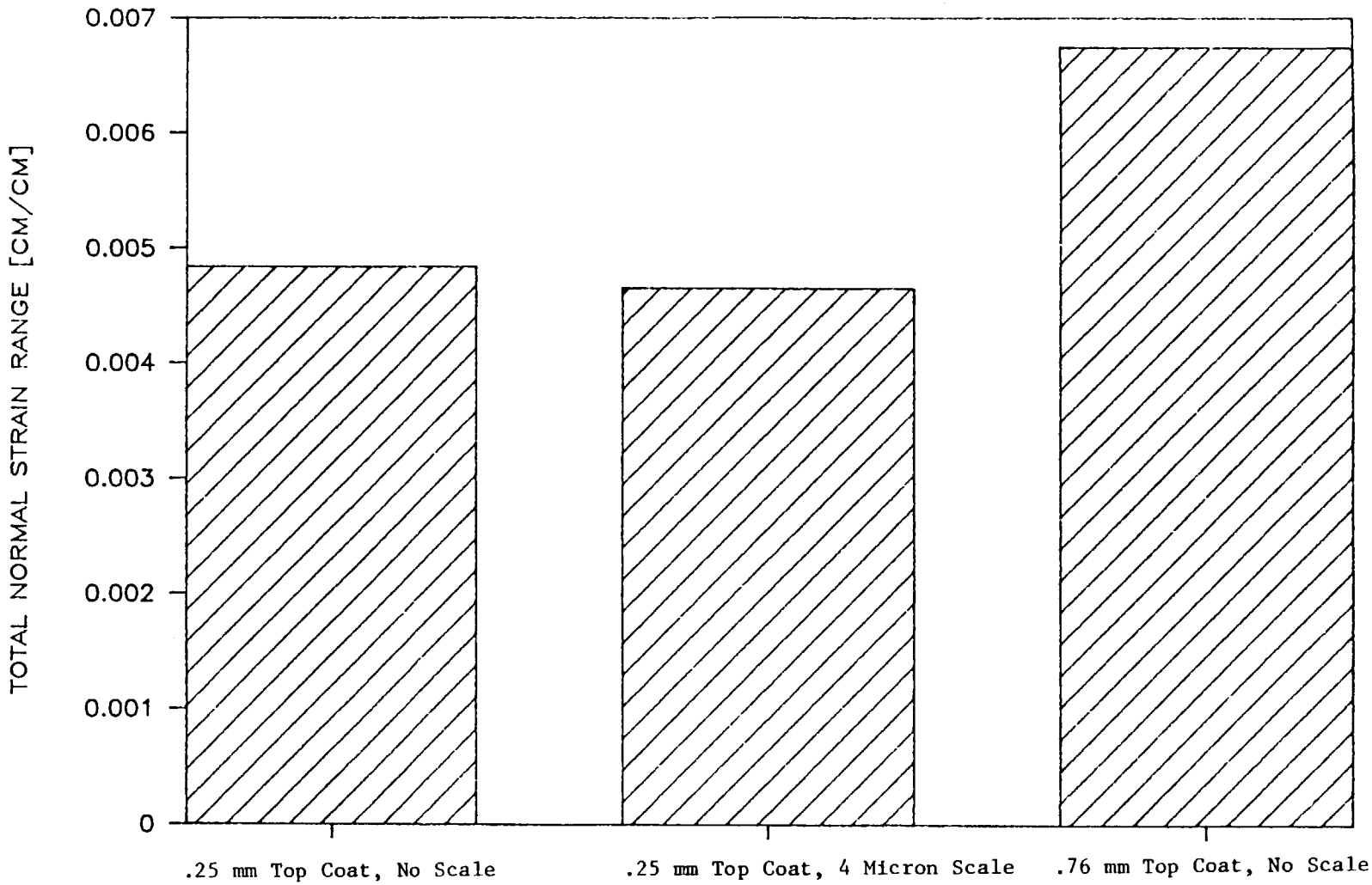

Figure 36. Effect of Al_2O_3 Scale and Top Coat Thickness on Total Normal Strain Range in the Top Coat at Top Coat/Bond Coat Interface Away from the Edge of Thermal Barrier Coated Tubular Specimen. Bond Coat Thickness 0.13 mm.

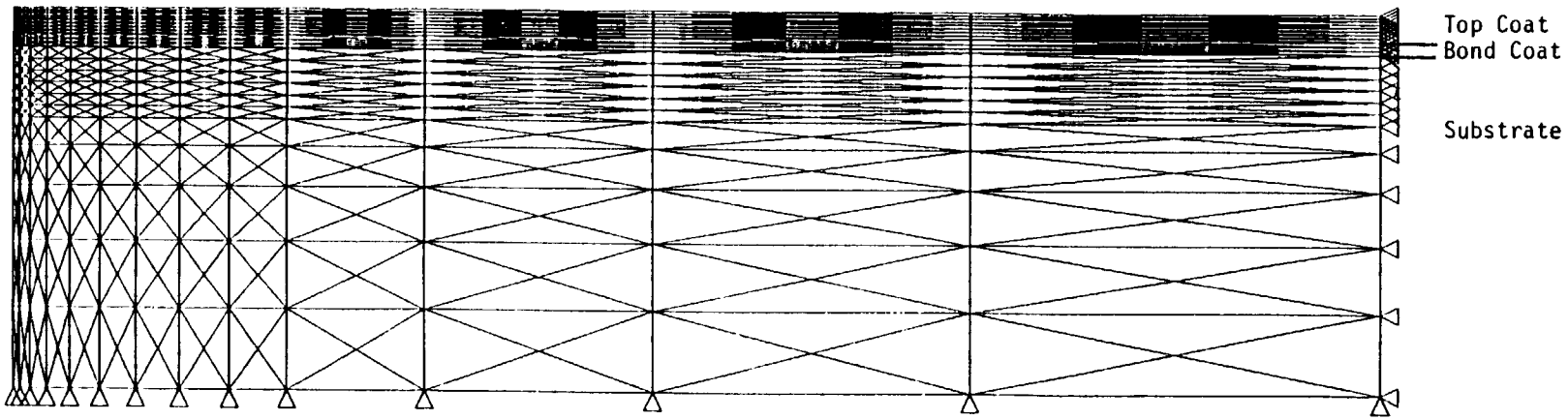

Figure 37. Finite Element Mesh of Thermal Barrier Coated Button Specimen.

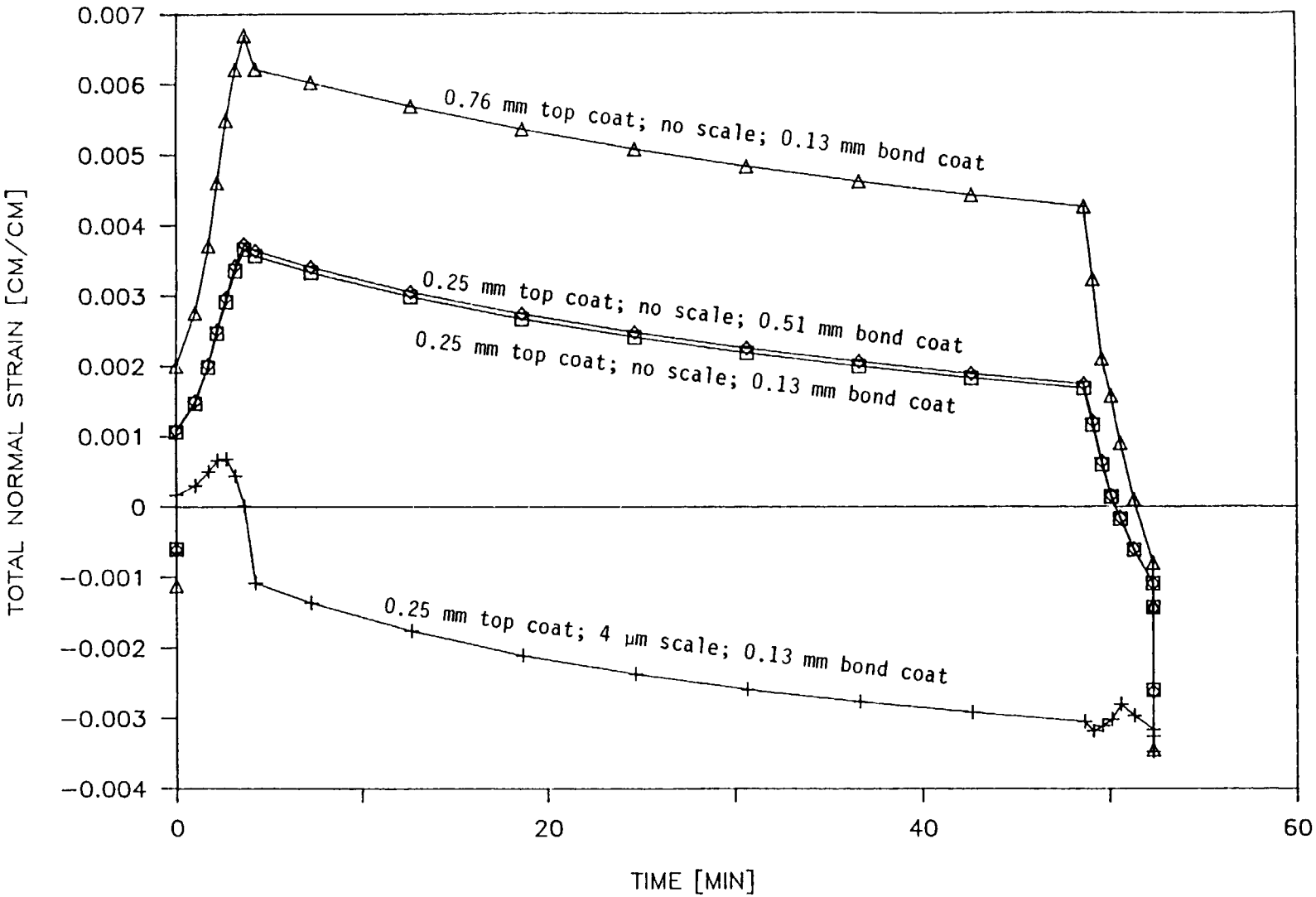

Figure 38. Calculated Total Normal Strain in Top Coat at Top Coat/Bond Coat Interface of Thermal Barrier Coated Button Specimen During Thermal Cycle Shown in Figure 32.

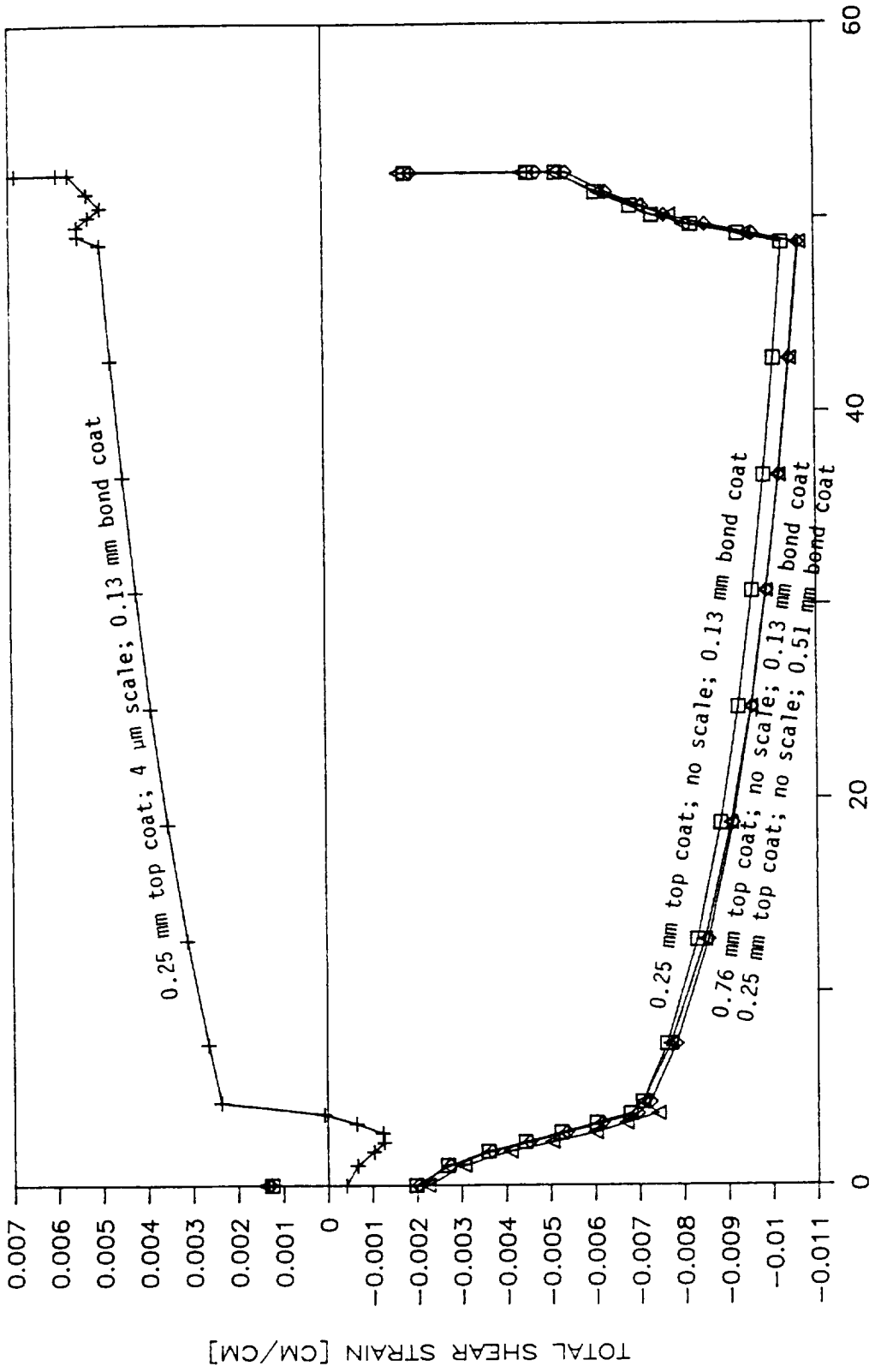

Figure 39. Calculated Total Shear Strain in Top Coat at Top Coat/Bond Coat Interface of Thermal Barrier Coated Button Specimen During Thermal Cycle Shown in Figure 32.

Also apparent in Figures 33 and 34 is the increase in strain range caused by a thicker top coat. This effect is even more pronounced when there is no chamfer at the top coat edge as in the button specimens. This is due to the increased stiffness of the thicker top coat, allowing it to better resist the outward pressure of the greater expanding bond coat and substrate.

In order to determine the difference an increase in hold time might make and to assess the amount of creep saturation obtained in one cycle, the 0.25 mm (0.01 inch) thick top coat models with and without the oxide scale were run with the hold time at 1093°C doubled (i.e., 1.5 hours instead of 0.75 hour). A comparison of total strain ranges can be seen in Figure 35, which shows that most of the creep occurs fairly quickly since there is a relatively small change in strain range for a doubling of hold time.

It is interesting to note that away from the edge, the strain state is less severe, especially for shear strain which is almost nonexistent. The presence of scale does not reduce the strains as at the edge, but neither does it seem to increase the strain. A comparison of strain ranges for an element located on the bond coat/top coat interface away from an edge is shown in Figure 36.

The button geometry was modeled with axisymmetric elements using the mesh shown in Figure 37. The mesh was again tailored such that greater sensitivity would be obtained in the areas of interest. The analyses were similar to those used for the tubes. Additionally, a change in the bond coat thickness was run to see what effect this would have.

The results are shown in Figures 38 and 39. More figures are shown in Appendix F. It can be seen that the scale again has the effect of reducing the stress/strain ranges. The top coat thickness effect is much more dramatic in the normal direction due to the fact that the edge is not chamfered as in the case of the tube. The thickness has little effect on shear strain, however. Changing the bond coat thickness can be seen to have essentially no effect on the top coat.

In summary, the trends obtained through a two-dimensional, axisymmetric finite element analysis with cyclic loading and material nonlinearities revealed that creep is the major material nonlinearity mechanism acting, rather than plasticity. As the stiffness of the top coat increases with thickness, the top coat is more severely loaded. Changing the bond coat thickness appears to have little effect on the top coat since the top coat is stress free when applied to the bond coat. The presence of a thin oxide scale can be beneficial due to the similarity in thermal expansion properties between scale and top coat. Clearly, however, continued growth of an oxide scale at the top coat/bond coat interface would ultimately not be beneficial and result in failure of the TBC as has been described earlier.

4.2 Thermomechanical Experiments

In order to better define the specimen response under the conditions of the furnace cycle test, an analogous experiment was conducted in the low cycle fatigue laboratory. The goal of these tests was to control and measure the temperature, load, and deformation of the specimen

using an electro-hydraulic test machine with induction heating of the specimen. The specimen, a standard thermomechanical fatigue (TMF) specimen (Figure 40), is a hollow cylindrical tube with threaded ends. Specimens were coated so that the bond and top coats covered the entire gage section and extended into the shank area. Displacement of the specimen gage length was measured by a conventional high temperature extensometer with its tips placed on the coating surface. A high frequency Lepel induction heater was used to heat the specimen. This heating technique produces a different through-the-thickness temperature gradient than was produced by the furnace, but this discrepancy was unavoidable for this phase of the test program. A strap-on thermocouple was used to control the temperature.

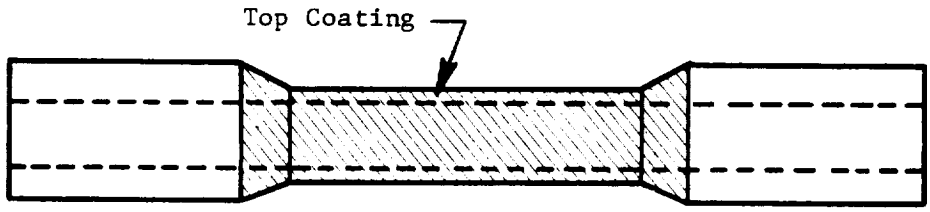

Figure 40. Thermomechanical Fatigue Test Specimen.

Before running the actual displacement experiments, grooves were machined in one specimen to allow placement of five thermocouples beneath the bond and top coats. The thermocouples and lead wires were placed in these grooves and the coatings applied over them. One thermocouple was at the center of the specimen with two more on either side of center as sketched in Figure 41; the five thermocouples were spaced 6.4 mm apart. Figure 42 shows the temperature profile developed by the center three thermocouples. From this data and from the output of the control thermocouple which was strapped to the outer surface of the coating, a temperature profile for the outer surface of the ceramic was developed and monitored. Note in Figure 42 that the cooling leg is longer than the heating leg; this was necessitated by the specimen geometry requiring a longer time to maintain a linear cooling rate. Note also that the temperature does not reach the lowest temperature achieved in the furnace cycle test. A temperature less than 121°C (250°F) would have required the use of cooling air through the hollow tube; the radial temperature gradients this would produce were deemed undesirable for this particular experiment.

The intent of the first experiment was to obtain quantitative data on the displacement of the specimen as it underwent the hold time cycle imposed in the furnace. For one of the tests, a narrow strip of coating was removed to allow measurement of substrate displacement. A second extensometer was placed with its tips in this strip. The strip was positioned approximately 120° away from the extensometer with its tips on the coating surface.

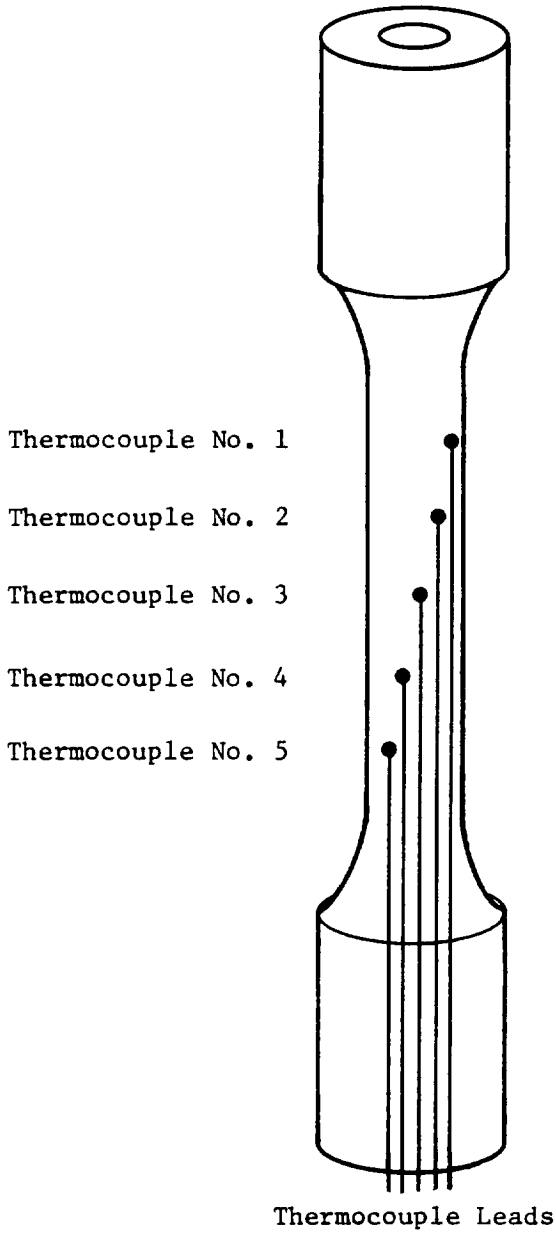

Figure 41. Locations of Embedded Thermocouples in Thermomechanical Test Specimens.

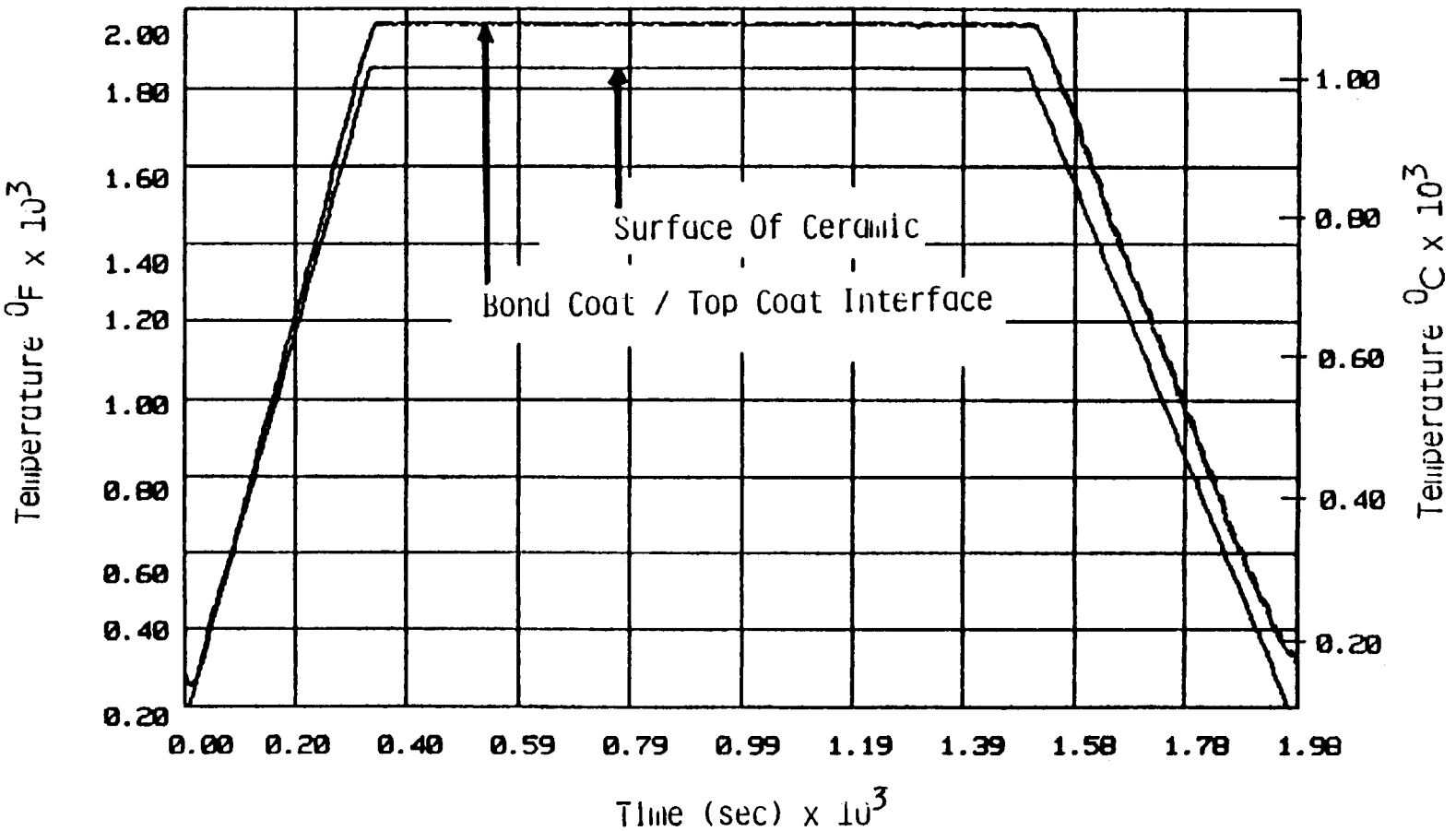

Figure 42. Temperature Profiles (Thermomechanical Experiment Thermal Cycle) for Thermocouples Embedded at Bond/Coat Top Coat Interface and at the Surface of the Ceramic.

The test was run while maintaining zero mechanical load, and the deformation sensed by the two extensometers was recorded on a strip chart. The chart showed time-dependent deformation in the substrate but very little happened in the coating, although it appeared that there was a very small increase in coating strain. It was hoped that this experiment would show a phase relationship between the deformation of the coating and substrate. Unfortunately the digital data acquisition did not work properly, forcing reliance on the strip chart. An examination of the strip chart indicates that the coating has a shorter ramp than the René 80 during heat-up, but during cool down the reverse is true. Both observations seem consistent over the test, but it seems likely that the shift is caused by a delay in the coating response at the cool-to-heat transition. That is, the shift in deformation is due to faster thermal response of the René 80 rather than a difference in creep response. A more accurate digital data acquisition system would be required to confirm this point. The free thermal expansion of the specimen gage section was in good agreement with the predicted value obtained from the coefficient of thermal expansion and the temperature change.

With the thermal profile and specimen behavior determined, a coated tube specimen was thermally cycled to represent the furnace cycle test cycle. This specimen underwent 249 cycles with no sign of distress to the coating.

Since the pure thermal loading did not produce failure in the time frame in which the specimens had failed in the earlier furnace tests, a mechanical strain component was added to the thermal strain. It was originally intended to superimpose tensile and compressive loading on the coating to determine the effect of stress state on failure of the coating. However, this proved difficult because the very large thermal cycle imposed a sizable thermal expansion on the specimen. The expansion limited the test conditions achievable in the current program. In addition, the lack of data on the TMF testing meant that there were no guidelines for establishing appropriate test conditions.

The first TMF test was started with a mechanical strain range of -0.3 to -0.1% run in phase with the temperature. The total strain range extended from -0.05 to 1.5%, while the stress was almost entirely compressive. There was a small tensile stress at the beginning of the hold in the first cycle but it relaxed out of the material. This cycle was run for 205 cycles and then the minimum mechanical strain was decreased to -0.4% to increase the load. After 176 additional cycles, the minimum strain range was again decreased, this time to -0.5%. The total strain hysteresis loop for the latter cycle is shown in Figure 43. After an additional 59 cycles the René 80 specimen failed, but no cracking of the ceramic was noted before gross (specimen separation) failure.

The second test was started at the same mechanical strain as the first, but after two cycles the range was changed to -0.1 to 0.1%. Following 52 cycles, the range was moved to -0.05 to 0.15% in an effort to increase the tensile portion of the cycle and run for 371 more cycles. While the ceramic showed no visible damage, the large changes in load record indicated that the specimen was cracked. The test was halted and the specimen was monotonically pulled apart. Figure 44 shows the total strain hysteresis loop for the test.

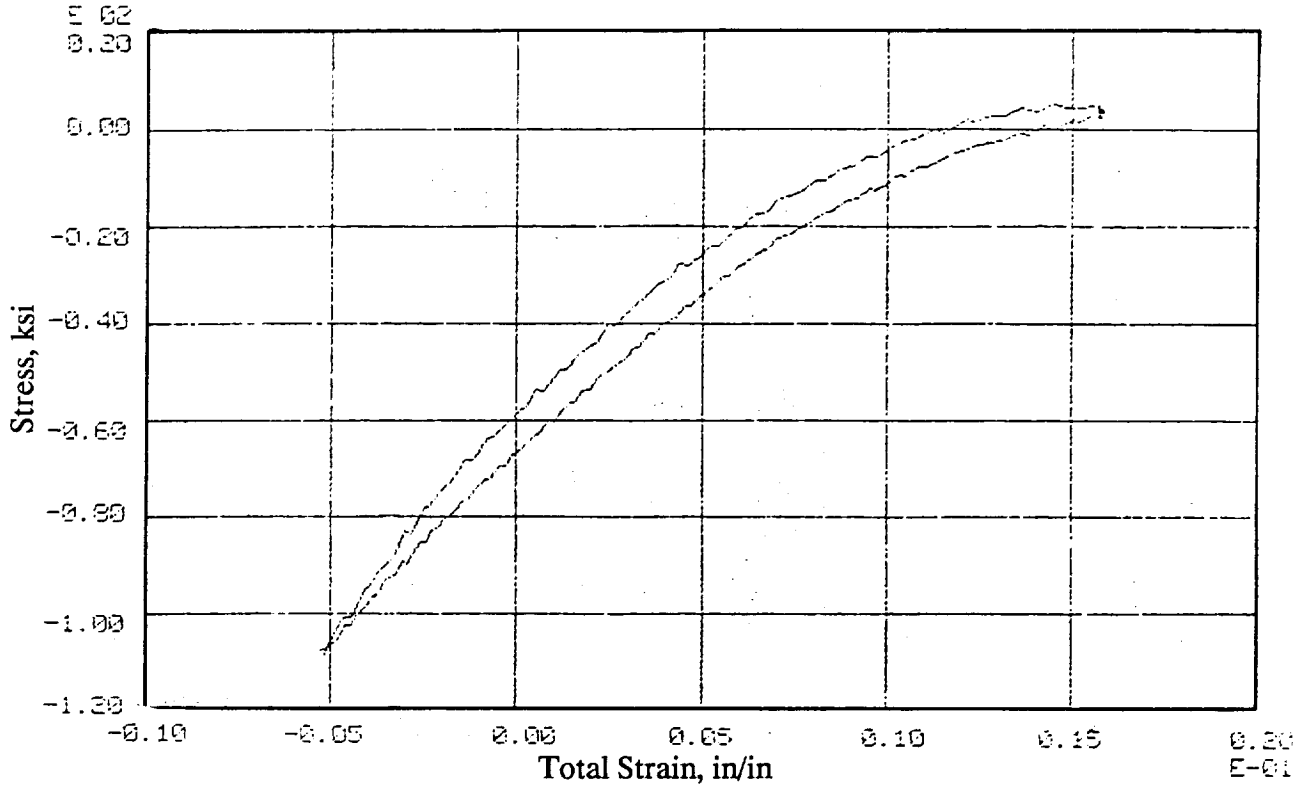

Figure 43. Stress-Strain Cycle During First TMF Test.

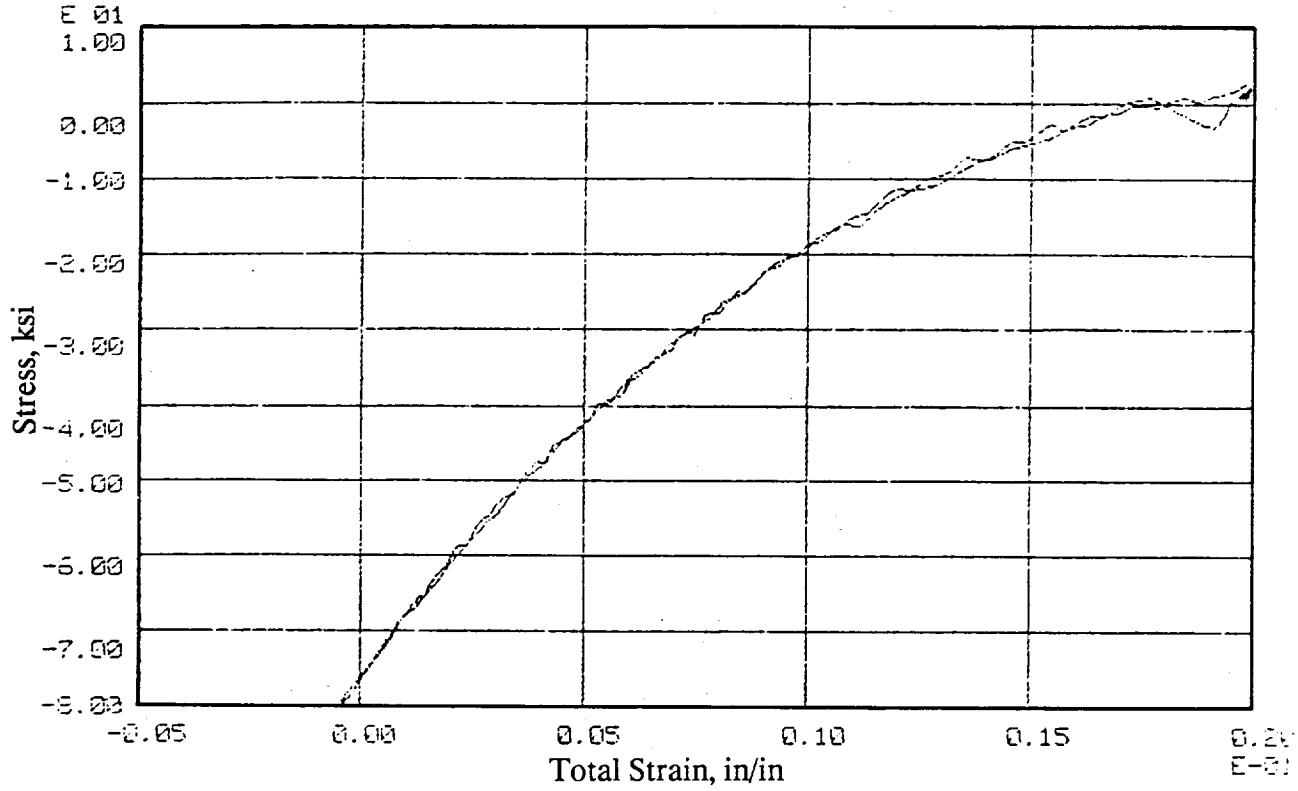

Figure 44. Stress-Strain Cycle During Second TMF Test.

The third thermomechanical test was intended to be run with a largely compressive strain range. However, the large thermal strain meant that a large compressive load would have to be applied or an out-of-phase cycle would be needed. To avoid buckling the specimen or introducing a new failure mode, it was decided to repeat the last strain range of the first test. With a mechanical strain range of -0.5 to +0.1%, this cycle at least gave a significant portion of the cycle in compression. The specimen lasted only 34 cycles before failing. There was no visible damage to the TBC before specimen separation occurred. The hysteresis loop in Figure 45 shows a large amount of inelastic deformation.

The fracture surfaces of the three TMF specimens were examined to determine the role of each of the materials in the failure process. A typical portion of the fracture surface of each specimen is shown in Figure 46. Specimens from the first and third tests show that fracture surface in the René 80 is dominated by interdendritic features. The fracture surface of the specimen from the second test, which failed monotonically, is quite different from the other two. The failure surface is more faceted, displaying the features of fast fracture. In none of the three specimens was it possible to locate any fatigue markings such as striations. For specimens from tests 1 and 3, Figures 46a and 46c, there were several large, relatively flat areas which at low magnification are reminiscent of elliptical fatigue cracks. These areas, however, when examined at high magnification, showed no striation markings, so it is speculation to interpret these planar features as fatigue cracks growing inward from the bond line. There was no evidence that the ceramic top coat played any role in the fatigue fracture; there were no fatigue markings or signs of an origin in the ceramic. Figure 47 shows a small section of the top coat of the specimen from the third TMF test. The fracture surface is very crystallographic and shows numerous secondary cracks. There are a number of lines on some facets but these lines are perpendicular to the direction of crack propagation and are more likely to be splat boundaries than fatigue striations. From the different heights of the fracture surface, it appears that the failure origin was in the René 80 or the bond coat and the ceramic fracture was a terminal event.

In addition to the failure surface, it is interesting to examine Figure 48, which shows a portion of the cylindrical surface of the same specimen. Clearly the surface is riddled with small cracks. There is a high crack density with no particular orientation effect; note that some of the cracks possess a significant crack opening. Since the pictures of the failed specimen were taken after the final fracture, one cannot say whether the cracks were caused by fatigue, the unstable fracture at the end of the test or were present from the manufacturing cycle. This point will be addressed later in this section.

In addition to the TMF tests on the cylindrical specimens, several isothermal bending tests were conducted. The objective of these tests was to examine the effect of mechanical strain on the life of the ceramic top coat. By removing the thermal strain component and by cycling at a fairly high rate, the strain-life relation could be quantified in a well-controlled experiment and the results applied to the more complex situation in which the temperature is changing. Moreover, it was hoped that the fast cycling frequency would allow the time and cycle dependent effects to be separated.

ORIGINAL PAGE IS
OF POOR QUALITY

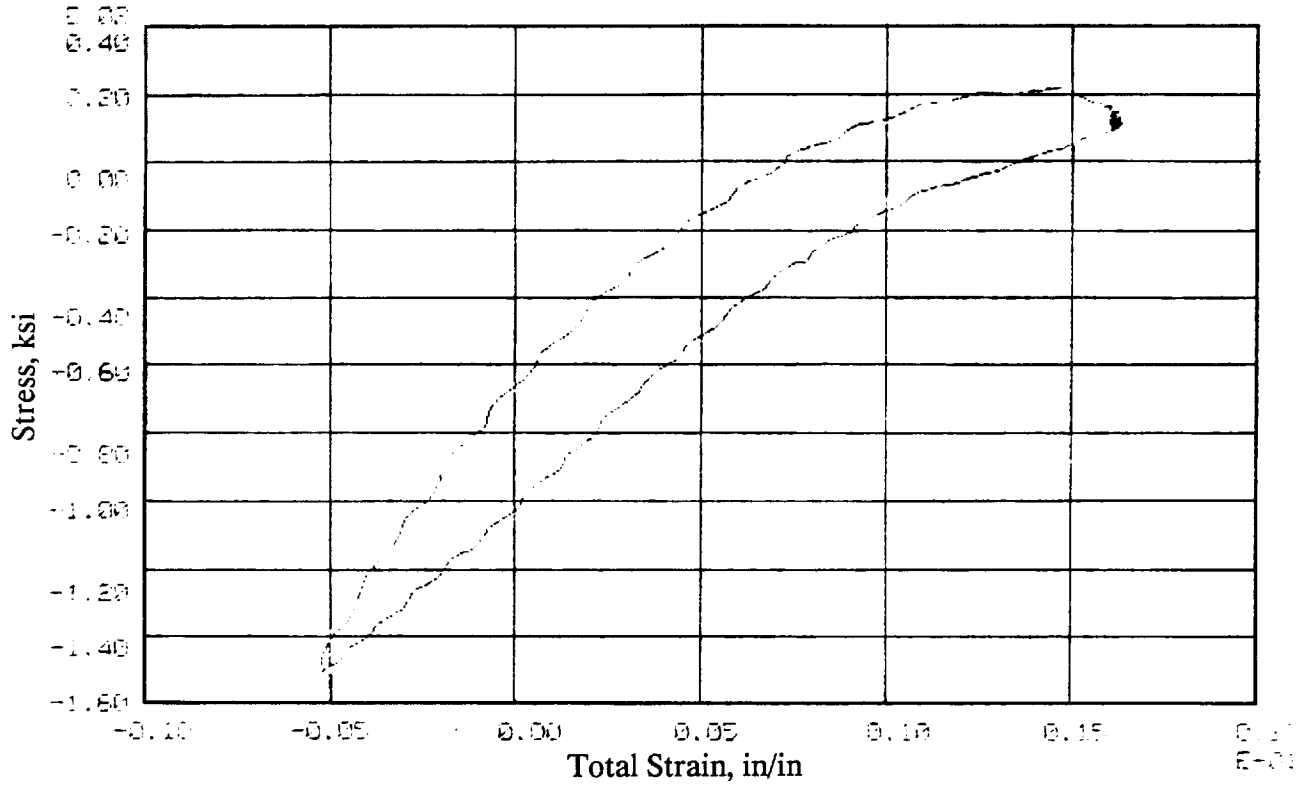

Figure 45. Stress-Strain Cycle During Third TMF Test.

a. Specimen from First TMF Test

b. Specimen from Second TMF Test

c. Specimen from Third TMF Test

Figure 46. Fracture Surface of Test Specimens from TMF Test.

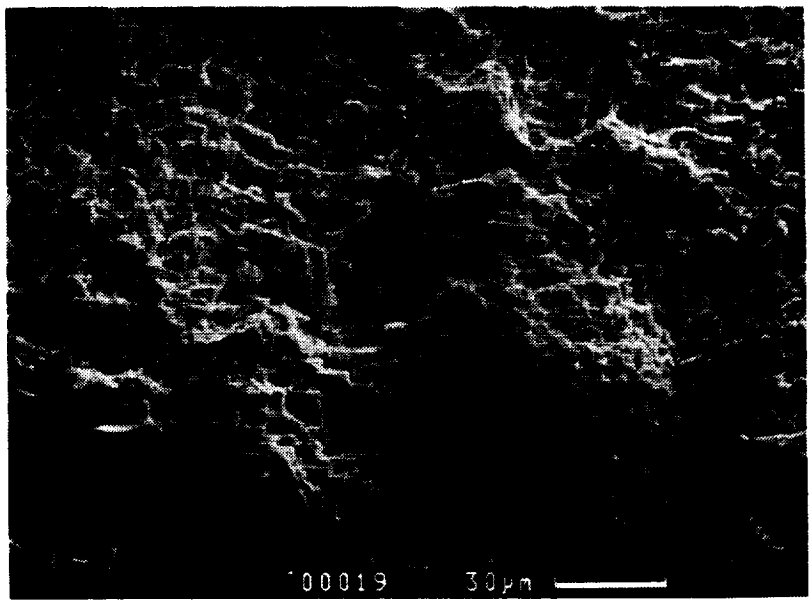

a

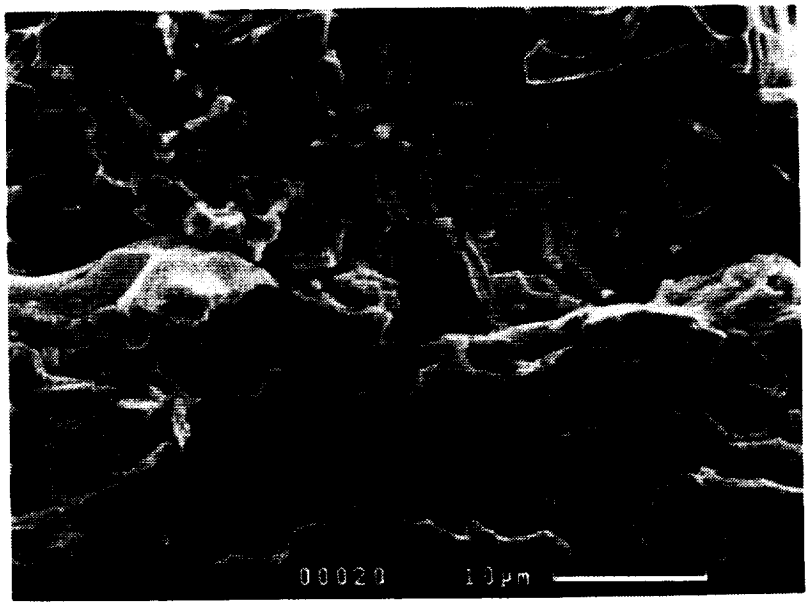

b

Figure 47 Fracture Surface of Zirconia Layer of TMF Specimen from Third TMF Test Showing Lack of Crack Striations.

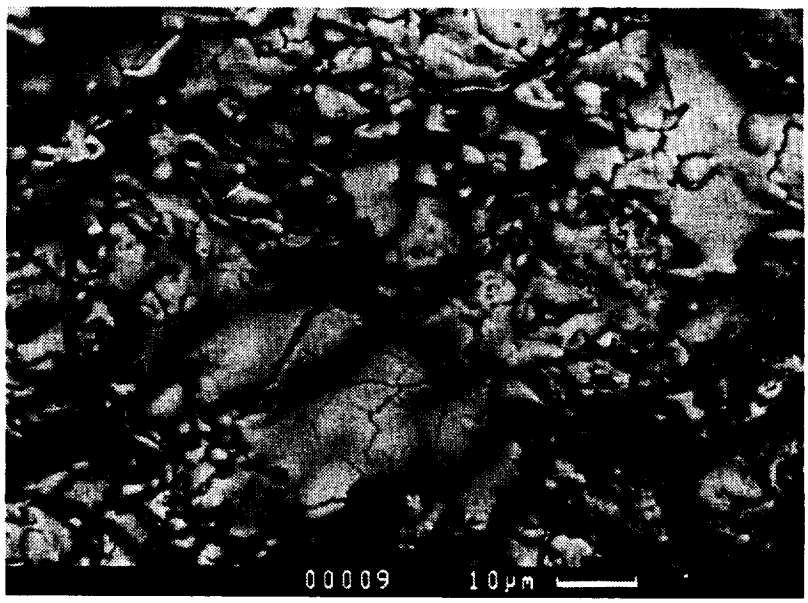

a

b

Figure 48 Surface of Zirconia Layer Showing Presence of Many Microcracks of Random Orientation.

The isothermal tests were conducted at 1093°C in a resistance furnace mounted in an electro-hydraulic test frame. The hot zone of this furnace was relatively small, therefore necessitating the use of a three-point bend specimen. A four-point bend fixture requires much more massive loading grips and would be more difficult to fit into the furnace. The larger four-point fixture is also potentially more difficult to control, a particularly important point in view of the very small loads involved in these tests. It was estimated that a deflection of 25 μm would be large enough to cause failure of the TBC. Accurately maintaining and controlling such small deflections was a concern but with some effort, it proved possible to successfully carry out the experiments.

In conformance with the other testing, René 80 was used as a base metal. Small René 80 blanks, 38.1 x 19.1 x 1.3 mm, were sprayed with the bond and top coat on both faces. The TBC was removed by grit blasting from a 6 mm-wide strip at each end of one side of the specimen and from a 2-mm-wide strip at the center on the opposite side where the loading pins make contact with the specimen.

The specimens were placed in the furnace and brought to 1093°C and allowed to stabilize for 1 to 2 hours. Cycling was carried out in deflection control at 1 Hertz; a very small minimum deflection was used to prevent complete unloading. The test was halted periodically and the ceramic examined with a microscope; this procedure was time consuming but avoided an elaborate noncontacting approach to crack detection.

The first two tests were devoted to determining suitable test parameters. For example, the first specimen was run for 200 cycles at a maximum deflection of 0.025 mm; the test was halted and the specimen inspected. No cracks were noted and both the maximum deflection and cycling interval were increased as experience was gained. Eventually a cyclic deflection of 0.150 mm was maintained for 15,000 cycles with no cracking visible. The presence of the mean deflection caused the thin René 80 substrate to creep; this in turn necessitated an increase in the mean deflection to prevent complete unloading at minimum deflection. In all cases, TBC failure was produced after quite extensive deflection of the specimen.

In the third test, the specimen was cycled for 30,000 cycles from 0 to 0.1 mm. The range was kept constant but the minimum was raised to 0.05 mm for another 15,000 cycles, at which time the specimen was still flat. When the minimum was raised to 0.1 mm, the specimen took on a permanent set after 15,000 additional cycles. Two more increases in load and another 30,000 cycles left a deflection of 0.60 mm in the specimen and a crack in the TBC at the center on the convex (tension) side. Figure 49 shows an overall view of the crack while Figure 50 portrays an enlarged view of an area near the center of the crack. All of the other specimens failed at the center and were similar in appearance to this specimen. There were no indications of fracture on the compression side of the bend specimen or near the ends of coating-bond coat interface.

In addition to the study of the cracks previously shown, both virgin ceramic surfaces and other areas of the bend and tube specimens were examined. The bend specimens were

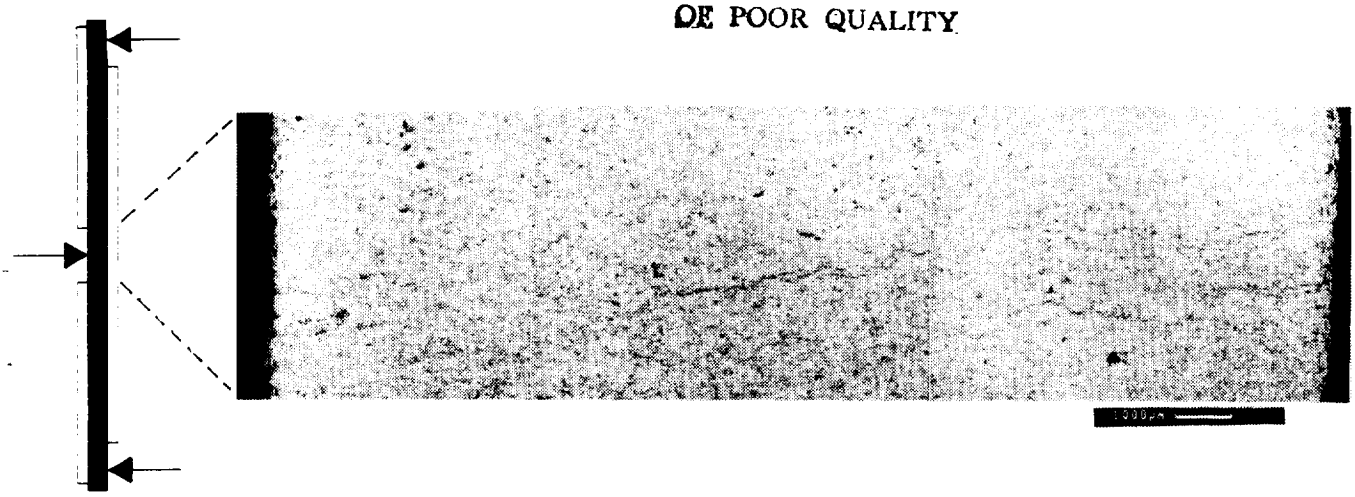

Figure 49. Surface of TBC at Center of Bend Specimen on Convex (Tension) Side Showing Cracks in Surface of Zirconia.

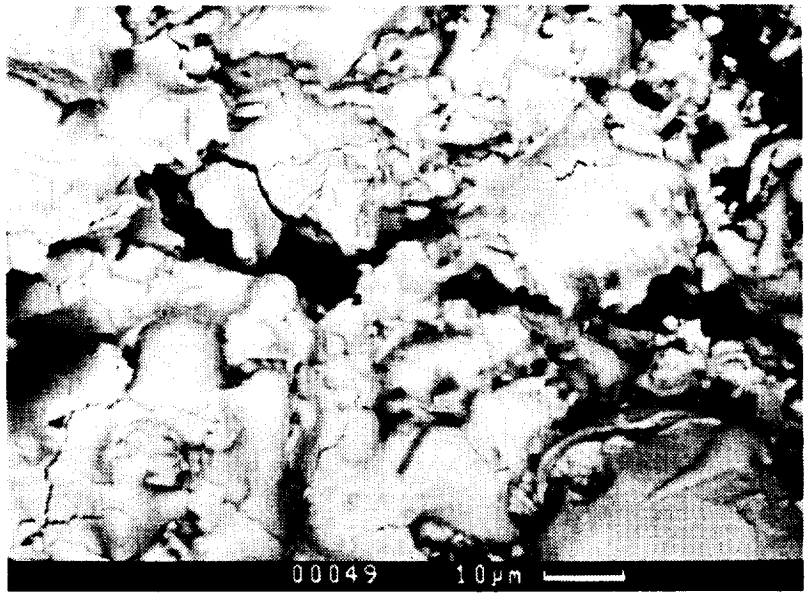

Figure 50. Enlarged Area of Surface of Specimen Shown in Figure 49.

scanned at locations away from the cracks. These locations were closer to the support pins and so were subject to much lower loads than the cracked area of Figure 49. Figures 51 and 52 show areas about half way between the crack and the support and close to the support, respectively. Both photographs show that the ceramic is full of microcracks, as does Figure 53 which displays the surface of the tube near the end of the gage section. There does not appear to be any particular orientation effect associated with the cracking. There does seem to be a slightly higher crack density at the higher strain location but given the density of microcracking, this is probably not highly significant.

For comparison purposes, Figure 54 and 55 show the virgin surface of both a tube and a bend specimen. In both cases, there is a significant amount of cracking with no particular orientation dominance. It appears that the tube may have a larger number of cracks but this is probably due to the larger "mud flat" area on the tube making the cracks more visible. Since only a very limited area of the specimen was examined, some caution should be exercised as to the generality of the observation.

When Figures 54 and 55 are compared to Figures 48 and 51 through 53, it is clear that the tested specimens do contain a greater density of microcracks than the virgin specimens. It is also clear, however, that the specimens do contain a significant amount of surface cracking at the end of the manufacturing cycle. Without sectioning, it cannot be ascertained as to the depth of the cracks and whether or not any subsurface cracks exist. This information needs to be supplemented with monitoring of individual cracks and their interaction as they grow. Such data will be difficult to acquire but is needed to support a mechanistic picture of the failure process.

The fatigue experiments in this section may be summarized as follows:

- There is significant microcracking in the TBC at the conclusion of the manufacturing cycle. The role, if any, of these microcracks in the final failure remains to be defined.
- In neither the tube nor the bend specimen was TBC failure observed without large substrate straining. The top coat appears to be stronger and more fatigue resistant than previously thought.
- The TMF specimens, in contrast to the thermal specimens, did not have coating edges in the gage section. Calculations show that the most severely strained coating elements are located at coating edges.
- There was no evidence of crack growth in the ceramic when the fracture surfaces of the TMF tubes were examined.

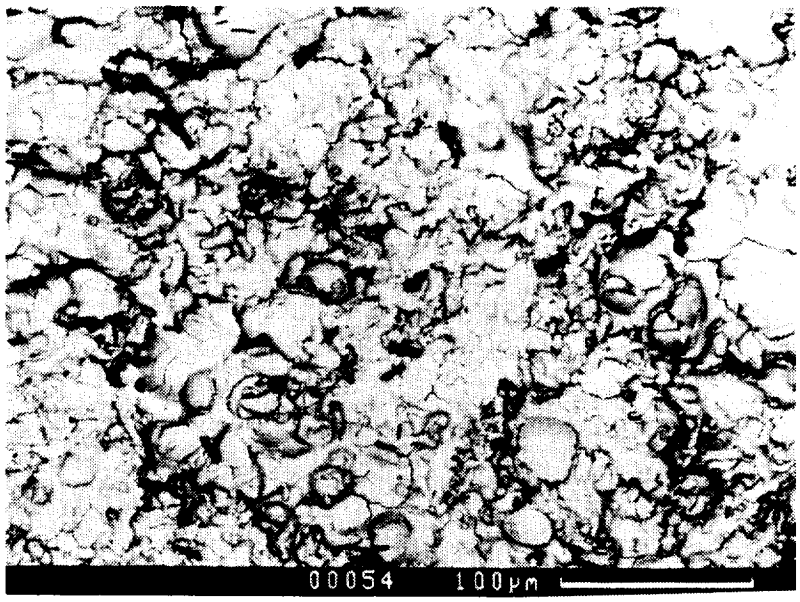

Figure 51. Enlarged View of Surface of Specimen Shown in Figure 49 Approximately Midway Between Center and the Support.

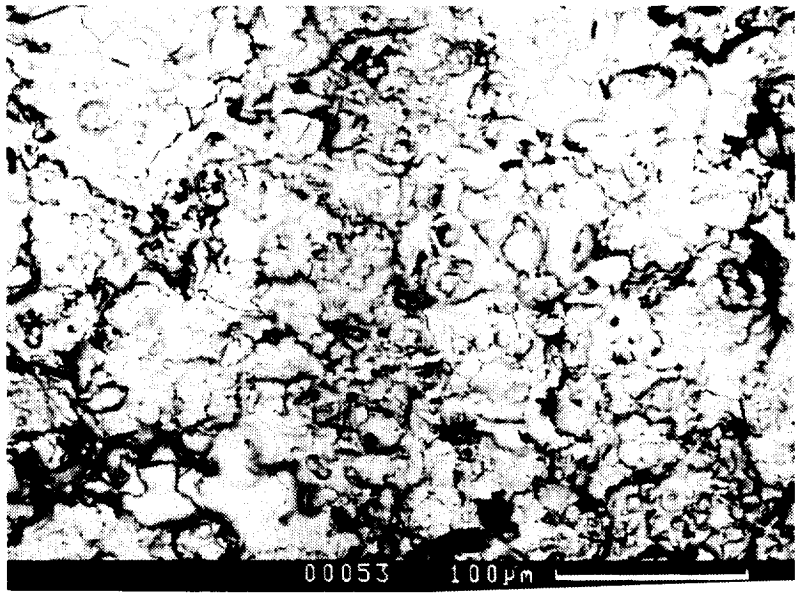

Figure 52. Enlarged View of Surface of Specimen Shown in Figure 49 Near End of Specimen.

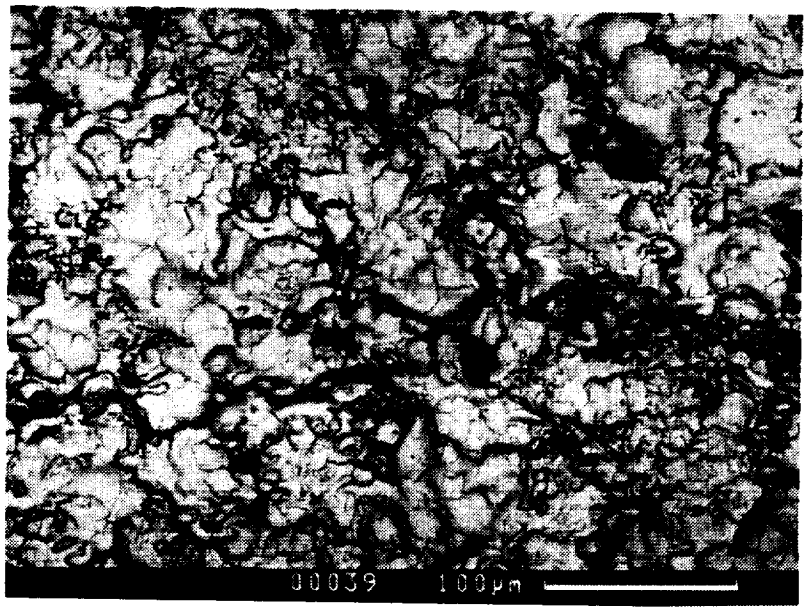

Figure 53. Surface of Coating on Tested Tubular TMF Specimen Near End of Gage Section, Showing Presence of Cracks.

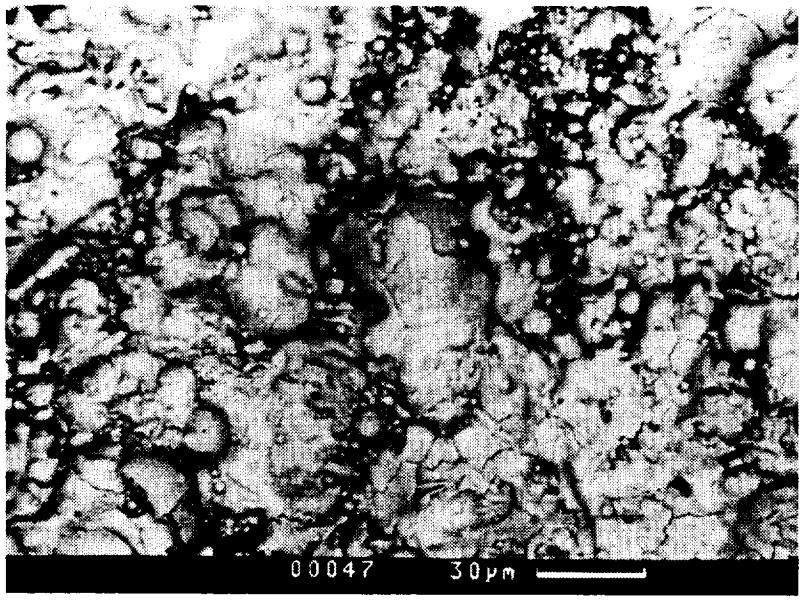

Figure 54. Surface of Coating on Untested Tubular TMF Specimen Showing Presence of Cracks of Random Orientation.

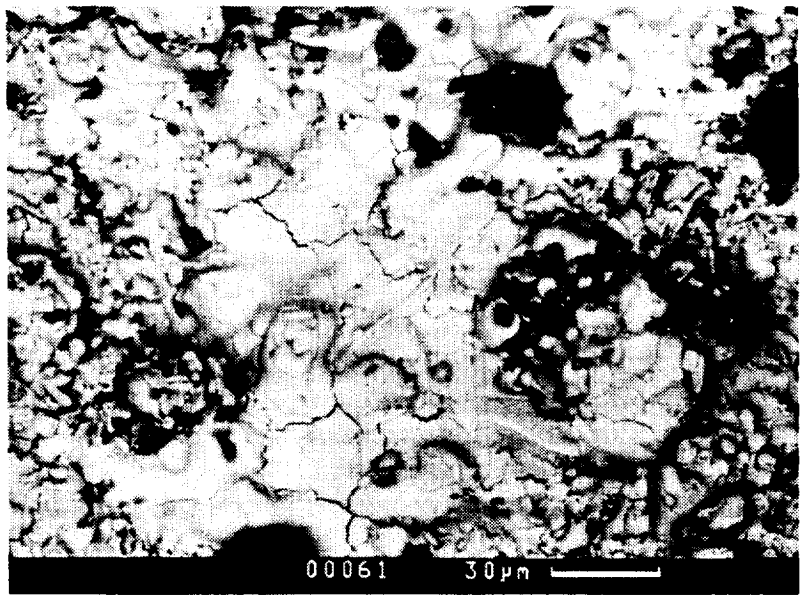

Figure 55. Surface of Coating on Untested Bend Specimen Showing Presence of Cracks of Random Orientation.

4.3 TBC Failure Model

4.3.1 Development of Life Prediction Model

The objective of the analytical modeling program was to produce an initial life prediction model and to define the direction that future modeling efforts should take. The spallation process likely includes several steps: initiation of microcracks, growth and link-up of these microcracks, and finally coating loss. Major contributors to the stresses which cause these events include thermal expansion mismatch, oxide scale growth on the bond coat, and material and structural changes which occur during elevated temperature use.

However, all of the above noted components of the failure process are subsurface and thus not accessible to direct observation. All the quantitative data available is post-failure. This is in direct contrast to the failure process of homogeneous materials in which their major failure modes consist of observable surface processes. Hence, we do not have the ability, as in homogeneous materials, to obtain experimental measurements at the location of failure. This, then, required the use of a technique to develop a life prediction model for TBCs different from that used for conventional materials.

The technique used in this study is that of inference. Since the effects that cause failure cannot be measured directly, it is necessary to correlate effects that can be measured to those at the failure location. To perform this correlation, use was made of nonlinear finite element analysis of the test specimens. To build a high degree of confidence into this technique, a range of test/geometry conditions was tested and modeled. Confidence in the inference technique comes from the ability to correlate TBC failures to the range of mapped conditions.

In attempting to develop the life models, the task was to understand the stress/strain/displacement fields developed at the TBC failure location during the thermal fatigue tests. In particular the role of the time dependent material properties and the changes they cause in the strain field must be understood. Since the state of stress/strain can strongly influence the failure mechanism, the degree of multiaxiality at the failure location must be taken into consideration.

To counter the above difficulties, there is one major simplifying factor: the failure location. Post failure metallographic analyses of TBCs show that there is a consistent failure location a short distance into the top coat from the top coat/bond coat interface. Therefore, it is known which information from the nonlinear finite element analysis must be correlated with test data: those predictions which correspond to this location. It is also known from prior testing that if an edge exists in the test geometry, failure will initiate at the edge, near the top coat/bond coat interface.

This then defines the inference process. Nonlinear finite element models are generated for the various test geometries and run through a simulation of the test conditions. By interrogating the analytical predictions for the failure locations and evaluating them against test

results, it was found that a traditional LCF parameter was capable of correlation to the life of the TBCs studied. Figure 56 depicts this process and plots the cycles to failure versus equivalent dwell periods during pre-exposure and thermal cycling for the specimens tested in the furnace cycle tests. (The original data is shown in Figures 7 and 15). The thermal cycles involve 45 minute holds at maximum temperature and the time at temperature during the pre-exposures were converted to an equivalent number of 45 minute dwells. When these data are plotted against cycles to failure, the life separates into three sets. Fitting a power law to these data, it is seen that the argon pre-exposure was most damaging, followed by oxygen and the combined oxygen-argon. This, as well as data from Figure 14, suggests that time dependent deformation rather than oxidation per se is the primary damage mode. Nevertheless, oxidation clearly plays some part and is included in the general form of the damage model,

$$A N_f = f_1 (N, Z) + f_2 (N, H_e) \qquad (4\text{-}2)$$

where

N is the number of cycles and describes the cycle dependent damage,

Z represents the thickness of the oxide layer,

H_e is the time dependent damage expressed through the equivalent hold times.

The development of the oxide layer is easily described by periodically measuring its thickness during pre-exposure. The results of these measurements are shown in Figure 8. Since it appears that the oxide layer saturates at approximately 4 μm, the growth relation was taken in the power law form,

$$Z = 0.92t^{0.26} \qquad (4\text{-}3)$$

where t is the time in hours, and Z is in microns.

The oxide layer growth pattern is easily monitored but relating the time and cycle dependent damage to the cycles to failure is a much more difficult task. The correlation could be determined using a laboratory experimental approach but this would require a very sizable program to identify and differentiate the parameters. It was decided, therefore, to employ a computational approach and use finite element analysis to determine the damage parameters.

The details of the finite element analysis and parametric results are discussed in Section 4.1; the application of these results to the failure model will be covered here. There are two questions regarding the failure model which need to be answered. First, does the analysis predict stress and strain fields which are consistent with the fracture modes and locations observed in the experiments? Second, what specific parameter, or parameters, can be used to correlate these results? The answer to the first question is affirmative since the analysis predicts higher stresses near the edges of the ceramic top coat, the area in which failure is usually observed.

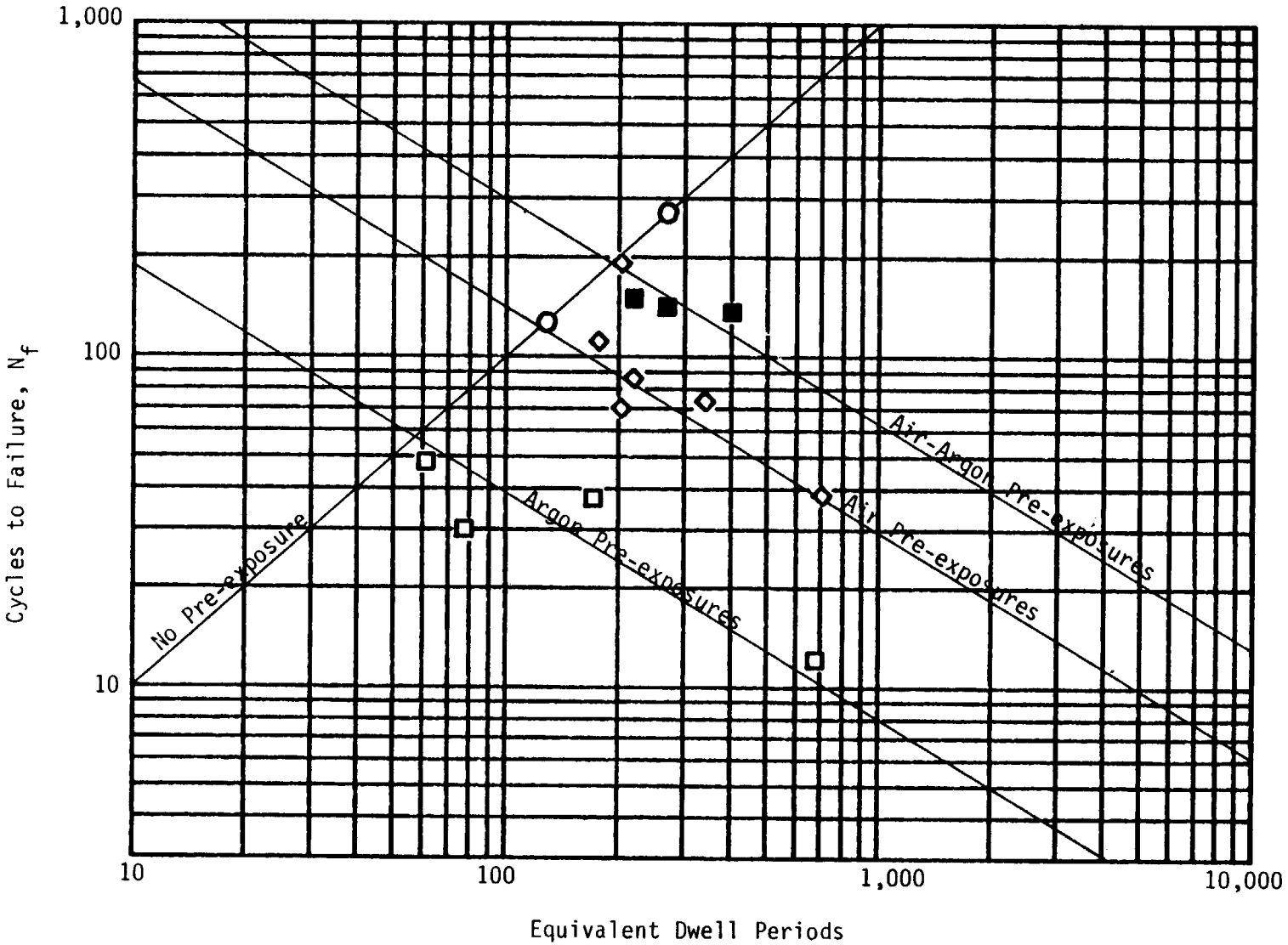

Figure 56. Cycles to Failure in Furnace Cycle Test Versus Equivalent Dwell Periods (Cycles Plus Pre-Exposure Time/0.75) for Thermal Barrier Coated Tubular Specimens.

The determination of a parameter capable of correlating the lives of the thermal barrier coated specimens is a difficult task since the failure mechanism is largely undetermined. In seeking a parameter, two considerations are that the deformation field is shear, driven by the thermal mismatch of the layers and that the field is multiaxial. The multiaxiality makes the failure mode geometry dependent and means that generalization of the failure model to mechanisms not observed in these experiments may be difficult.

The fact that there is a large shear gradient across the bond coat-top coat interface means that the shear strain will likely play a key role in the cracking process. A hysteretic energy based on shear strain was considered, but for the current experiments the high temperature hold will allow any stress existing during the hold period to relax. Thus, although energy has been used successfully to correlate TMF of René 80, it was decided to use the strain components themselves in this instance. Another factor in this decision was the success of the strain ranges in correlating life in multiaxial strain fields. Depending on the operative failure mechanism, both the normal and shear strain have been found to be important. A number of different models were tried with the general form being

$$N_f = f(\Delta\varepsilon_{rz}, \Delta_{rr}) \tag{4-4}$$

These models explicitly include the time and cycle dependent behavior through the constitutive model. One approach to the pre-exposure/oxidation influence would be to treat the growth of the oxide layer as the growth of a damage zone; however the evidence indicates that such an approach is too simplistic. The pre-exposure/oxidation was modeled as altering the state of stress through the presence of the oxide layer and through changes in the time-dependent material behavior.

One of the parameters examined was the maximum shear strain in the cycle. Somewhat surprisingly this did not correlate at all. However, when a combination of normal and shear strain is employed, the results fall into a consistent pattern. The damage parameter that gave the best correlation was

$$D = \Delta\varepsilon_{rz} + 0.4\,\Delta\varepsilon_{rr}, \tag{4-5}$$

with the result shown in Figure 57. The results for the pre-exposure in air were obtained by determining the scale thickness from Equation 4-3, and then interpolating the finite element results for no scale and the maximum scale thickness of four microns. Similarly for the argon pre-exposure, the creep damage was estimated by interpolating and extrapolating the hold time finite element results. To do this in the absence of a multiaxial creep damage model, it was necessary to make an assumption regarding the relationship of damage and strain. It was assumed, based on the observation that specimens which had been pre-exposed in an inert environment for 50 hours had about one-half the thermal cycle life of unexposed specimens, that a 50-hour pre-exposure would represent 50% damage.

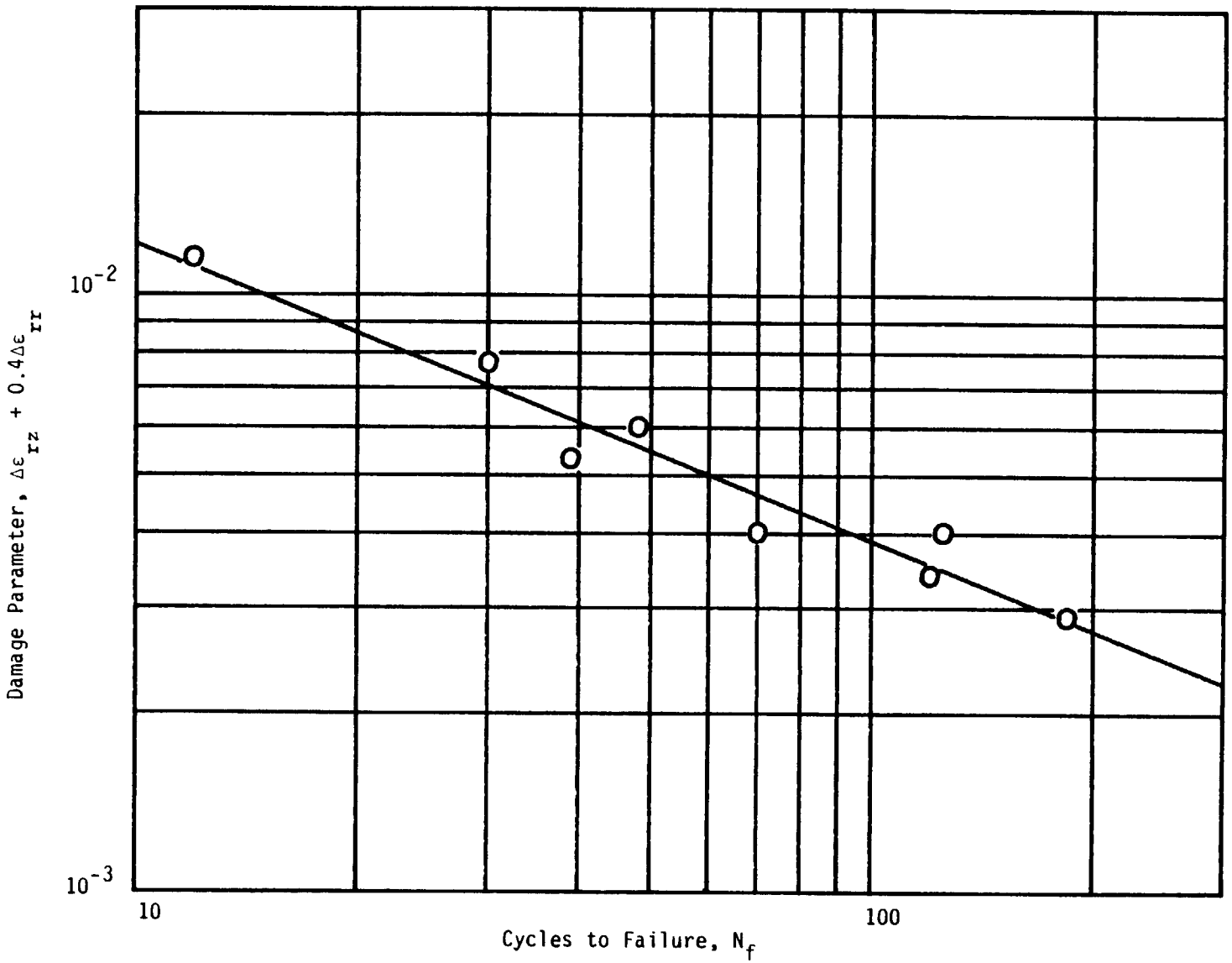

Figure 57. Relationship Between Damage Parameter and Thermal Cycles to Failure of Thermal Barrier Coated Tubular Specimens.

These considerations allowed the damage-life plot of Figure 57 to be made. A linear fit to these data gave

$$D = 0.121\, N_f^{-0.486} = \Delta\varepsilon_{rz} + 0.4\, \Delta\varepsilon_{rr}^{*} \qquad (4\text{-}6)$$

This relationship gives an excellent fit to the failure data but it must be remembered that these specimens failed in the edge areas. If conditions are such that failures take place away from an edge, the coefficients in the model may need to be altered, but it is expected that the general form of the relationship would remain the same. This will require additional TMF testing with tube specimens to determine the operating environment under which the non-edge failures could be observed. It should also be noted the failure model is based on a certain level of coating loss as a failure criterion; it is clear that a different failure definition would alter the results. Presumably the stress state associated with a fully constrained failure would be different but this presumption needs to be confirmed and its impact on the failure model ascertained.

4.3.2 Summary

The development of the failure model for the thermal barrier coatings is based on the following:

1. For the tests conducted, failure is associated with the coating edges.
2. The failure occurs within the ceramic, approximately 1 mil from the top coat/bond coat interface.
3. The failure is the result of time-dependent processes, both creep and oxidation.
4. The deformation field is shear driven due to the thermal mismatch of the materials. However, the normal strains apparently play a role in propagating the failure.
5. Extension of this failure model to other geometries and failure locations is probably possible but demonstration is beyond the scope of this program.

---

*The $\Delta\varepsilon$ refers to a range quantity. In this case, it is the difference between the maximum and minimum strains in the cycle. In figures such as Figure 33, the strain components themselves are plotted; hence, the difference between the strain at time 1 and time 2 would be:

$\Delta\varepsilon_{rr} = \varepsilon_{rr}(\tau 2) - \varepsilon_{rr}(\tau 1)$

5.0 TASK III - MODEL VERIFICATION

The objective of this task was to verify the major mode life-prediction model which was developed in Task II. This was attempted by using the model to predict the furnace cycle test lives of several coating variations and specimen geometries, then comparing these predicted lives to experimentally determined test lives.

5.1 Life Prediction

Test lives were predicted for 11 combinations of coating and specimen variations. Included were three coating systems, three specimen geometries, two top coat thicknesses, and two edge conditions. Coating system (bond coat) variations were NiCrAlY, aluminide-coated NiCrAlY, and aluminide-coated bond coat No. 4 (see Section 3.4). Specimen geometry variations included tubes and rods, and three specimen diameters: 6.3, 14.3, and 15.9 mm. Top coat thicknesses were 0.25 mm (10 mils) and 0.76 mm (30 mils). Both tapered and untapered edges were included.

Test lives were predicted for each of the 11 selected variations by performing finite element analyses to compute the normal and shear strains in the top coat at the most severe location, (i.e., at the edge of the coating), and using an equation similar to equation 4-6 to predict the life of each.

Before applying equation 4-6 however, it was necessary to modify the intercept of the line fitted to the data of Figure 57. This was necessary because a number of changes had been made to the model of the TBC coated cylinder over the life of the program to improve the accuracy of the model. Since the verification experiments were intended to demonstrate the capabilities of the model, it was deemed appropriate to include all improvements made during the program. The disadvantage of this was that the model used for the pre-exposure and verification analyses were not exactly the same. Specifically, the changes were:

1. The finite element mesh was altered to improve performance in the region of greatest interest, the bond coat-top coat interface.
2. The inclusion of the oxide scale was accomplished through thermal mismatch analysis. This allowed the incorporation of bond coat properties rather than the previously used René 80 properties.
3. The most significant change was the use of strain values from the finite element anaylsis of the second thermal cycle rather than the first. It had been found that the first thermal cycle was not representative of the stable cyclic behavior of the specimens, thus a second cycle was included in the finite element analysis.

Although it would have been desireable to rerun the analyses for the pre-exposure specimens with the improved procedure, this was not feasible. Thus, when it was found that the strain values calculated for the baseline specimen (no pre-exposure) using the updated model were larger than those which had been obtained using the earlier model, it was necessary

to revise equation 4-6. It was assumed that the new model and cycle would merely increase all the strain ranges by a similar amount, thereby shifting the data in Figure 57 to the right. This procedure kept the slope of the curve the same but increased the intercept. The expression used to predict the damage in the verification tests was:

$$0.135\ N_f^{-0.486} = \Delta\varepsilon_{rz} + 0.4\ \Delta\varepsilon_{rr} \qquad (5\text{-}1)$$

The accuracy of the assumptions and procedures that went into this model will be explored in the next section.

5.2 Test Results

Triplicate specimens were prepared of each variation and tested in the furnace cycle test at 1093°C. Average test lives are compared to the predicted lives in Table XIV. Test lives are shown in Figure 58 for all specimens. Generally, the model correctly predicted the trends associated with the coating and specimen variations, such as lives decreasing with increasing top coat thickness, longer lives associated with tapered top coats, and decreased lives associated with air pre-exposures. However, there were significant differences between the predicted and actual test values in many cases, indicating that more testing and data are needed to refine the model. A discussion of the results is presented below.

Clearly, the model correctly predicts that TBC life decreases with increasing top coat thickness (Groups A and F, and Groups E and G). However, the actual decrease was significantly larger than that predicted. The difference may be the result of the development of higher levels of residual stress in thicker coatings. The model does include coating application history to a degree, but it does not include change in substrate temperature during top coat application as the coating builds up and increases in insulating value. Since this effect would be expected to be larger for thicker coatings, the larger than expected difference between thin and thick coatings may not be associated with inconsistencies in the model, but with the difference in conditions during coating application.

Slightly longer lives were noted for tapered specimens from Groups A and I, while no differences were noted for Groups H and J, and Group G and K. Since the lives were unexpectedly very short (coating failure was observed at first inspection in all cases except one) in the latter groups, it is not surprising that the effect was not clearly differentiated. However, the difference in life for Groups A and I, was much smaller than expected. The smaller than expected change may be associated with the ability to produce a nontapered edge. The nontapered edge was produced by masking the coating and grit blasting away some of the top coat to remove the taper. Hence, it is possible that the idealized square edge used to calculate the strains in the model was not realized on the actual specimens. Thus, it is possible that the difference between the actual lives of the tapered and nontapered coatings should be smaller than predicted.

Table XIV. Comparison of Predicted and Actual Test Lives.

	Specimen Geometry	Specimen Diameter, mm	Bond Coat	Top Coat Thickness, mm	Preoxidized 100 Hours at 1093°C	Tapered Edge	Predicted Life	Actual Life	Variation
A	Tube	14.3	NiCrAlY	0.25	No	Yes	127	102	Baseline
B	Rod	15.9	NiCrAlY	0.25	No	Yes	106	120	Geometry
C	Rod	6.3	NiCrAlY	0.25	No	Yes	109	67	Geometry
D	Tube	14.3	NiCrAlY + Codep	0.25	No	Yes	109	58	Bond Coat
E	Tube	14.3	Bond Coat No. 4 + Codep	0.25	No	Yes	33	60	Bond Coat
F	Tube	14.3	NiCrAlY	0.76	No	Yes	92	20	Top Coat Thickness
G	Tube	14.3	Bond Coat No. 4 + Codep	0.76	No	Yes	24	5	Top Coat Thickness/ Bond Coat
H	Tube	14.3	NiCrAlY	0.76	Yes	Yes	41	5	Top Coat Thickness/Preoxidation
I	Tube	14.3	NiCrAlY	0.25	No	No	53	95	Nohtapered Edge
J	Tube	14.3	NiCrAlY	0.76	Yes	No	15	7	Top Coat Thickness/Nontapered Edge/Preoxidation
K	Tube	14.3	Bond Coat No. 4 + Codep	0.76	No	No	10	5	Top Coat Thickness/Bond Coat/ Nontapered Edge

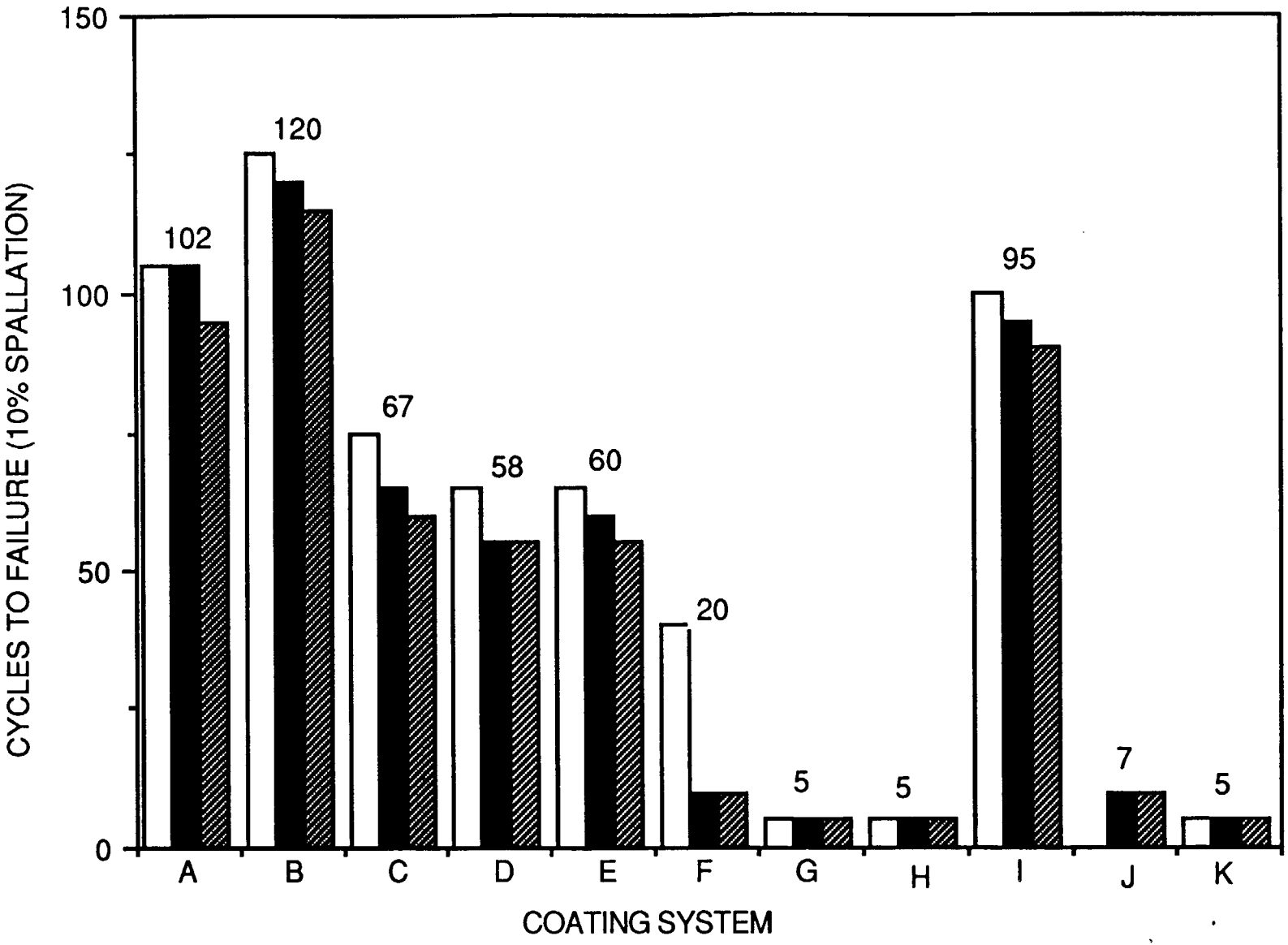

Figure 58. Furnace Cycle Test (1093°C) Life for Specimens with Selected Specimen and Coating Variations to Test Validity of Life Model. See Table XIV for Specimen and Coating Descriptions. (Numbers Above the Bars are Averages.)

case, however, much of the decrease may be associated with this evaluation of thicker coating [0.76 mm, 30 mils)] as discussed above.

The model also predicted that essentially equal lives would occur for the three different geometries included in this experiment (Groups A, B, and C). Essentially equal lives were noted for Groups A (14.3 mm tube, 102 cycles) and B (15.9 mm rod, 120 cycles). However, the lives of the Group C specimens (6.3 mm rod, 67 cycles) were one-half the lives of the two larger diameter specimens. Examination of the heating and cooling rates of the specimens indicated that the cooling rates were more severe for the 6.3 mm rods (smaller mass) than the larger rods and tubes. Hence, it is likely that the shorter life can be attributed to the faster cooling and heating rates. The slightly longer lives of the 15.9 mm diameter rod specimens (greater mass) relative to the tube specimens may also be attributed to cooling and heating rates since the rod specimens heated and cooled slightly slower than the tubes. Cooling and heating rates are not currently modeled as part of this program since a "standard" test condition only was evaluated.

The most disappointing results were for the specimens with aluminide (Codep) coated bond coats. Test lives of these specimens were much shorter then previous results (Figure 20) and much shorter than the predicted lives. In this case, it is clear from post-test analysis that the problem is not with the model but with the specimens. One problem that can occur when bond coats are aluminide overcoated is that their "effective" surface roughness (surface texture) is reduced. The reduction in surface roughness due to the aluminide coating is usually not detectable by conventional profilometer measurements. The aluminide coating reduces the roughness of minor peaks and valleys on the bond coat surface by filling them in (Figure 16) but does not significantly reduce the heights of the major peaks and valleys. Therefore, measured surface roughness does not decrease, but the "effective" surface roughness of the bond coat for bonding is decreased, and thus the coating life may be decreased. This has been observed in other GE work where aluminiding has been used. One solution to achieve more consistent results is to use a coarser spray powder for the bond coat; this results in a greater surface roughness. Whether poor results occur or not probably depends on the actual thickness of the aluminide coating in a given coating run. Since all of the coatings used to generate the model were made with -230 + 400 mesh powder (the model does not address different bond coat surface roughnesses), no change was made for the verification experiment.

Obviously, more data and fine tuning is required together with the addition of fracture mechanics, to make the life prediction model developed during the first phase of this program an effective tool to predict TBC life. However, the model can be used to predict the effect of changes to the TBC system and be used as a framework for future TBC models.

It is felt that the development work applied to this life prediction model is a positive step in the use and advancement of TBC technology. It is anticipated that, with further refinement, the model will not only provide a useful tool for predicting coating life, but will also promote increased understanding of TBC behavior and the factors which influence it. As a result, a more solidly based rationale will emerge for development work aimed at improving TBCs.

6.0 CONCLUSIONS

- A TBC life prediction model was developed for a thermal cycle test based on thermal cycle test results, finite element models, and thermomechanical experiments.
- Inelastic time dependent finite element models were developed for TBCs.
- Experimental results indicate that bond coat oxidation is a significant contributor to the TBC failure. The modeling work indicates that the presence of a thin oxide scale on the bond coat can be beneficial due to the similarity in thermal expansion properties of the scale and top coat. However, it must be remembered that stresses that may be expected to occur as a result of the volume expansion associated with the growth of the oxide scale were beyond the capabilities of the current computer programs and were therefore not included in the model.
- Experimental results indicate that specimens with bond coats which have higher creep strengths have longer thermal cycle test lives; however, life prediction analysis predict the opposite, i.e., shorter thermal cycle test lives for specimens with higher bond coat creep strengths.
- TBC life is foreshortened if its initial exposure at elevated temperature is an environment which promotes the development of oxide scales other than Al_2O_3.
- TBC life can be extended by locating the edges of the TBC away from the hottest areas.
- TBC life decreases with increasing top coat thickness.

7.0 RECOMMENDATIONS

The following recommendations are offered for further studies.

1. The failure of plasma-sprayed TBCs is a complex function of the properties of the materials in the bond coat and top coat layers, the influences on these properties of the defects produced by the plasma spray process, and the response of these to thermal cycling. The cracking process should be documented, along with the interaction among the developing defects, by studying the development of flaws during the coating application process and during testing.

2. A larger data base on the physical and mechanical properties of plasma-sprayed ZrO_2 and plasma-sprayed bond coat alloys should be established to provide realistic property data for use in analytical studies. Basic constitutive properties, creep and strength values should be determined.

3. Given the necessary presence of cracks in the coating, a model should be developed which includes the effect of cracks. This model should allow the cracks to open and close and carry crack closure loads realistically.

4. An analytic methodology to gradually grow oxide scale on the bond coat in the finite element model should be developed. Appropriate properties for the oxide scale as a function of thickness and chemistry changes need to be available.

5. The model should be improved in its capability to separate time dependent behavior into material oxidation and constitutive response.

6. The model and experimental work should be extended to predict the life of the coating on specimens in a Mach 0.3 burner rig test, which would be more representative of actual operating conditions.

7. Fracture and continuum mechanics life prediction models should be developed.

8. The model should be modified to include failure of TBCs produced by the physical vapor deposition (PVD) process.

APPENDIX A - POWDER CHARACTERISTICS

Table A-1. Powder Manufacturers.

Manufacturer	Powder	Powder Size, Mesh
Alloy Metals, Inc.	Bond Coat No. 1 (Ni-22Cr-10Al-0.3Y)	- 230 + 400
Union Carbide	Bond Coat No. 2 (Special)	- 230 + 400
Union Carbide	Bond Coat No. 3 (Special)	- 230 + 400
Union Carbide	Bond Coat No. 4 (Special)	- 230 + 400
Metco	Top Coat (ZrO_2-$8Y_2O_3$)	- 140 + 10 μm

Table A-2. Powder True Density*.

Powders	Density (g/cc)
Bond Coat No. 1 (Ni-22Cr-10Al-0.3Y)	7.31
Bond Coat No. 2	8.35
Bond Coat No. 3	7.88
Bond Coat No. 4	7.36
Top Coat (ZrO_2-Y_2O_3)	5.53

*Density of as-received powder (Null-Pychometer)

Table A-3. Powder Sieve Analysis (Weight %).

Sieve Size (mesh)	Bond Coats No. 1	No. 2	No. 3	No. 4	Top Coat ZrO_2-8Y_2O_3
+ 170	0.0	0.0	0.0	0.0	10.0
- 170 + 200	0.4	0.8	0.0	0.0	13.7
- 200 + 250	14.7	7.6	0.8	0.0	5.7
- 250 + 270	34.5	27.7	23.5	14.8	9.5
- 270 + 325	29.2	32.4	34.6	36.7	13.7
- 325 + 400	12.2	25.1	28.0	32.6	9.4
- 400	9.0	6.3	13.0	15.8	38.1

Table A-4. Powder Microtrac Analysis.

Powders	10th Percentile μm	50th Percentile μm	90th Percentile μm	Mean Diameter μm
Bond Coat No. 1	34.5	52.8	83.2	54.9
Bond Coat No. 2	36.7	57.1	90.2	57.8
Bond Coat No. 3	30.6	51.6	96.5	56.3
Bond Coat No. 4	37.7	55.2	84.4	56.3
Top Coat	27.7	62.4	115.9	65.7

APPENDIX B - BOND COAT MICROSTRUCTURE

Phase identifications of bond coat microstructure after pre-exposure and thermal cycle testing are shown in Figure B-1. In all cases, the application of an aluminide overcoat has resulted in a microstructure containing a high Al β (NiAl Type) matrix. The phases labeled include γ (Ni solid solution), γ' (Ni_3Al) type, β (NiAl type), and $M_{23}C_6$. In some cases, certain phases which can only be identified by X-ray diffraction or election microprobe are labeled as "other phases". These other phases can include carbides, oxides, the sigma phase, the Mu phase, and the α - Cr phase.

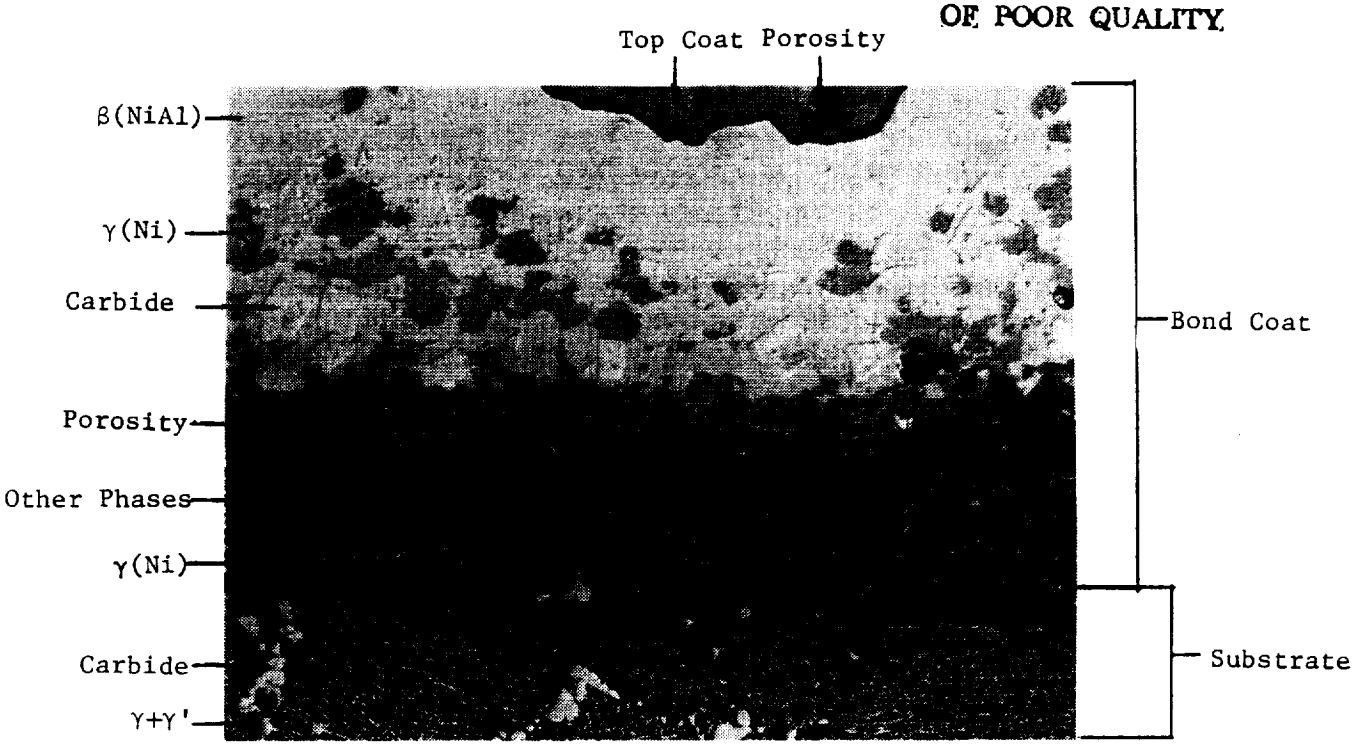

a. Bond Coat No. 2 - 100 Hour Air Pre-Exposure (No Thermal Cycles)

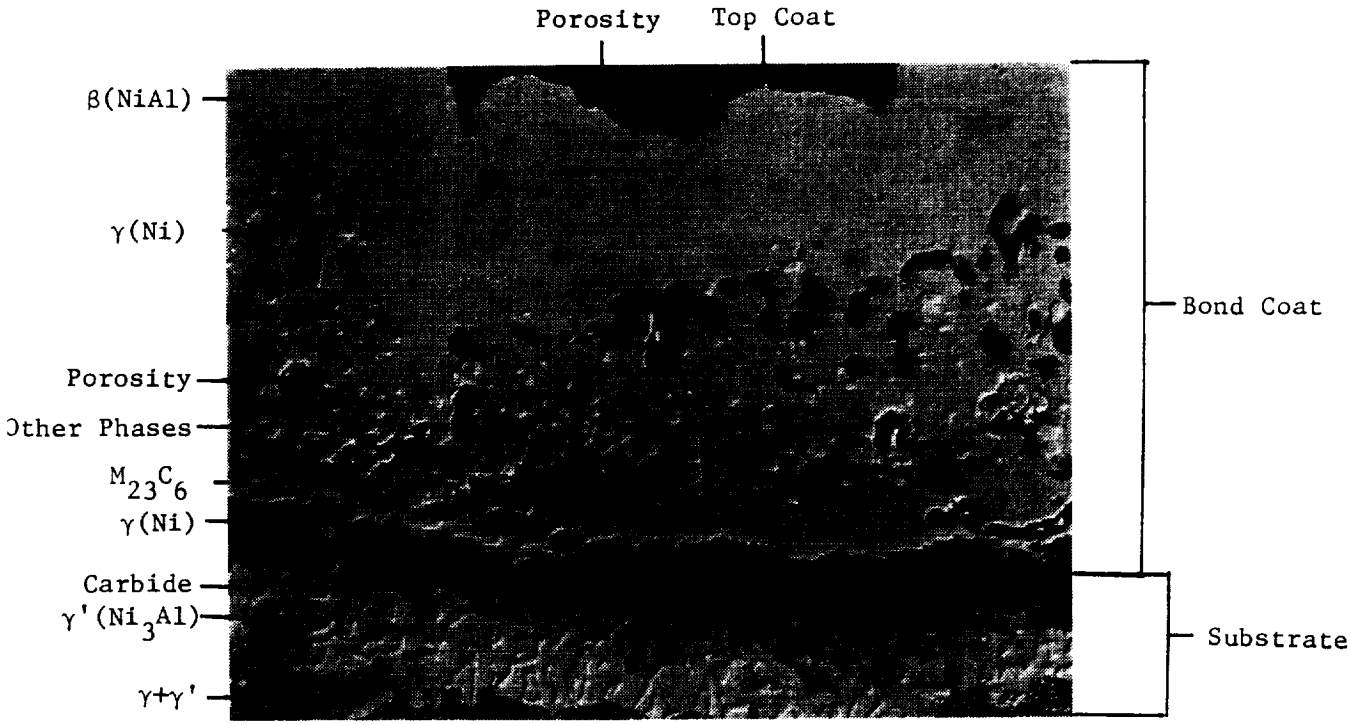

b. Bond Coat No. 1 - 100 Hour Argon Pre-Exposure (No Thermal Cycles)

Figure B-1. Phase Identification of Bond Coat Microstructure After Pre-Exposure and Thermal Cycle Testing.

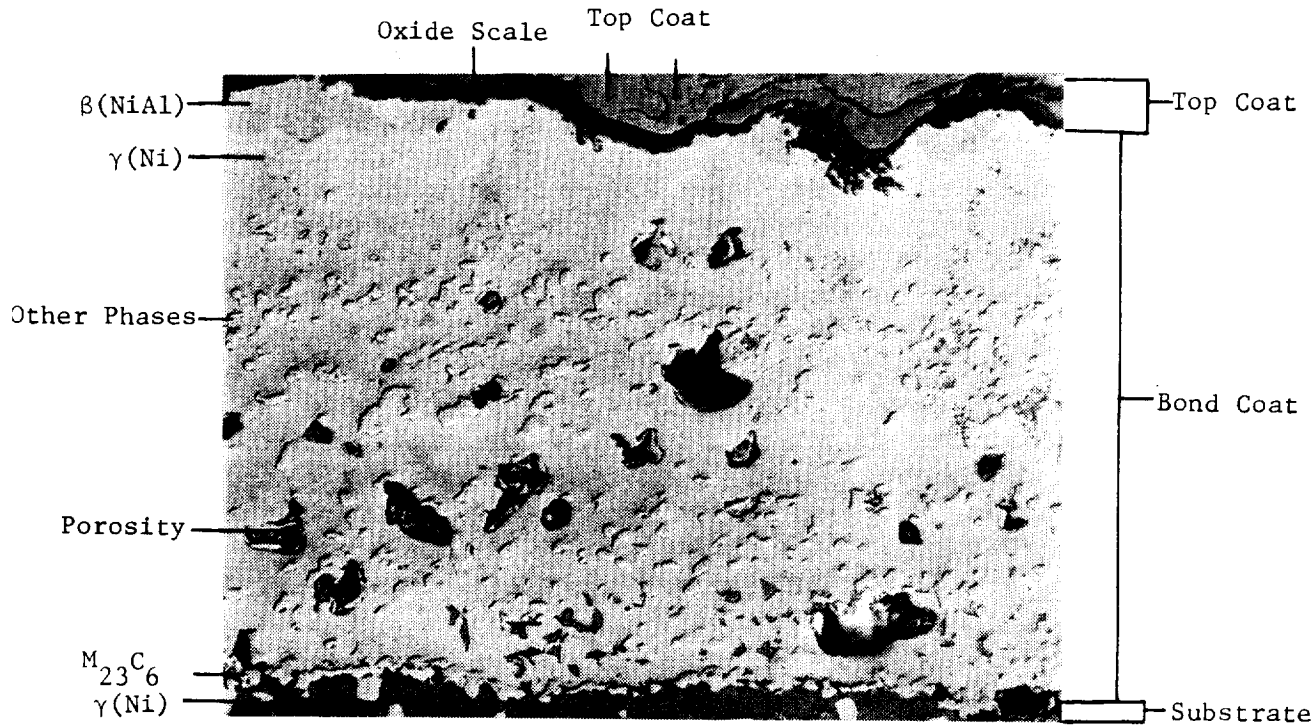

c. Bond Coat No. 4 - 100 Hour Air Pre-Exposure (After 470 Thermal Cycles)

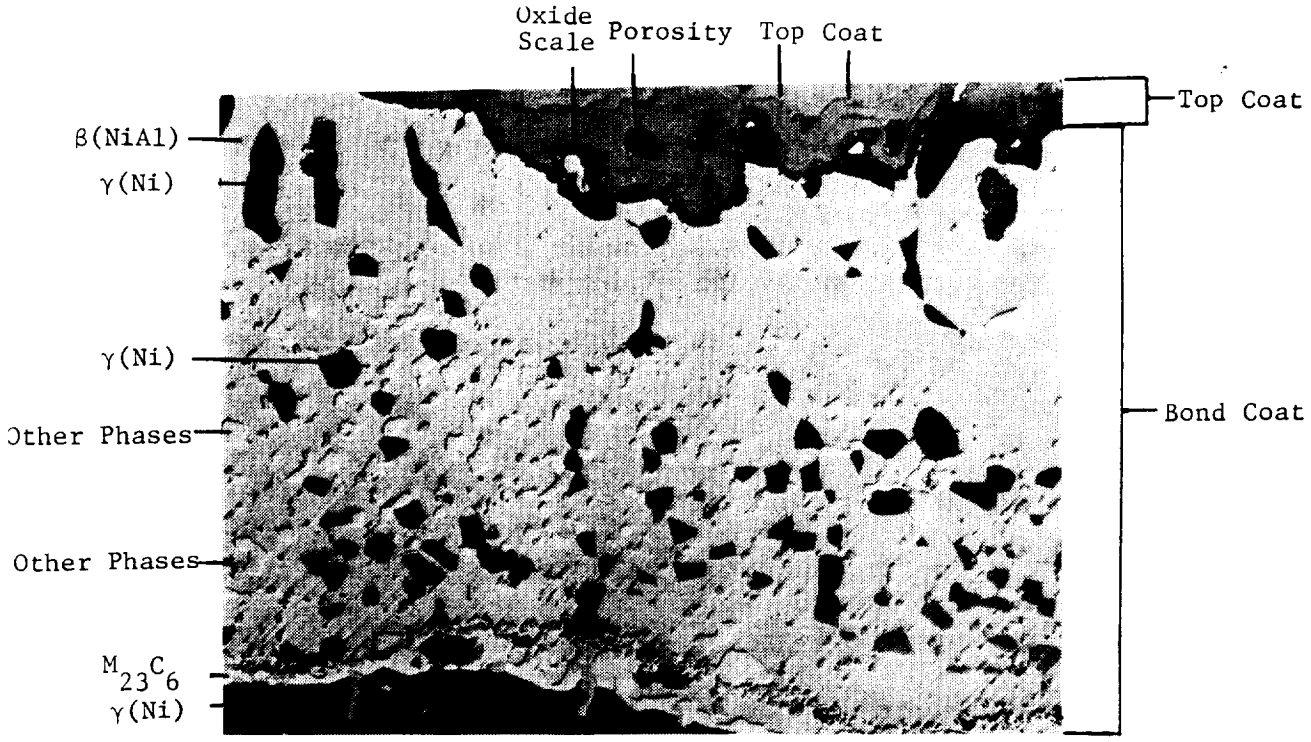

d. Bond Coat No. 3 - 100 Hour Argon Pre-Exposure (After 320 Thermal Cycles)

Figure B-1. Phase Identification of Bond Coat Microstructure After Pre-Exposure and Thermal Cycle Testing (Concluded).

APPENDIX C - CYANIDE FINITE ELEMENT PROGRAM

CYANIDE is a two-dimensional finite element program which can handle either plane stress, plane strain, or axisymmetric deformation. The program can analyze structures subjected to any complex cyclic thermomechanical loading conditions including concentrated loads, pressure loads, thermal loads, and centrifugal loads. CYANIDE accounts for both time-independent plastic flow and time-dependent creep deformation.

Plasticity is accounted for by using a modified Besseling subvolume method with multilinear stress-strain curves which are temperature dependent. A typical stress-strain representation for one temperature is shown in Figure C-1. This method automatically reproduces certain aspects of real-material behavior important in the analysis of engine components. These include the Bauschinger effect, cross hardening, and memory. In addition to simulating the material response very closely, Besseling's method is also more economical than other methods. Implementation of the method involves revising the force vector by computing plastic forces which account for the plastic flow:

$$[K]\,[\delta] = [F] + [F_p] \qquad \text{(C-1)}$$

where K is the elastic stiffness,
δ is the incremental displacement,
F is the applied force
F_p is the plastic force.

Since the method does not require modification of the stiffness matrix in the plastic iterations, it is consequently very economical.

The creep analysis utilizes one of two possible creep representations. When tertiary creep is not considered to be of importance, the equation used is:

$$\varepsilon_c = k\,\bar{\sigma}_e^{n} t^{m} + q\,\bar{\sigma}_e^{r}\,t \qquad \text{(C-2)}$$

where
$\bar{\sigma}_e = \sigma_e/100000$, σ_e = effective stress
and
k, m, n, q, r = material-dependent and temperature-dependent creep coefficients.

This type of response is shown for one temperature in Figure C-2.

When the material exhibits a significant amount of tertiary creep capability, an alternate representation is used. Primary creep is represented by the Bailey-Norton law.

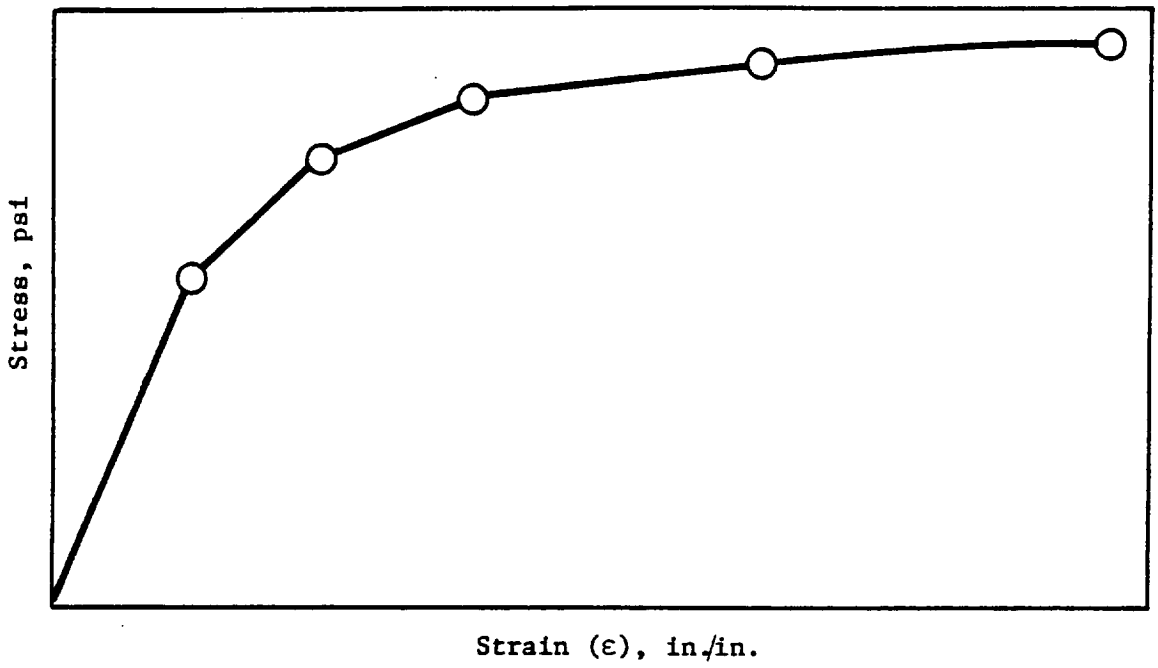

Figure C-1. Point by Point Stress-Strain Curve Representation.

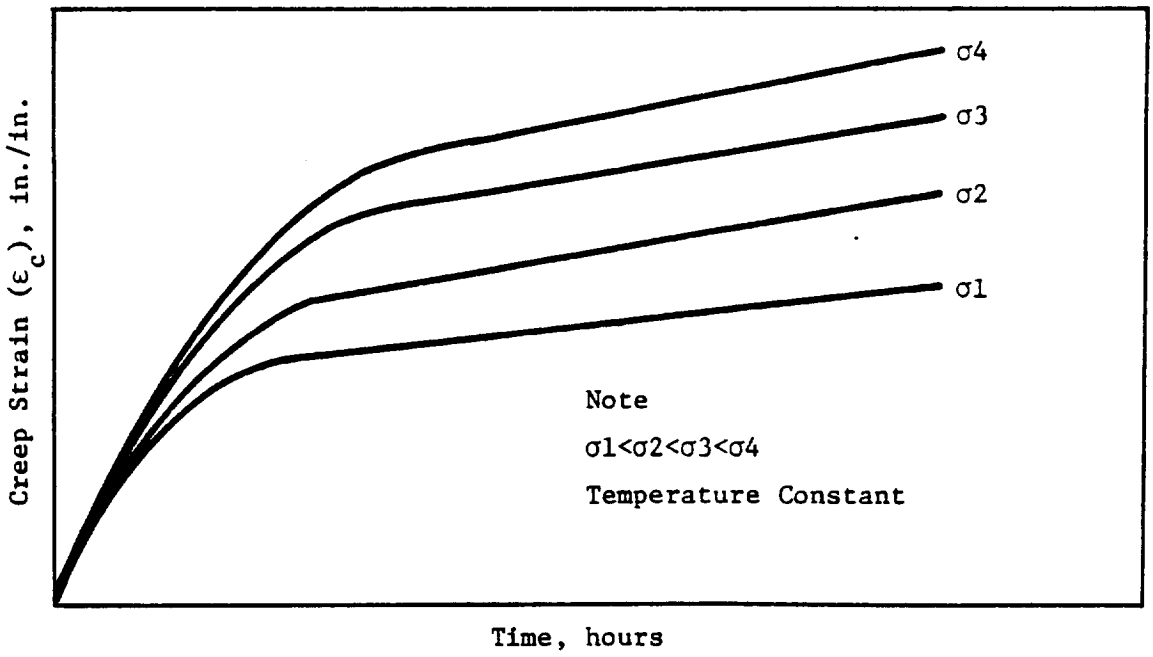

Figure C-2. Creep Curve Representation for Constant Temperature.

$$\varepsilon_c^P = A1\ \bar{\sigma}_e^{A2}\ t^{A3} \tag{C-3}$$

Secondary creep is modeled with the expression proposed by Marine, Pao, and Cuff (42)

$$\varepsilon_c^S = A4\ \bar{\sigma}_e^{A5}\ t + A6\ \bar{\sigma}_e^{A7} \tag{C-4}$$

Tertiary creep is represented with an equation of the form

$$\varepsilon_c^T = A8\ \exp A9\ \bar{\sigma}_e^{A10}\ t \tag{C-5}$$

A1, A2 ... A10 = material-dependent and temperature-dependent creep coefficients. This type of response is shown for one temperature in Figure C-3.

CYANIDE also contains an orthotropic creep formulation. The creep strain rate is assumed to be given by

$$\varepsilon_{ij} = g_{ijk1}\ \sigma_{k1} \tag{C-6}$$

where

ε_{ij} = strain rate tensor
σ_{k1} = stress tensor
g_{ijk1} = tensor with components that are functions of temperature, σ_e, and hardening rule and are derivable from input creep curves.

The user can select from time hardening, strain hardening, or life fraction creep rule, depending on the actual material characteristics. Strain hardening is ordinarily adequate for describing hardening behavior, providing that stress reversals do not occur. A stress reversal is considered to occur when

$$(\varepsilon_{ij})_c\ \sigma_{ij} < 0 \tag{C-7}$$

where$(\varepsilon_{ij})_c$ is creep strain measured from the current origin. When a reversal occurs the origin is changed, and the analysis proceeds (43).

The combination of general creep equations and creep rule makes the program very general in application to structures which undergo time-dependent inelastic deformation. A

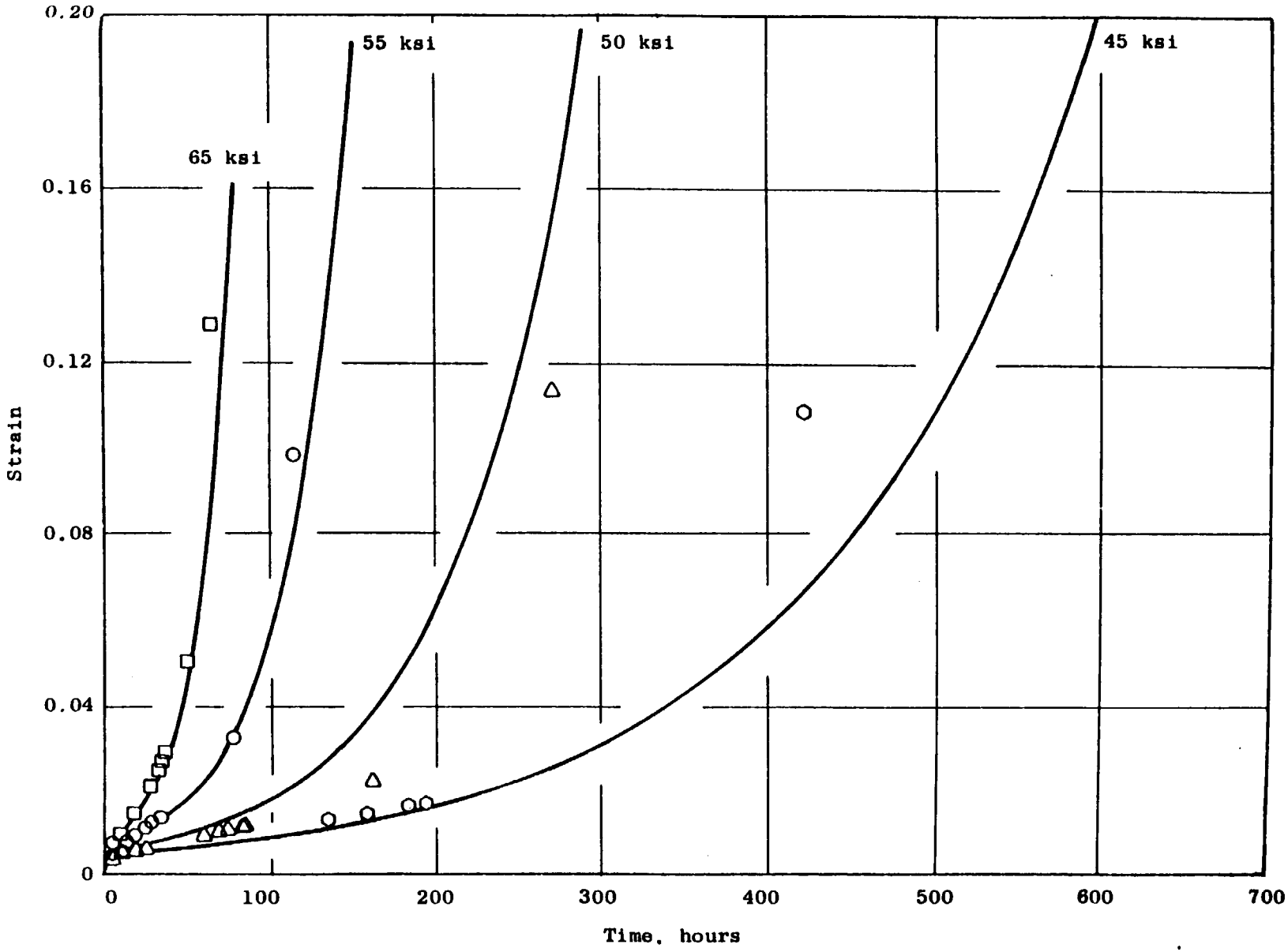

Figure C-3. Creep Strain Versus Time for Several Stress Levels, DS René 80 Material.

solution is done for each time step using an iterative technique to predict incremental creep strain components and revise the right side of the basic structural stiffness matrix equation by adding a plastic force vector to account for the creep effects

$$[K]\{\delta\} = \{F\} + \{F_{P_C}\} \quad . \quad \text{(C-8)}$$

in a manner similar to that used in the Besseling technique for time-independent plasticity. Again, this method is very efficient; very large problems can be solved economically, and convergence has been shown to be very rapid. The benefits of the CYANIDE finite element program will be more evident when creep relationships are introduced later in this TBC analysis effort.

APPENDIX D - PRELIMINARY MODELING EFFORT

Two-dimensional finite element models were used to determine the stress and deformation fields in the TBC specimens. Several finite element models were examined and an axisymmetric model was selected to evaluate the fields. These results provided an important step in the development of TBC life prediction models.

For the axisymmetric model, a longitudinal slice of a multilayer cylinder (Figure D-1a) was examined. In this case, the assumption was made that the specimen model was sufficiently long that the cross sectional planes (perpendicular to axis) remain planar after deformation. For this geometry, two different axisymmetric models were investigated. The first had two layers in the axial direction (Figure D-1b), with the elements in the right layer made extremely rigid to resist the axial and shear deformation. The second model (Figure D-1c) had many layers in the axial direction, with the last layer very long (10:1 aspect ratio, not shown) in the axial direction. In both models, the goal was to enforce the uniform axial deformation.

After careful examination, the decision was made to utilize the second axisymmetric model (Figure D-1c).

The axisymmetric finite element model was used in two analytical tasks. Initially, the bond coat stress free temperature was assumed to be 982°C (1800°F), while the top coat stress free temperature was assumed to be 204°C (400°F). These are the temperatures of the substrate during application of these coatings. The material properties utilized in the model are listed in Appendix E. Stresses, which include effective, radial, axial, and hoop, were computed across the top coat, the bond coat, and the substrate in the radial direction. Both elastic and plastic deformation were included in the analysis, but no plasticity developed for the temperature conditions selected (time at temperature was not included). Analysis of the results for these two analytical tasks is discussed below.

In the first analysis, the specimen was assumed to undergo the thermal cycle of 21°C - 1093°C - 21°C in the furnace cycle test. Since this is a quasistatic test, the entire specimen was assumed to be at a given temperature. Effective, radial, axial, and hoop stresses versus distance in the radial direction are plotted in Figures D-2 through D-5 for four different temperatures [21°C (70°F), 204°C (400°F), 982°C (1800°F), and 1093°C (2000°F)]. As indicated, the stress-free temperature for the top coat was taken as 204°C (400°F); therefore, zero stress was found in the top coat at this temperature. However, after the top coat was applied to the bond coat, 982°C (1800°F) was no longer the bond coat stress-free temperature. Therefore, small stresses due to the top coat application are present in the bond coat at this temperature.

As observed in all plots, the model predicts extremely large stresses in the bond coat and top coat at 1093°C (2000°F). The high stresses in the top coat are probably relieved by microcracking. The results also indicate that large compressive stresses do develop in the

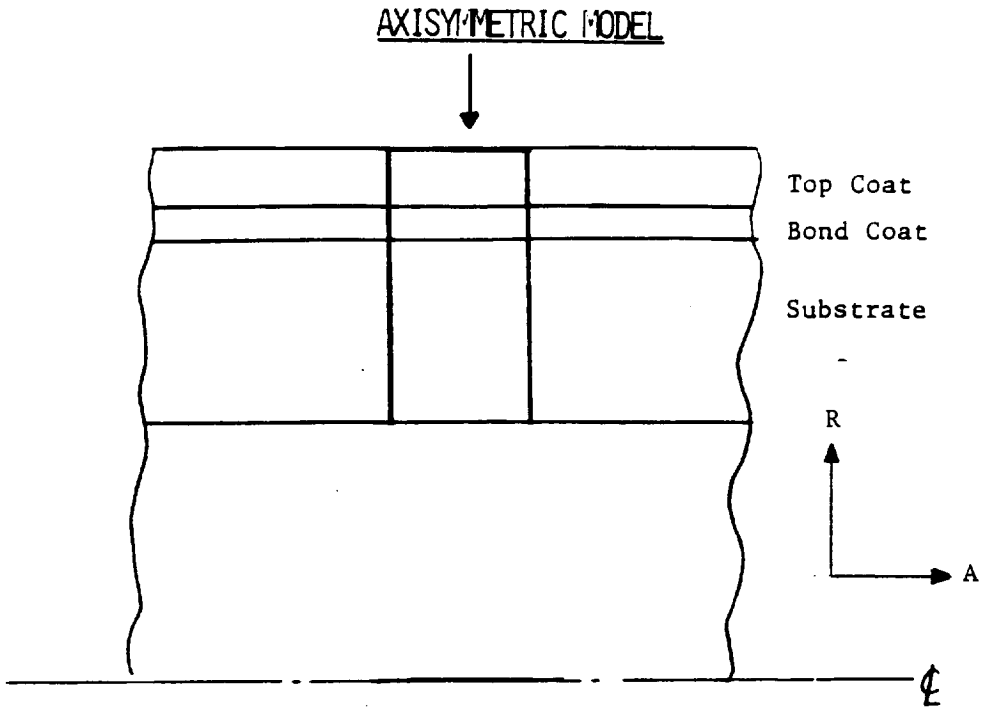

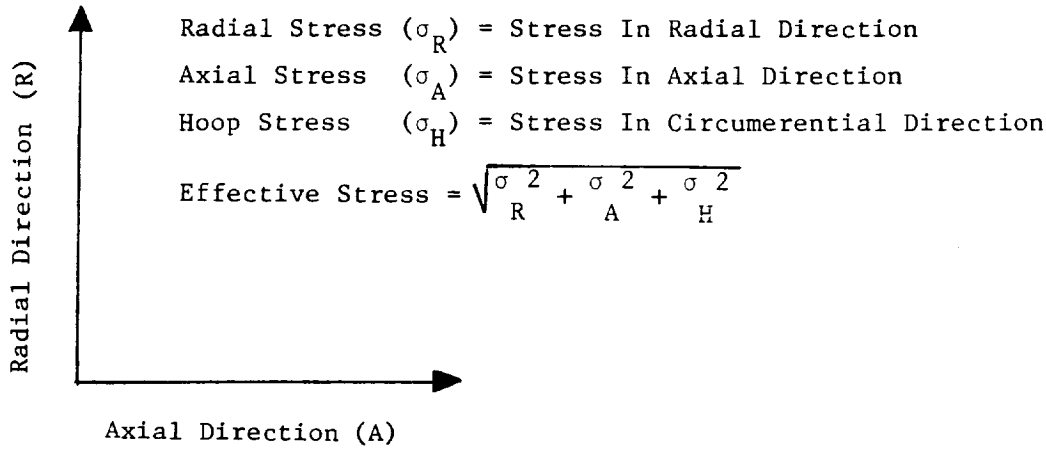

a. Longitudinal Slice of Multilayer Cylinder.

Figure D-1. Axisymmetric Model.

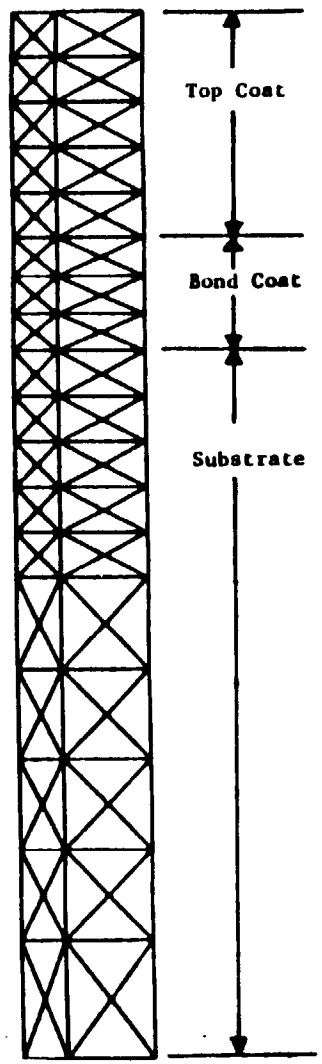

b. Layers of Finite Elements (Model 1)

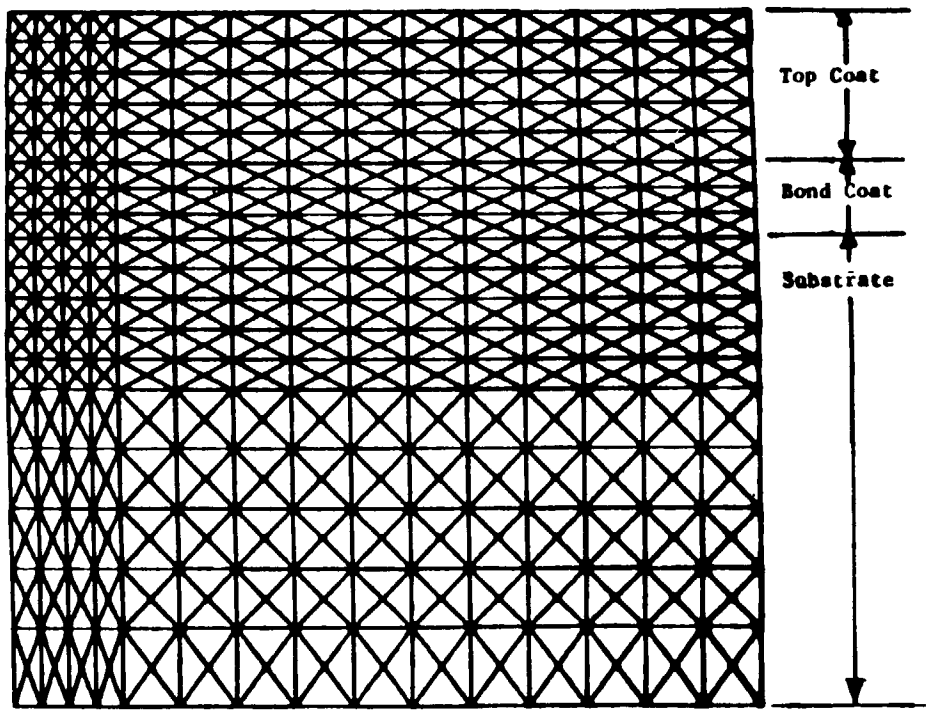

c. Layers of Finite Elements (Model 2)

Figure D-1. Axisymmetric Model (Concluded).

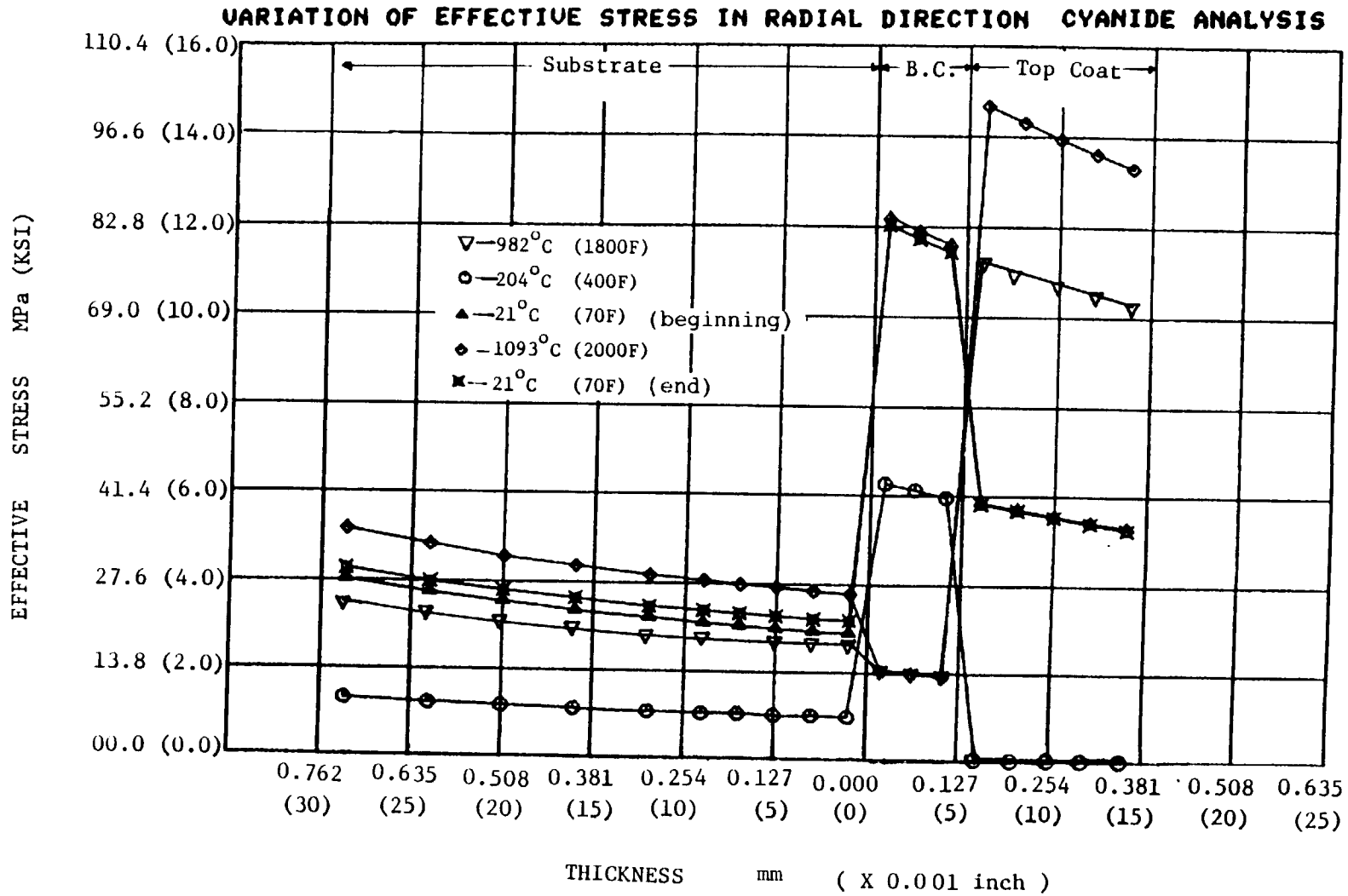

Figure D-2. Plot of Effective Stress Versus Distance in the Substrate, Bond Coat, and Top Coat in the Radial Directions, CYANIDE Analysis for Task A (No Temperature Gradient).

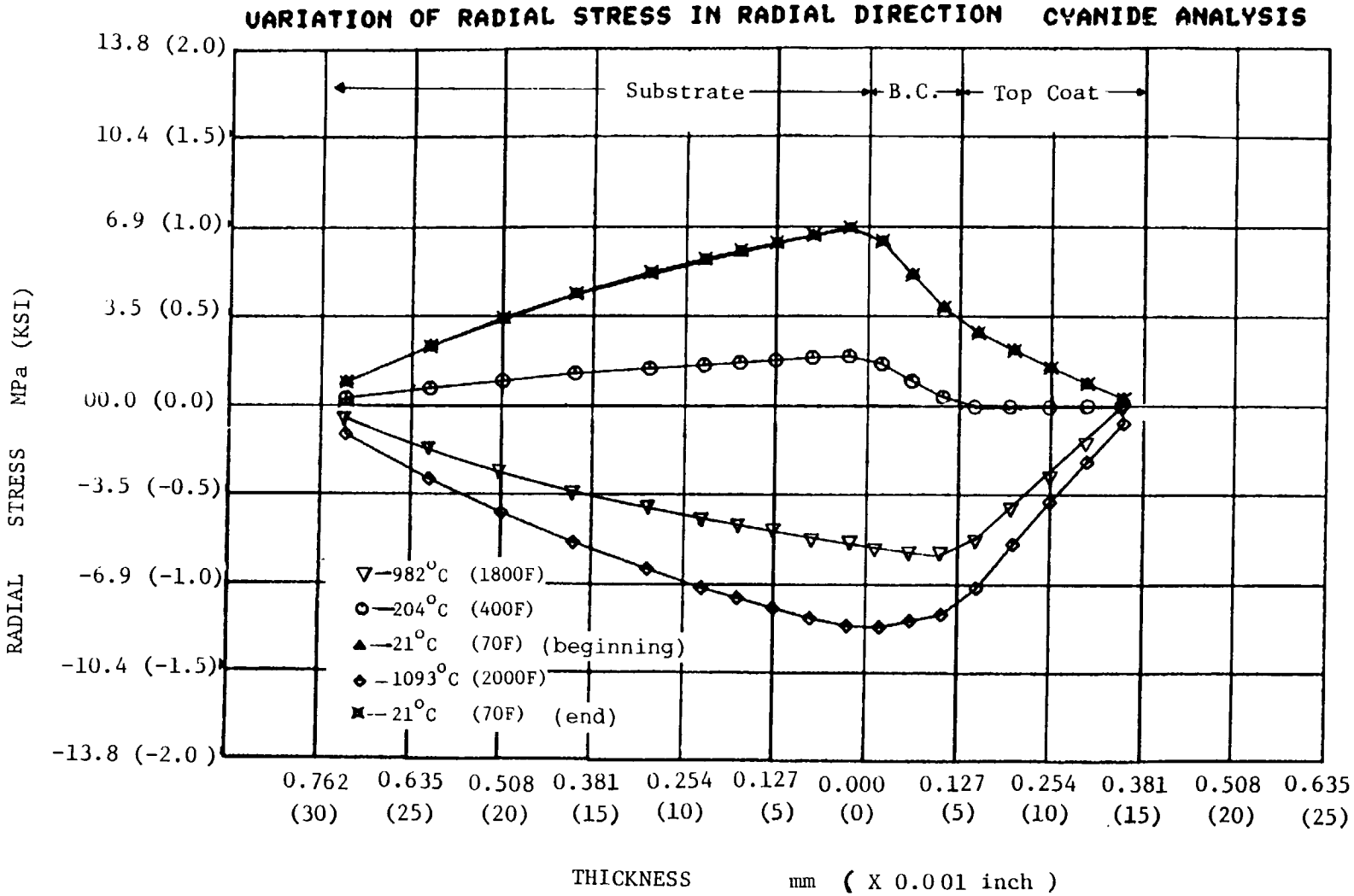

Figure D-3. Plot of Radial Stress Versus Distance in the Substrate, Bond Coat, and Top Coat in the Radial Directions, CYANIDE Analysis for Task A (No Temperature Gradient).

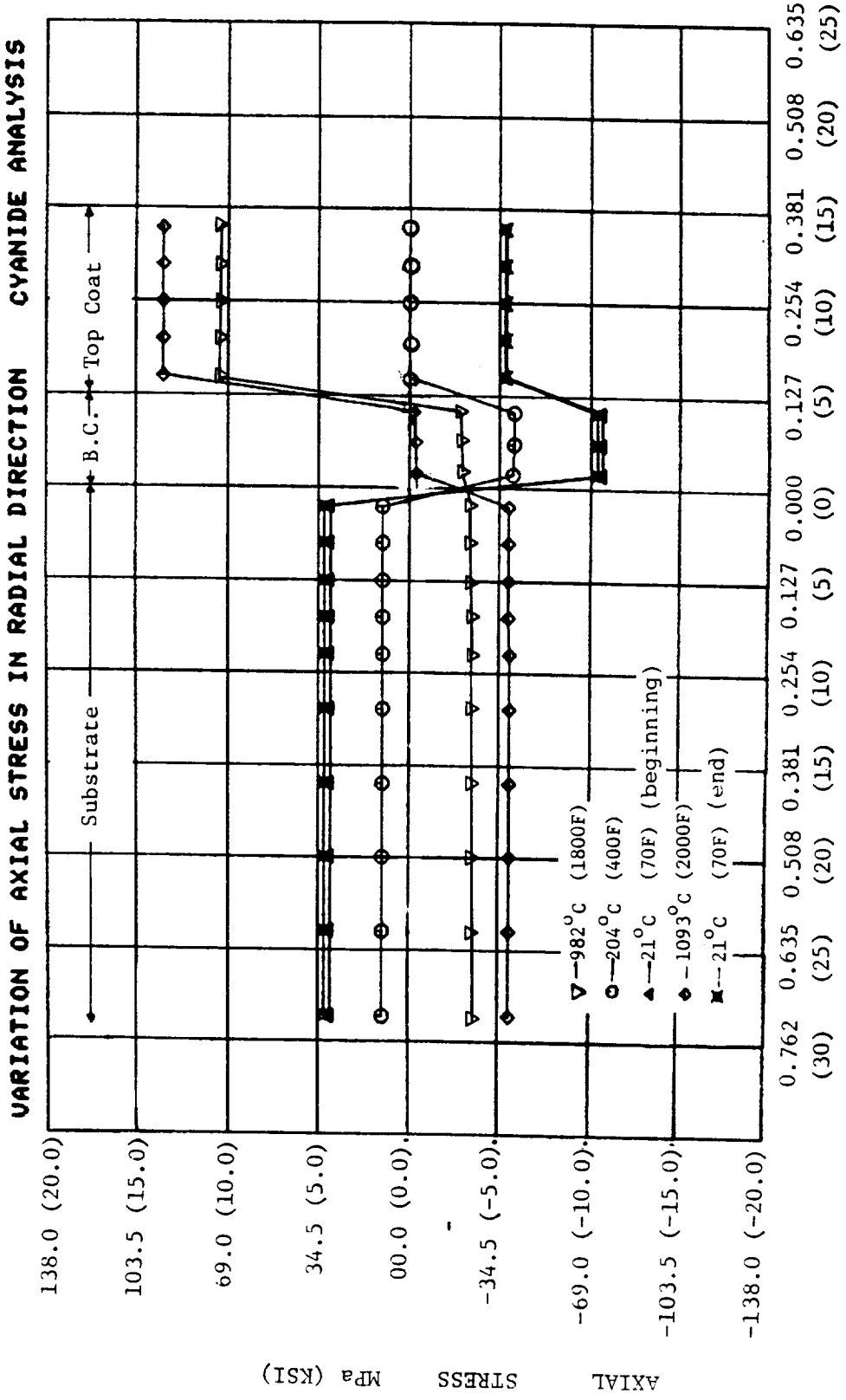

Figure D-4. Plot of Axial Stress Versus Distance in the Substrate, Bond Coat, and Top Coat in the Radial Directions, CYANIDE Analysis for Task A (No Temperature Gradient).

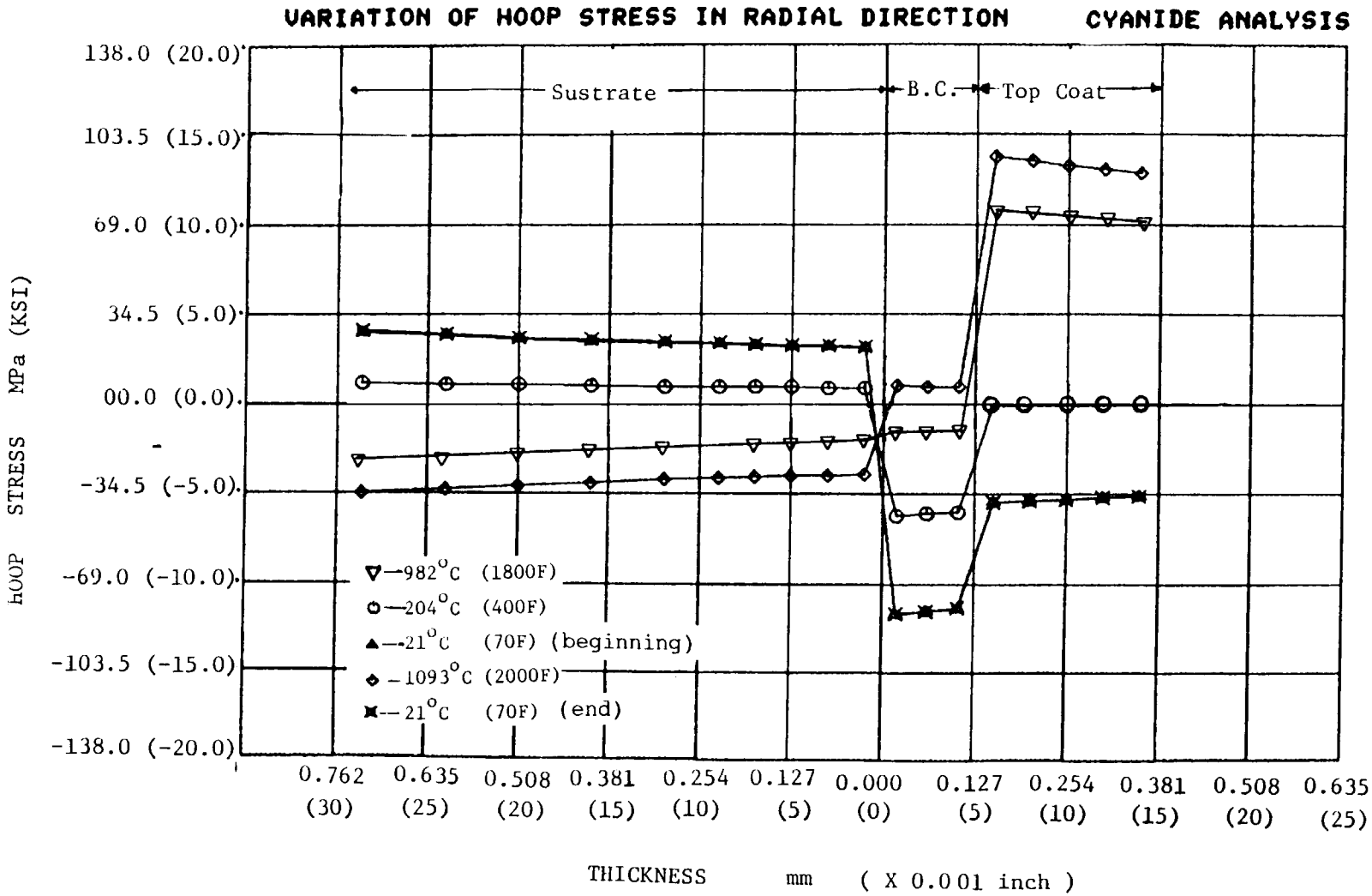

Figure D-5. Plot of Hoop Stress Versus Distance in the Substrate, Bond Coat, and Top Coat in the Radial Directions, CYANIDE Analysis for Task A (No Temperature Gradient).

ceramic as the temperature decreases. This is consistent with most theories associating TBC failure with the large compressive stresses that develop in the ceramic upon cooling.

In the second analytical model, a temperature distribution across the TBC system was modeled. In this study, the surface of the ceramic was set at 1093°C (2000°C), the bond coat/top coat interface was set at 943°C (1730°F), the bond coat/top coat interface was set at 941°C (1725°F), and the inner wall of the tube was set at 927°C (1700°F). The stress profiles obtained were plotted (Figures D-6 through D-9) and compared with the results present when the system was at 21°C (70°F). Interestingly, the largest effective stress was found to be in the ceramic near the bond coat/top coat interface, which is the typical failure location for thermal barrier coatings. Comparison of the results of deformation behavior for the two temperature conditions (Figures D-2 through D-9) indicate how the presence of thermal gradients can affect the stress state present in TBCs.

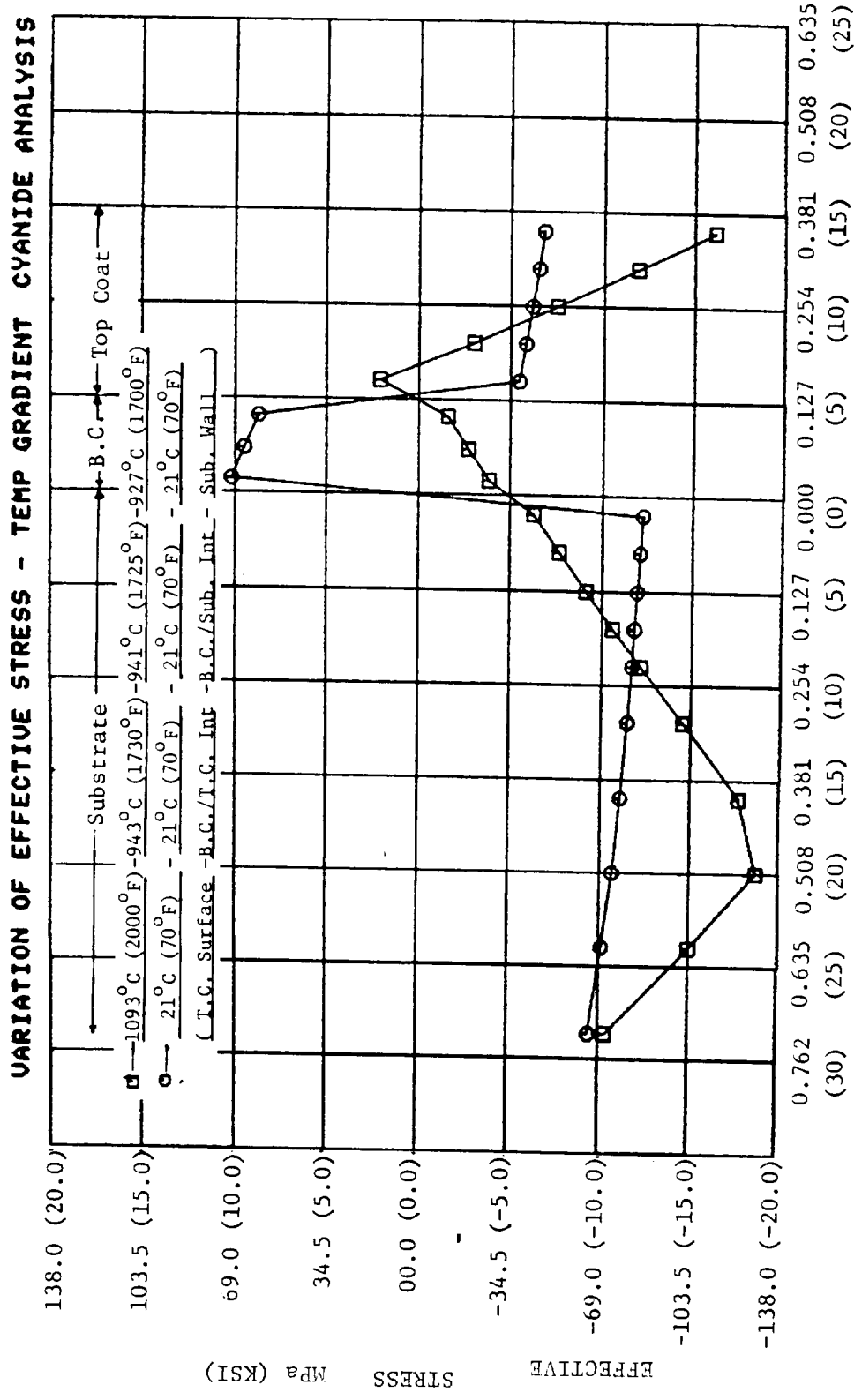

Figure D-6. Plot of Effective Stress Versus Distance in the Substrate, Bond Coat, and Top Coat in the Radial Directions, CYANIDE Analysis for Task B (Temperature Gradient).

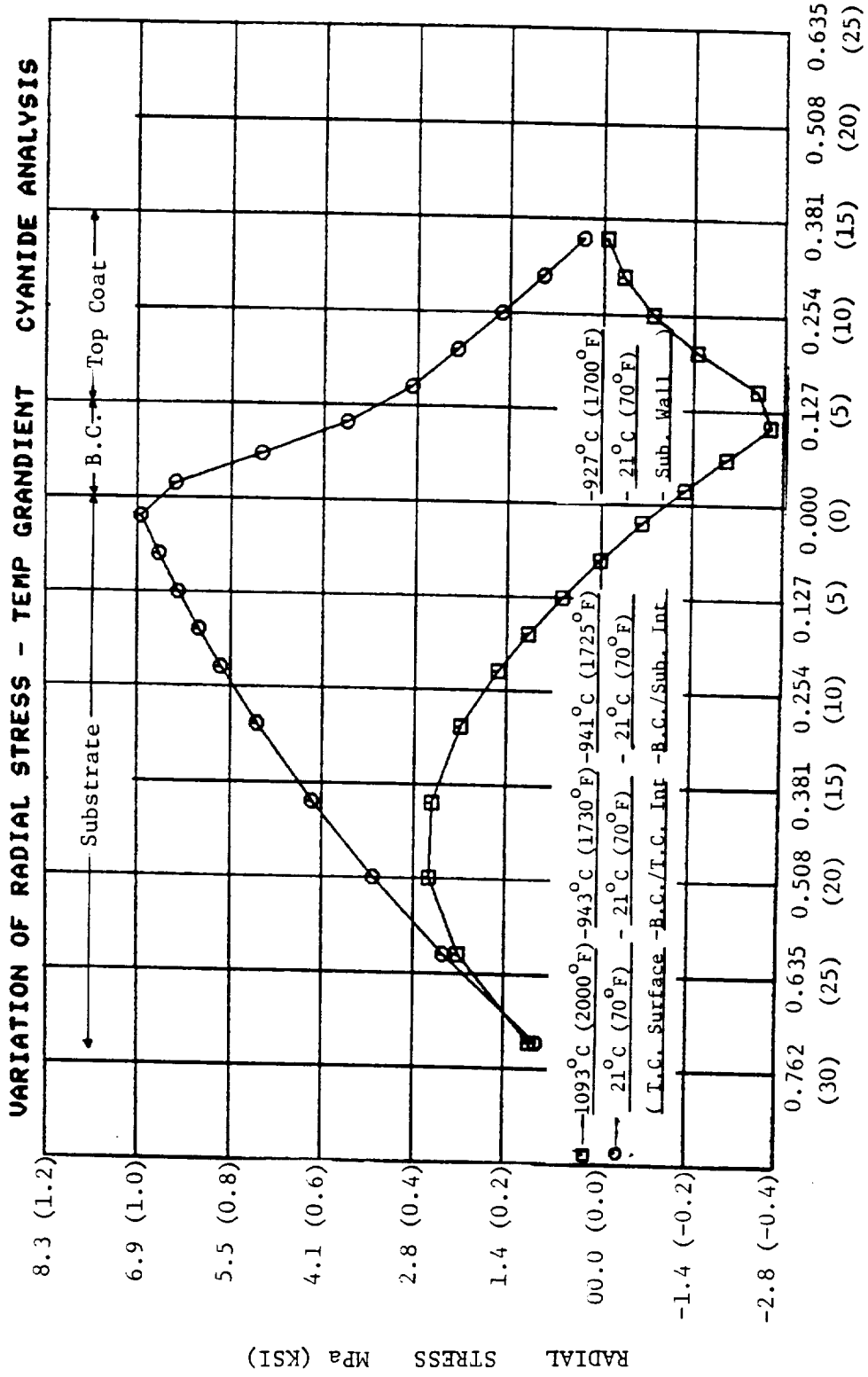

Figure D-7. Plot of Radial Stress Versus Distance in the Substrate, Bond Coat, and Top Coat in the Radial Directions, CYANIDE Analysis for Task B (Temperature Gradient).

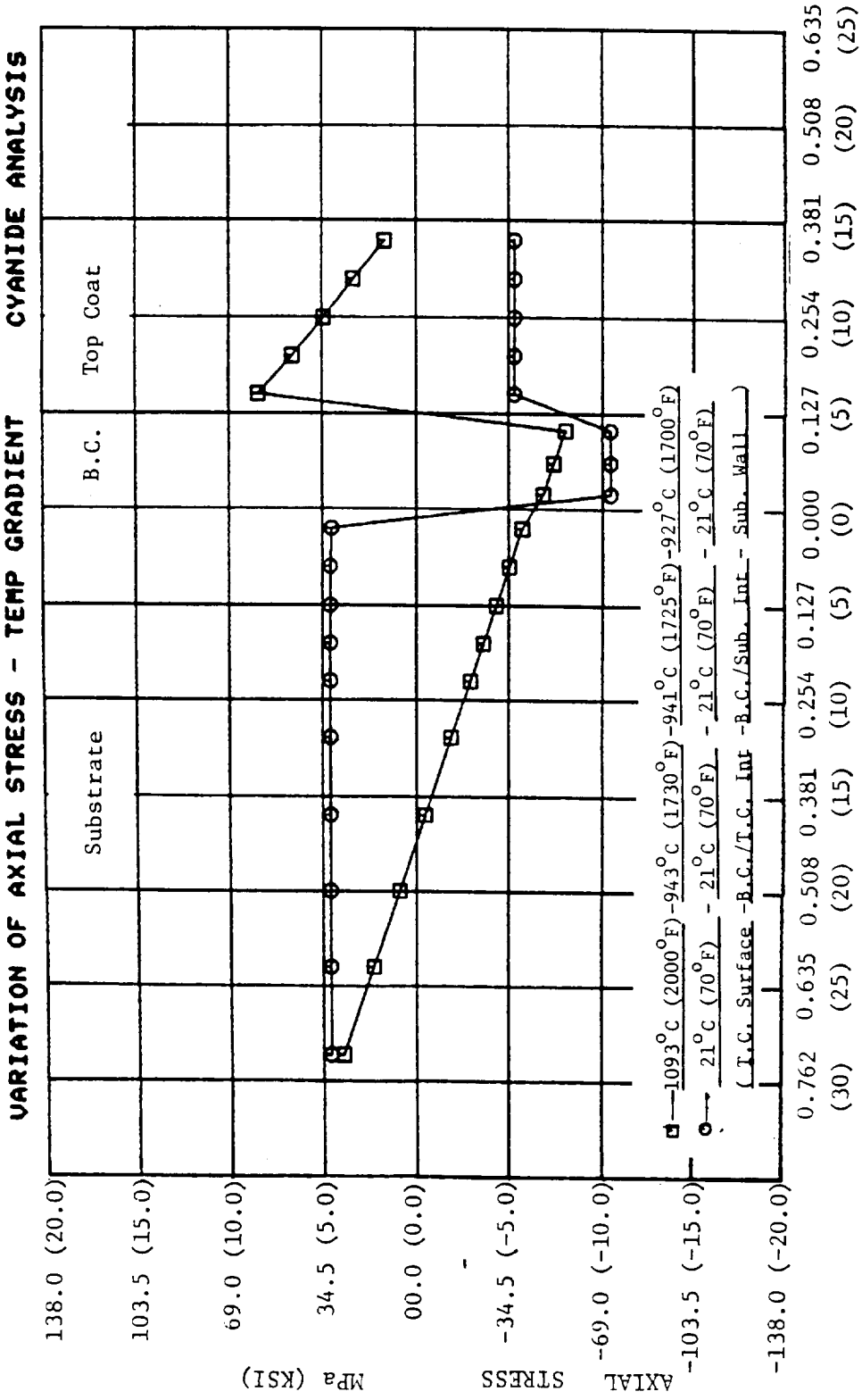

Figure D-8. Plot of Axial Stress Versus Distance in the Substrate, Bond Coat, and Top Coat in the Radial Directions, CYANIDE Analysis for Task B (Temperature Gradient).

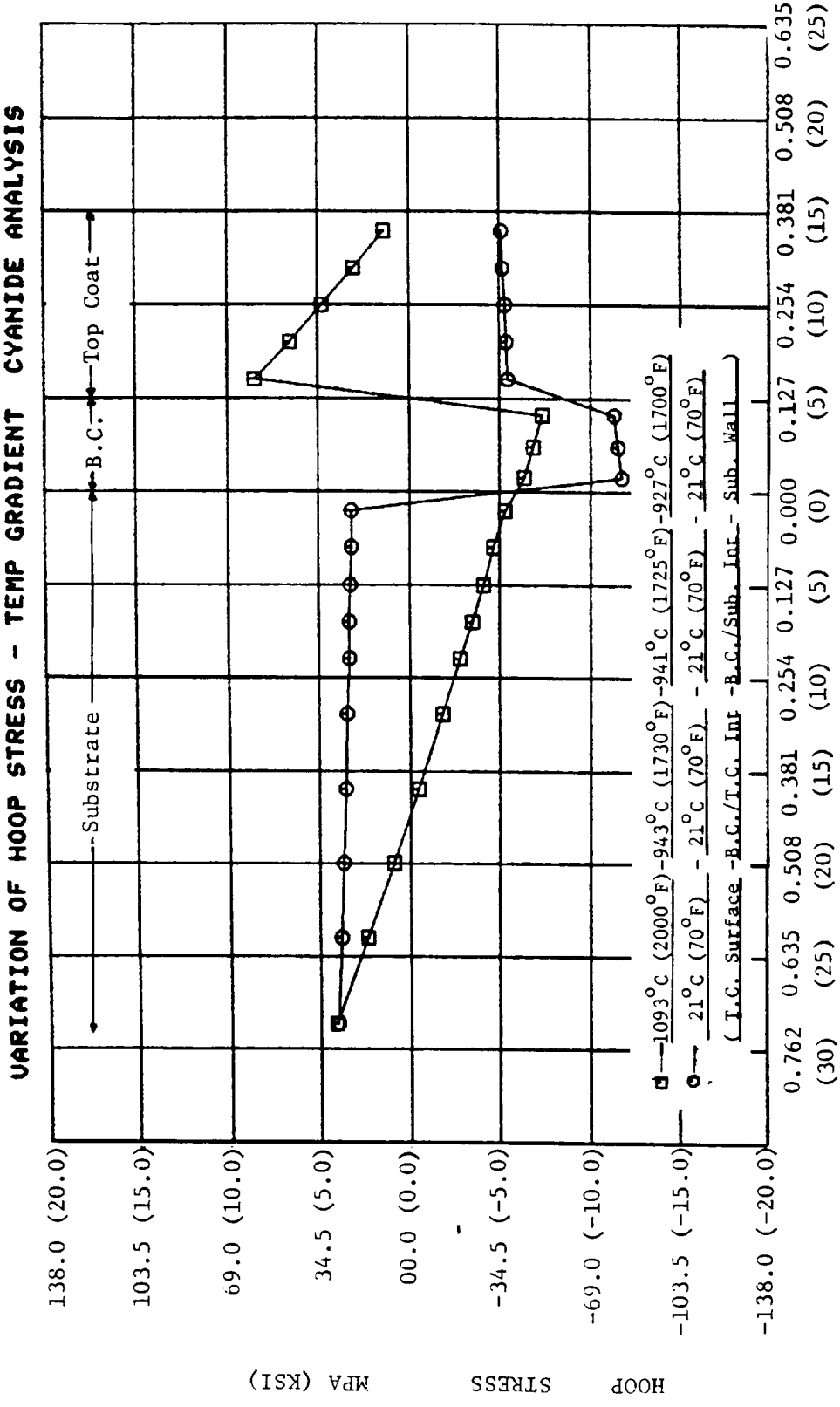

Figure D-9. Plot of Hoop Stress Versus Distance in the Substrate, Bond Coat, and Top Coat in the Radial Directions, CYANIDE Analysis for Task B (Temperature Gradient).

APPENDIX E - MATERIAL PROPERTIES USED IN CYANIDE PROGRAM

Table E-1. Elastic Modulus of TBC Components.

Temperature °C	(°F)	René 80 GPa (MSI) (Ref. 44)		Ni-22Cr-10Al-0.3Y GPa (MSI) (Ref. 32)		ZrO_2-8Y_2O_3 GPa (MSI) (Ref. 45)		Al_2O_3 GPa (MSI) (Ref. 46)	
21	(70)	208	(30.1)	198	(28.7)	48	(7.0)	393	(57)
204	(400)	198	(28.7)	189	(27.4)	41	(5.9)	393	(57)
427	(800)	186	(27.0)	162	(23.5)	33	(4.8)	386	(56)
538	(1000)	180	(26.1)	151	(22.0)	31	(4.5)	379	(55)
649	(1200)	175	(25.3)	143	(20.7)	28	(4.0)	372	(54)
760	(1400)	166	(24.0)	134	(19.4)	26	(3.8)	365	(53)
871	(1600)	157	(22.8)	129	(18.7)	23	(3.4)	352	(51)
982	(1800)	145	(21.0)	124	(18.0)	21	(3.0)	338	(49)
1093	(2000)	116	(16.8)	119	(17.2)	20	(2.9)	310	(45)
1204	(2200)	86	(12.5)	----		17	(2.5)		

Table E-2. Poisson's Ratio of TBC Components.

Temperature °C	(°F)	René 80 (Ref. 44)	Ni-22Cr-10Al-0.3Y*	ZrO_2-8Y_2O_3 (Ref. 32)	Al_2O_3 (Ref. 46)
21	(70)	0.31	0.31	0.076	0.28
204	(400)	0.32	0.32	0.076	0.28
427	(800)	0.32	0.32	0.076	0.29
538	(1000)	0.33	0.33	0.076	0.29
649	(1200)	0.33	0.33	0.076	0.30
760	(1400)	0.34	0.34	0.076	0.32
871	(1600)	0.34	0.34	0.076	0.34
982	(1800)	0.35	0.35	0.076	0.36
1093	(2000)	0.37	0.37	0.076	0.40
1204	(2200)	0.39	0.39	0.076	

*Assumed identical to René 80 for initial studies.

Table E-3. Coefficient of Thermal Expansion (x 10^6).

Temperature °C	(°F)	René 80 in/in/°C (Ref. 44)	Ni-22Cr-10Al-0.3Y in/in/°C (Ref. 32)	ZrO_2-8Y_2O_3 in/in/°C (Ref. 45)	Al_2O_3 in/in°C (Ref. 46)
21	(70)	12.4	11.1	7.6	6.9
204	(400)	12.7	11.7	8.5	7.1
427	(800)	13.1	12.8	9.4	7.4
538	(1000)	13.4	13.3	9.9	7.7
649	(1200)	13.6	13.6	10.3	8.0
760	(1400)	14.3	14.0	10.9	8.2
871	(1600)	15.0	14.8	11.2	8.5
982	(1800)	16.0	15.6	11.7	8.7
1093	(2000)	17.2	16.7	12.2	9.1
1204	(2200)	18.4	----	12.6	

APPENDIX F - CALCULATED STRESS AND CREEP STRAIN CURVES

Figures F-1 through F-8 show the calculated stresses and creep strains in the top coat at the top coat/bond coat interface of thermal barrier coated tubular and button specimens during the thermal cycle shown in Figure 32. Calculated values were obtained using the CYANIDE finite element program described in Section 4.1 and Appendix C of this report.

One interesting feature of the analysis is shown in Figures F-1 and F-3 and demonstrated the asymmetry of the creep generated in the top coat during the thermal cycle. Note that the increment in stress upon heat-up is less than the decrement during the cool down phase. A careful examination of Figure F-3 shows that there is a small but measurable amount of creep generated during the heating but very little creep during cooling. This results from higher stress during heat-up and also from more primary creep. The increased creep lowers the maximum stress and leads to greater unloading during the cool down part of the cycle.

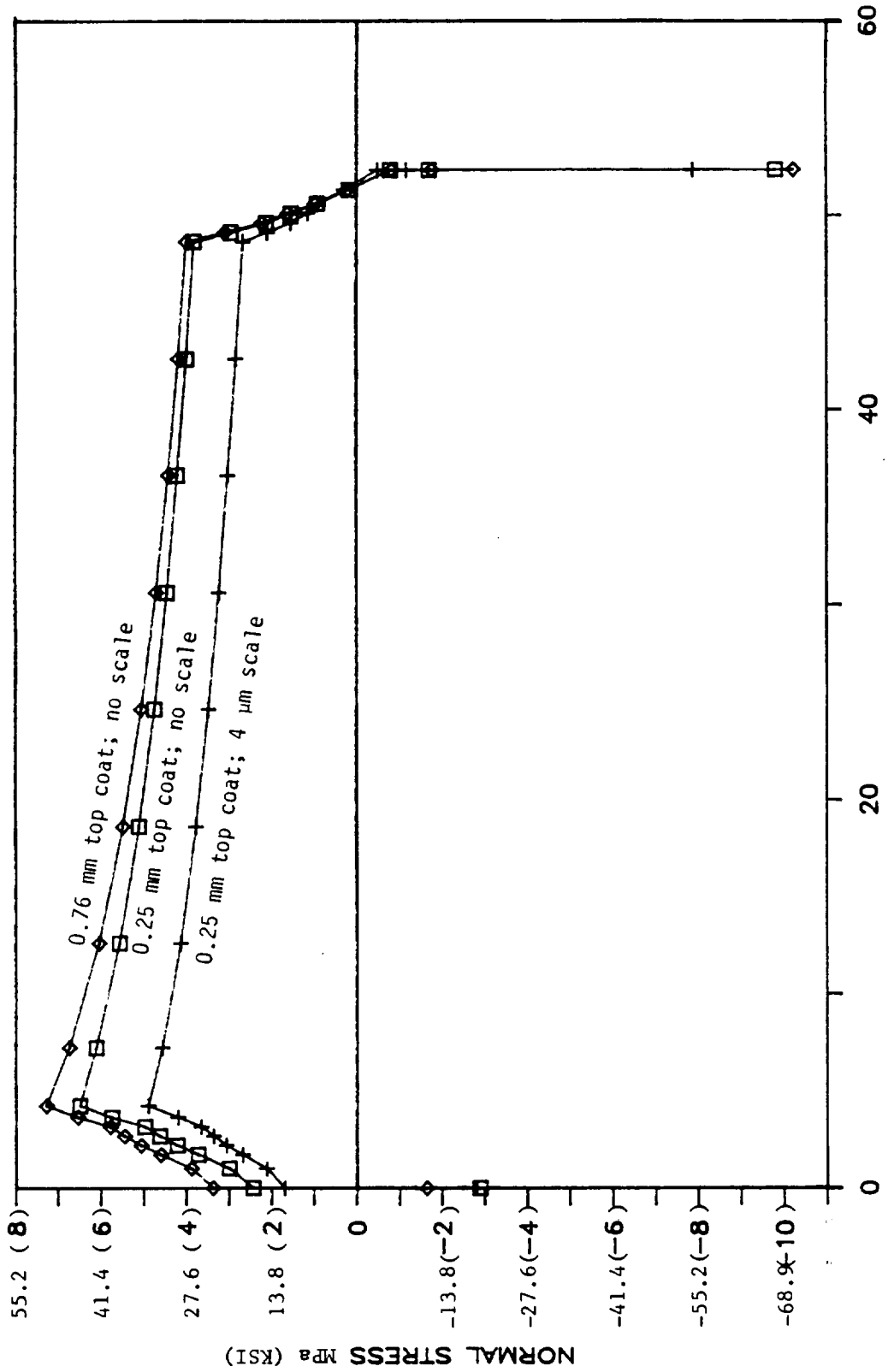

Figure F-1. Calculated Normal Stress in Top Coat at Top Coat/Bond Coat Interface of Thermal Barrier Coated Tubular Specimen. Bond Coat Thickness 0.13 mm.

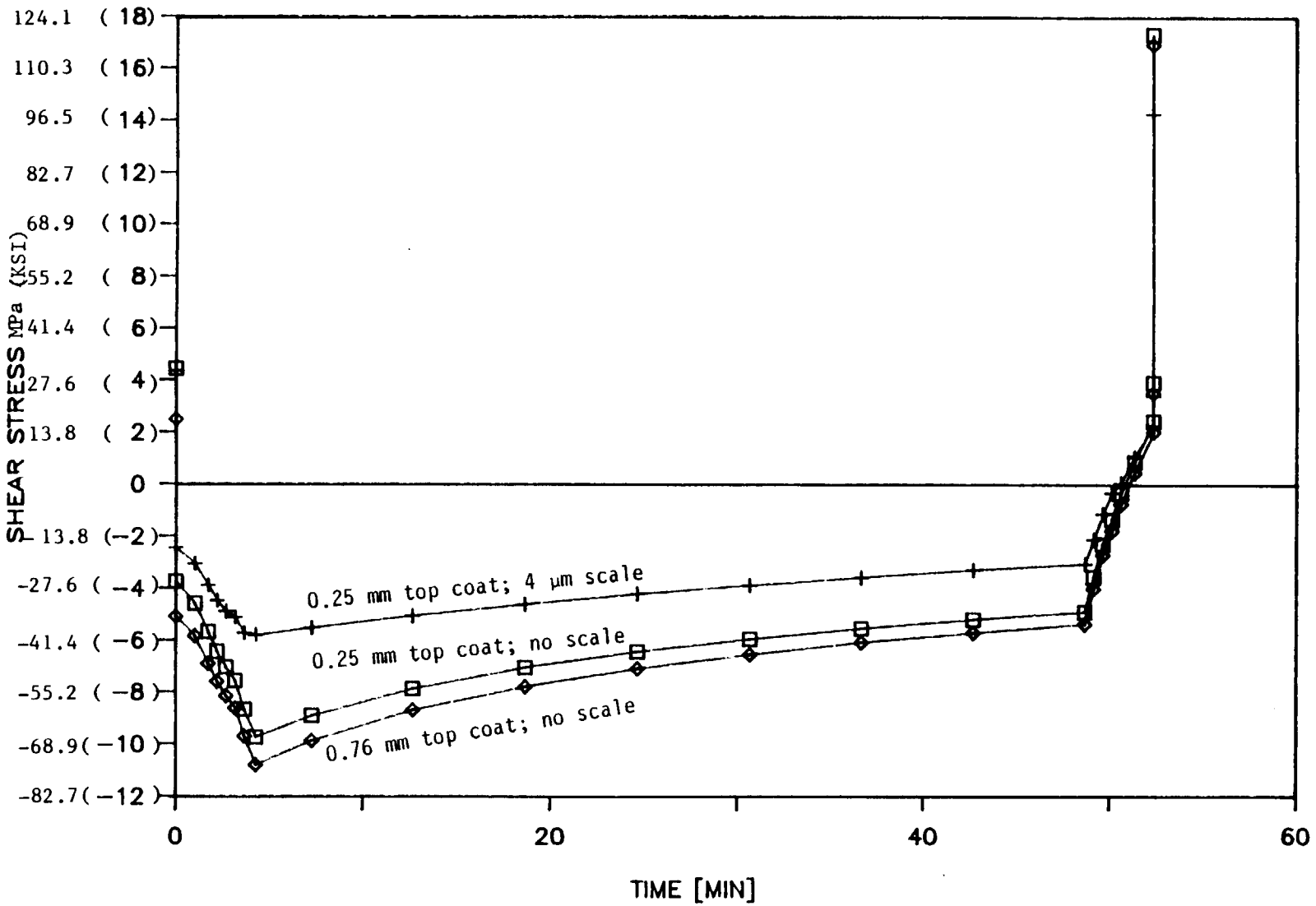

Figure F-2. Calculated Shear Stress in Top Coat at Top Coat/Bond Coat Interface of Thermal Barrier Coated Tubular Specimen. Bond Coat Thickness 0.13 mm.

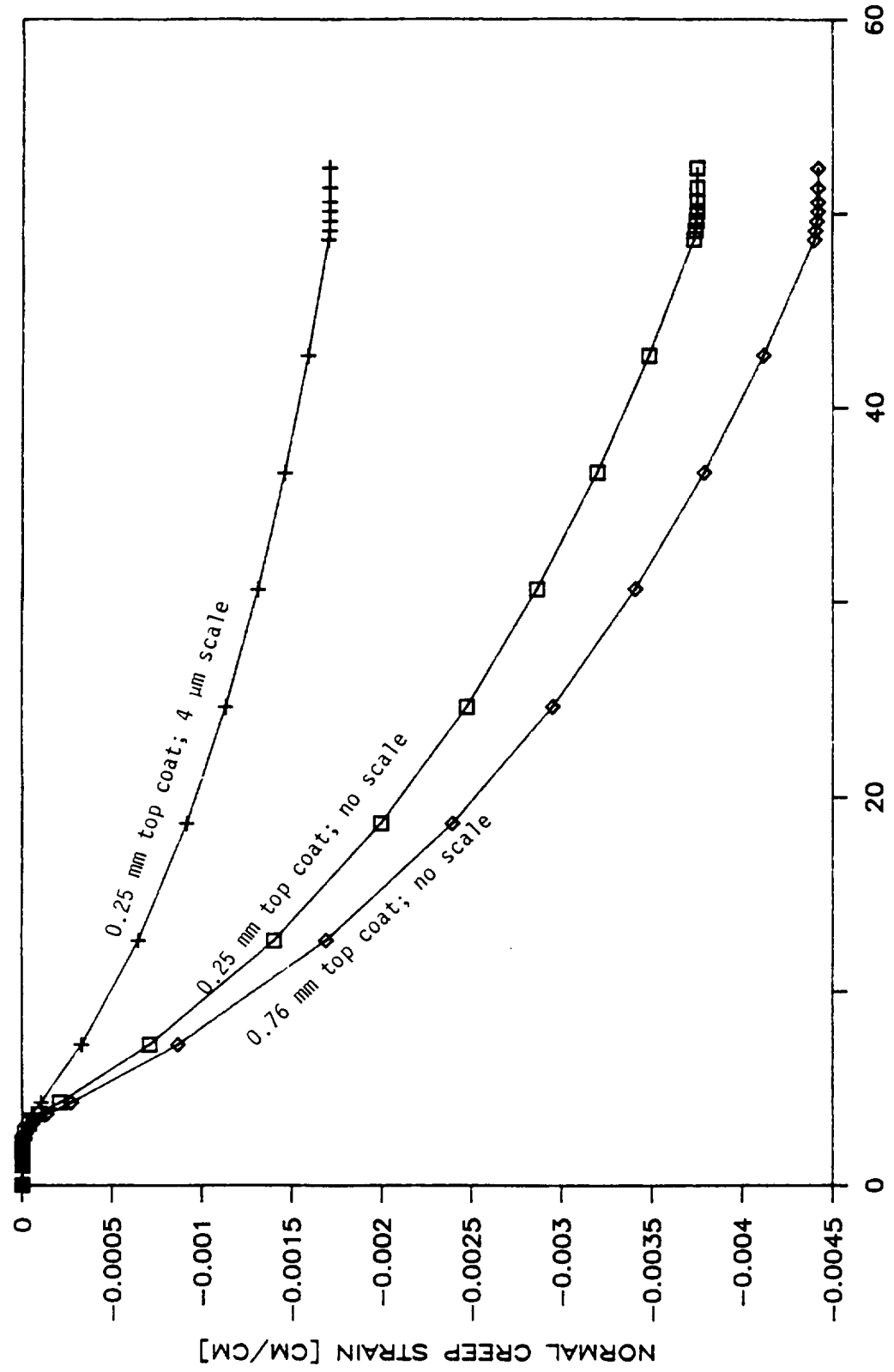

Figure F-3. Calculated Normal Creep Strain in Top Coat at Top Coat/Bond Coat Interface of Thermal Barrier Coated Tubular Specimen. Bond Coat Thickness 0.13 mm.

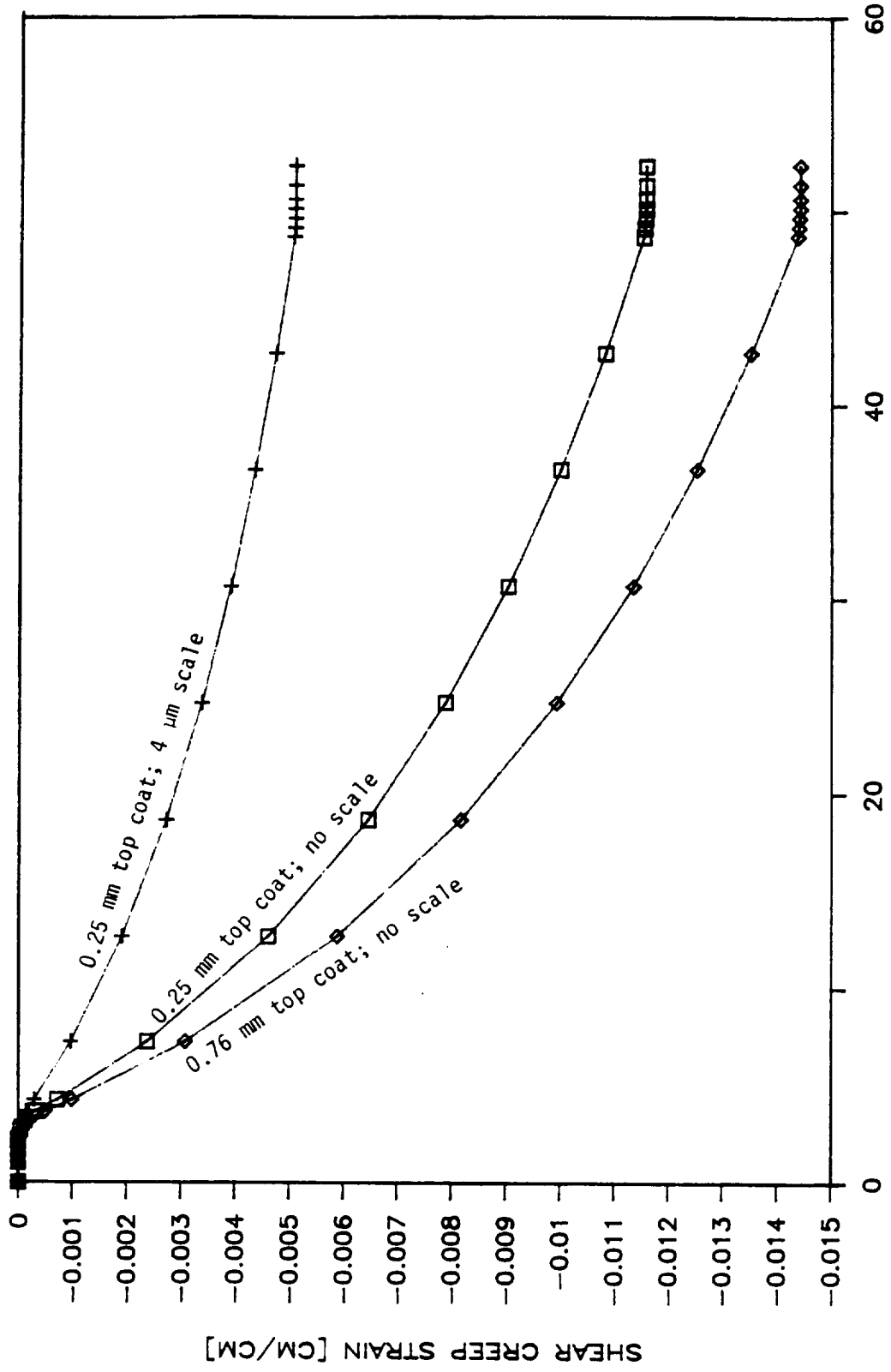

Figure F-4. Calculated Shear Creep Strain in Top Coat at Top Coat/Bond Coat Interface of Thermal Barrier Coated Tubular Specimen. Bond Coat Thickness 0.13 mm.

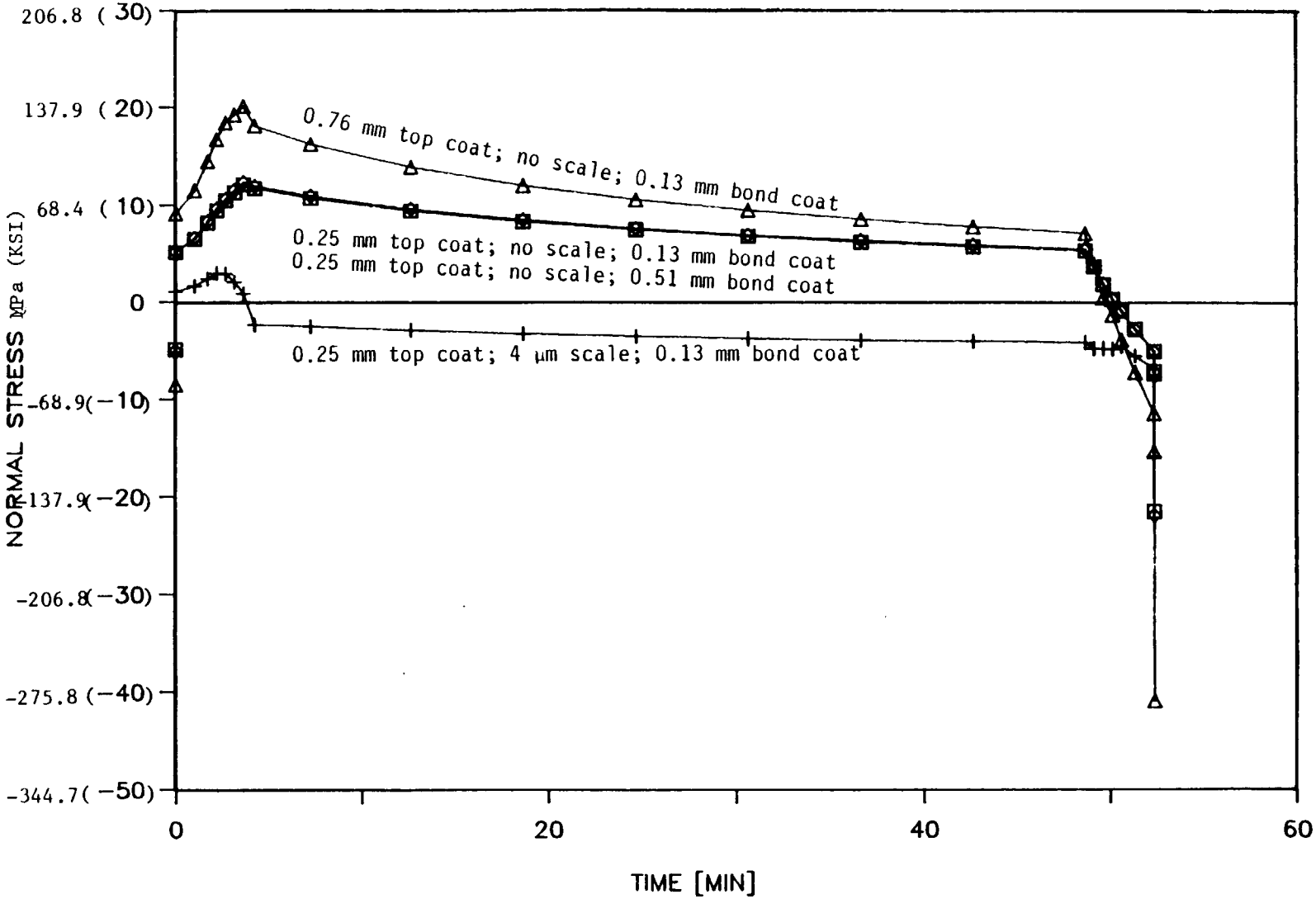

Figure F-5. Calculated Normal Stress in Top Coat at Top Coat/Bond Coat Interface of Thermal Barrier Coated Button Specimen.

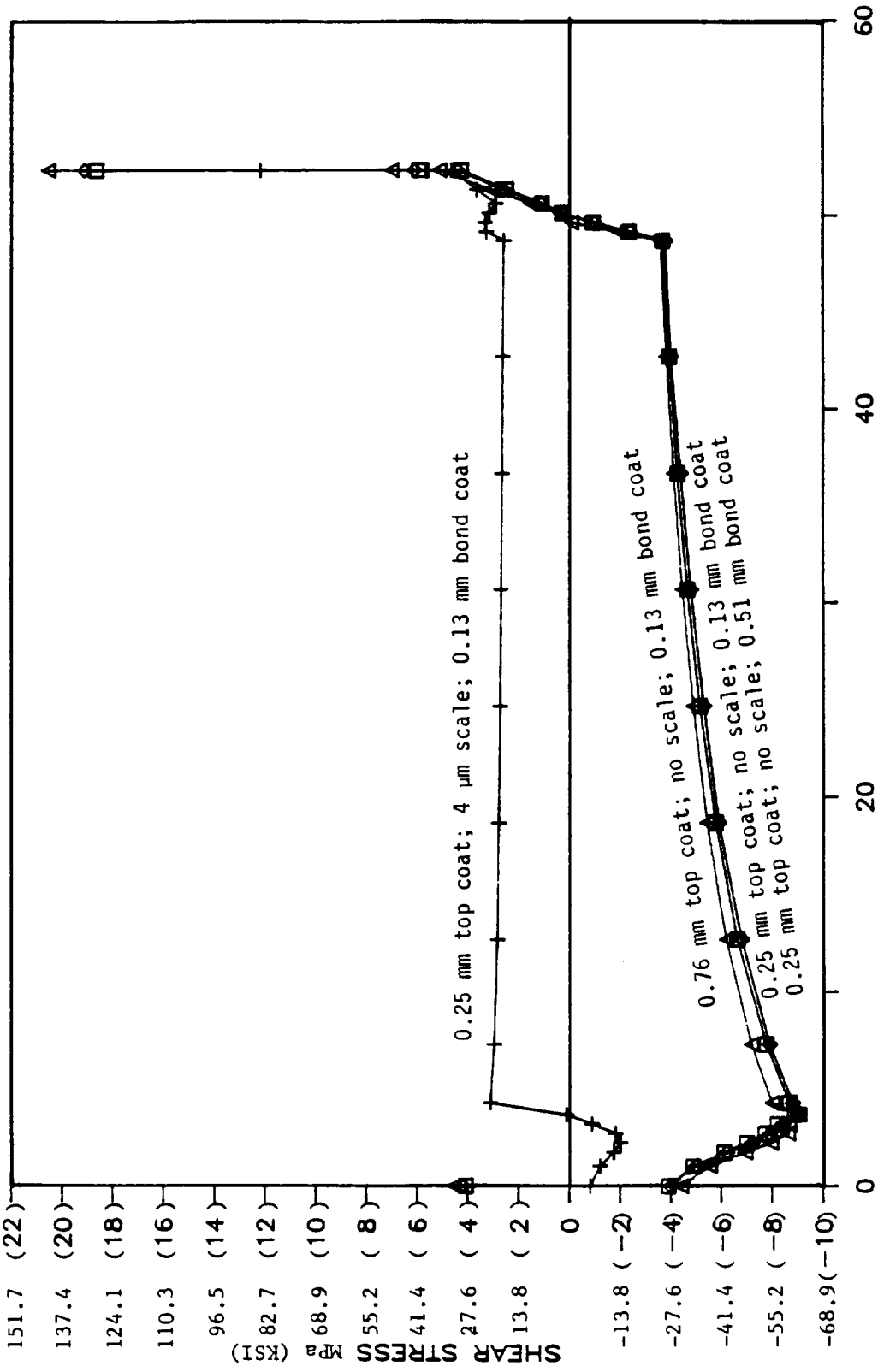

Figure F-6. Calculated Shear Stress in Top Coat at Top Coat/Bond Coat Interface of Thermal Barrier Coated Button Specimen.

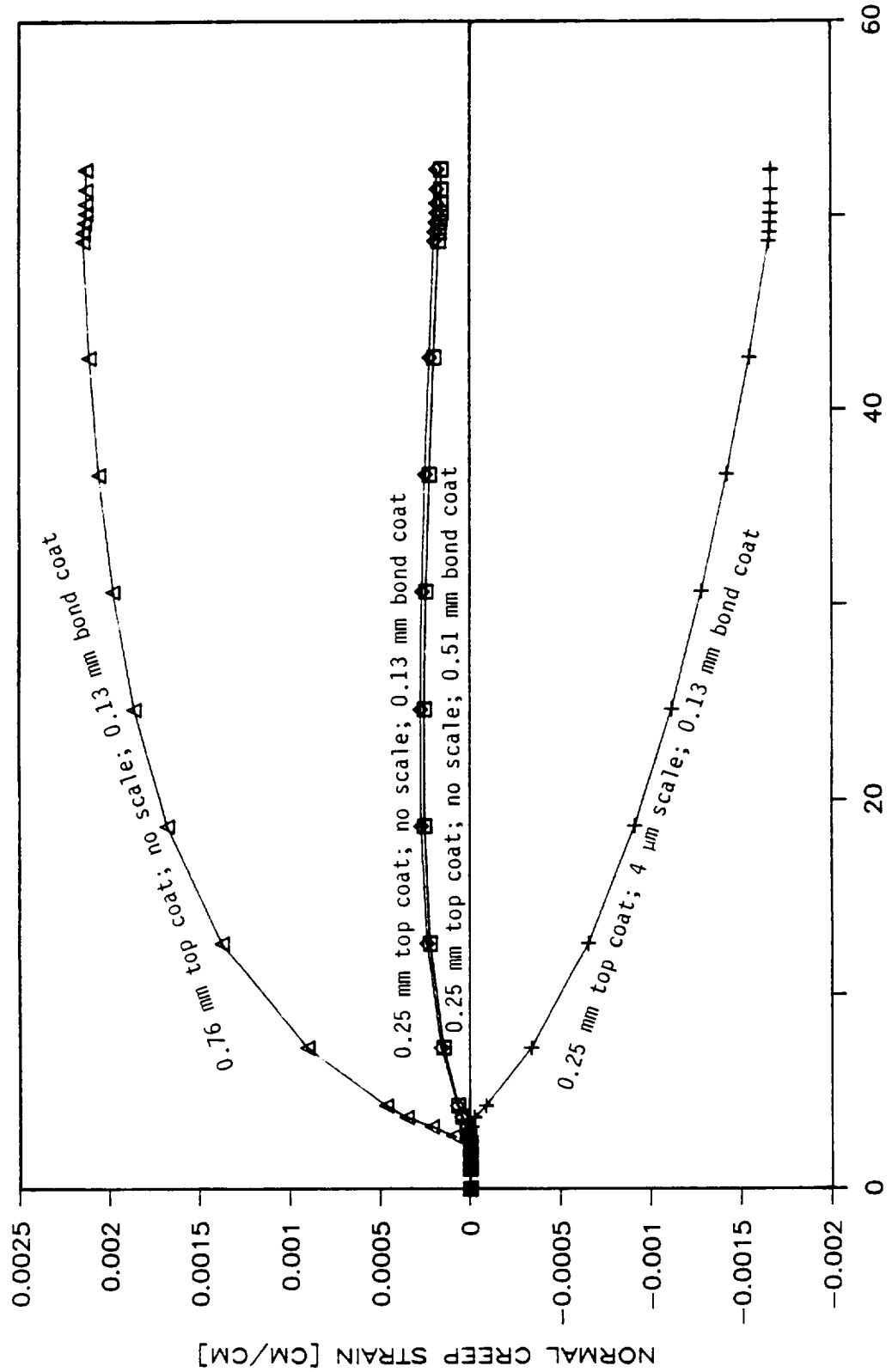

Figure F-7. Calculated Normal Creep Strain in Top Coat at Top Coat/Bond Coat Interface of Thermal Barrier Coated Button Specimen.

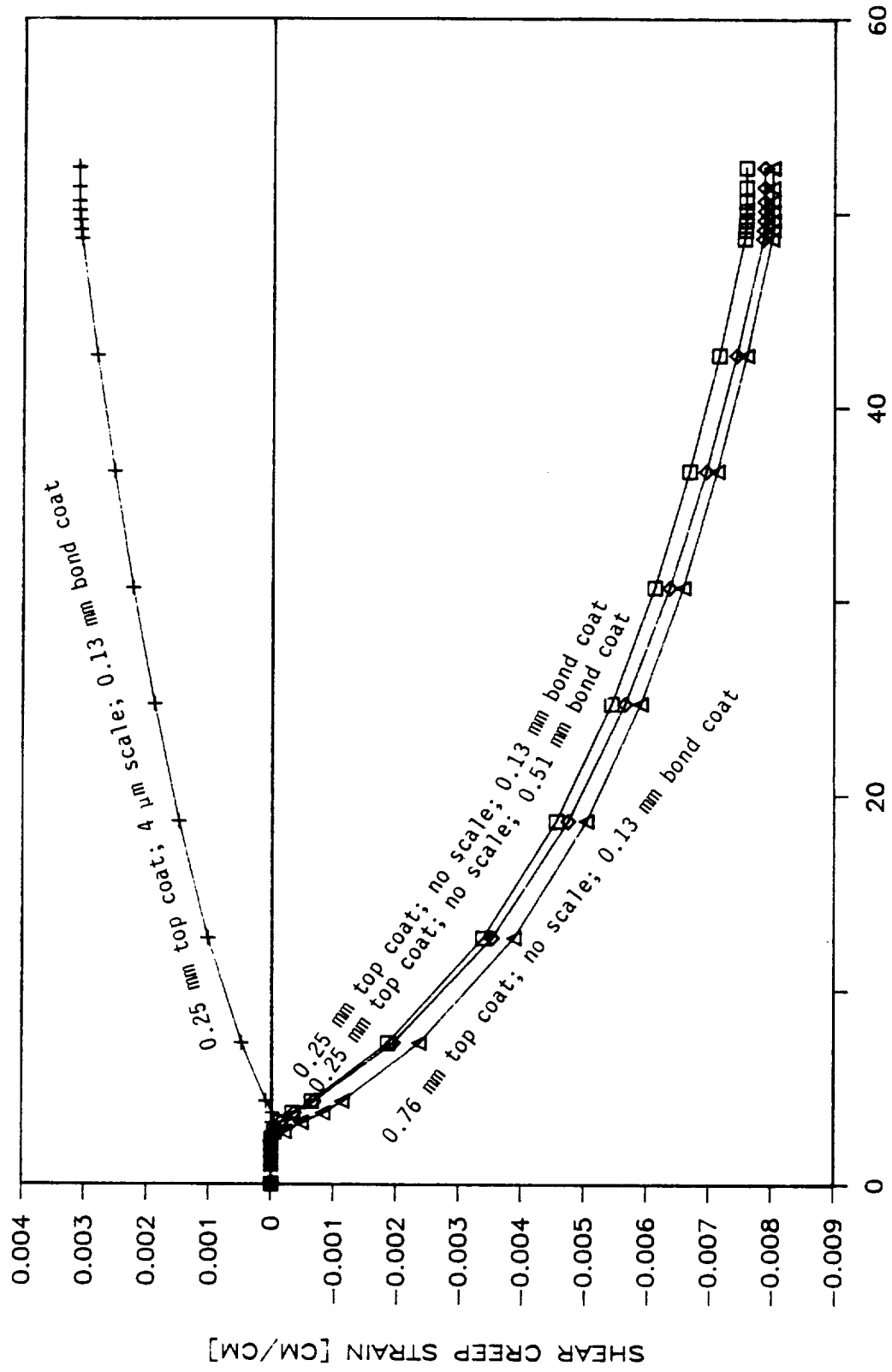

Figure F-8. Calculated Shear Creep Strain in Top Coat at Top Coat/Bond Coat Interface of Thermal Barrier Coated Button Specimen.

APPENDIX G - STRESS-FREE REFERENCE TEMPERATURE

The concept of the stress-free reference temperature provides a convenient and economical approach for incorporating the effects of processing history. This approach will be briefly reviewed and illustrated with an example.

The stress-free reference temperature is computed by

$$\Delta T_{NR} = T_{NR} - T_R = \frac{\alpha_c - \alpha_s}{\alpha_{NR}} (T_{SF} - T_R) \qquad \text{(G-1)}$$

where

T_{NR} = Stress-free reference temperature
T_R = Reference temperature, 70°F
T_{SF} = Stress-free temperature
α_c = Thermal expansion coefficient of the coating at T_{SF}
α_s = Thermal expansion coefficient of the substrate at T_{SF}
α_{NR} = Thermal expansion coefficient of the coating at T_{NR}

The stress-free temperature, T_{SF}, may be determined according to the coating process. Consider a simple process in which the base metal is heated up to some temperature, then the molten coating material is applied on to the base metal, and then it is cooled down to room temperature. In this case the stress-free temperature is the temperature of the base metal at which the coating material is applied. If the coating process ends with an annealing process which removes the residual stresses totally, then the stress-free temperature will be the annealing temperature.

The above equation contains two unknowns, T_{NR} and α_{NR}, but the thermal expansion is a known function of temperature; in most cases linear interpolation can be used. In general, the interpolation can be written

$$\frac{\alpha_T - \alpha_{TR}}{T - T_R} = \frac{\alpha_{NR} - \alpha_{TR}}{T_{NR} - T_R} \qquad \text{(G-2)}$$

where T is some other temperature, α_T is the thermal coefficient of expansion at that temperature, α_{TR} is the thermal coefficient of expansion at the reference temperature, and the other quantities are defined above.

For a simple case of a coating and a substrate, the coating is applied at 982°C so that is the stress free temperature and the reference temperature is taken as 21°C. The coefficents are

α_c (982°C) $= 15.66 \times 10^{-6}$ m/m/C

α_s (982°C) $= 16.04 \times 10^{-6}$ m/m/C

and substituting into equation (G-1)

$$\Delta T_{NR}\, \alpha_{NR} = -365.18 \times 10^{-6} \qquad \text{(G-3)}$$

The additional data required is:

$T_R = 21°C$, $\alpha_{TR} = 11.16 \times 10^{-6}$ m/m/C

$T = 204°C$, $\alpha_T = 11.79 \times 10^{-6}$ m/m/C

Substituting into equation (G-2)

$$\alpha_{NR} = 0.00344 \times 10^{-6}\, \Delta T_{NR} + 11.16 \times 10^{-6}$$

and then into (G-3),

$$0.00344\, \Delta T_{NR}^2 + 11.16\, \Delta T_{NR} + 365.18 = 0$$

Solving and selecting the appropriate root leads to $T_{NR} = -12.4°C$

When a third coating is added, the constraint of the bond coat must be taken into account when calculating the stress-free reference temperature of the top coat. This is done by matching the thermal expansion of the top and bond coat at the interface at the top coat application (stress-free, T_{SFT}) temperature. If U is the thermal expansion of the bond coat at T_{SFT}, then

$$U = \alpha_{CT}\,(T_{SFT} - T_R) - \alpha_{NRT}\,(T_{NRT} - T_R)$$

where the subscript T refers to the top coat.

The procedure is identical to the previous exercise with the interpolation relation (G-2) supplying the second expression for T_{NR2} and α_{NR2}. Substituting the properties of the top coat and the expansion of the bond coat leads to

$$T_{NR2} = -218.6°C$$

REFERENCES

1. Busch R., "Develop Sputter Deposited, Graded Metal ZrO_2 Coating Technology for Application to Turbine Hot Section Components," Naval Sea System Command, Contract N00024-75-C-4333, 1976.

2. Duderstadt, E.C. and Agarwal, P., "Energy Efficient Engine - High Pressure Turbine Thermal Barrier Coating Support Technology Report," General Electric Company, Aircraft Engine Business Group, R82AEB293, NASA CR-168037, 1982.

3. Stecura, S. "Effects of Yttrium, Aluminum, and Chromium Concentrations in Bond Coatings on the Performance of Zirconia - Yttria Thermal Barriers," NASA TM-79206, 1979.

4. Gedwill, M.A., "Improved Bond Coatings for Use with Thermal Barrier Coatings," NASA TM-81567, 1980.

5. Miller, R.A. and Lowell, C.E., "Failure Mechanisms of Thermal Barrier Coatings Exposed to Elevated Temperatures", NASA TM-82905, 1982.

6. Miller, R.A. and Berndt, C.C., "Performance of Thermal Barrier Coatings in High Heat Flux Environments," NASA TM-83663, 1984.

7. 1982 Independent Research and Development Technical Plan, General Electric Company, Aircraft Engine Business Group, R82AEB244, Vol. V, 1982.

8. Stecura, S., "Optimization of the NiCrAlY/ZrO_2-Y_2O_3 Thermal Barrier System," NASA TM-86905, 1985.

9. Miller, R.A., "Oxidation Behavior of a Thermal Barrier Coating," Proceeding on High Temperature Protective Coating, edited by S.C. Singhal, Presented at 112th AIME Annual Meeting, Atlanta, Georgia, March 7-8, 1983.

10. Miller, R.A., Agarwal, P., and Duderstadt, E.C., "Life Modelling of Atmospheric and Low Pressure Plasma Sprayed Thermal Barrier Coatings," Presented at 1984 American Ceramic Society Meeting , Cocoa Beach, Florida, 1984.

11. Miller, R.A., "Oxidation - Based Model for Thermal Barrier Coating Life," Ceramic Journal, p. 83, August, 1984.

12. 1984 Independent Research and Development Technical Plan, General Electric Company, Aircraft Engine Business Group, R84AEB454, Project 10.18, 1984.

13. Valentine, P.G. and Maier, R.D., "Microstructure and Mechanical Properties of Bulk and Plasma - Sprayed Y_2O_3 - Partially Stabilized Zirconia", NASA CR-165126, 1980.

14. Gill, B.J., "Plasma deposited MCrAlY and thermal barrier coatings for gas turbine components," Presented at First Conference On Material Engineering, ME, 10-12 July 1984.

15. Stecura, S. "Effects of Compositional Changes On The Performance Of A Thermal Barrier Coating System," NASA TM 78976, 1979.

16. Miller, R.A., Garlick, R.G., and Smialek, J.L., "Phase Distributions in Plasma Sprayed Zirconia - Yttria," American Ceramic Society Bulletin, V.62, p. 1355-1358, Dec., 1983.

17. Agarwal, P., GE-AEBG, unpublished data, 1983.

18. Anderson, C.A. and Gupta, T.K., "Phase Stability and Transformation Toughening in Zirconia", Science And Technology Of Zirconia, Advances In Ceramics, Vol.3, edited by Heuer, A.H. and Hobbs, L.W. , American Ceramics Society, p. 184, 1981.

19. Evans, A..G., "Toughening Mechanisms in Zirconia Alloys," Science And Technology Of Zirconia II, Advances In Ceramics, Vol. 12, edited Heuer, A.G., Claussen, N., and Ruhle, M., American Ceramic Society, p. 193, 1984.

20. Valentine, P.G. , Maier, R.D., and Mitchell, T.E., "Microstructure and Mechanical Properties of Bulk Yttria - Partially - Stabilized Zirconia", NASA CR-165402, 1981.

21. Mantkowski, T.E., Rigney, D.V., Froning, M.J., and Jayaraman, N., "Characterization of ZrO_2 - Y_2O_3 Thermal Spray Powder Systems," Presented at NASA Thermal Barrier Coating Workshop, May 21, 22 1985, Cleveland, Ohio.

22. Hendricks, R.C., and McDonald, G., "Effects of Arc Current on the Life in Burner-Rig Thermal Cycling of Plasma - Sprayed ZrO_2 - Y_2O_3", Ceramic Engineering Society Proceeding, Vol. 3, 1982.

23. Rangaswamy, S., and Herman, H., "Thermal Expansion Study of Plasma - Sprayed Oxide Coatings", Thin Solid Films, Vol. 73, p.43-52, 1980.

24. Cassenti, B.M., Brickley, A.M., and Sinko, G.C., "Thermal and Stress Analysis of Thermal Barrier Coatings", AIAA/SAE/ASME 17th Joint Propulsion Conference, 1981, Colorado Springs Co., AIAA-81-1482.

25. Shankar, N.R., Berndt, C.C., Herman, H., and Rangaswamy, S., "Acoustic Emission from Thermally Cycled Plasma-Sprayed Oxides", American Society Bulletin, Vo.62, No.5, May 1983.

26. Becher, P.F., Rice, R.W., Wu, C.C., and Jones, R.L., "Factors In The Degradation Of Ceramic Coatings For Turbine Alloys", Thin Solid Films, Vol. 53, p. 225-232, 1978.

27. McDonald, G. and Hendricks, R.C., "Effect Of Thermal Cycling On ZrO_2-Y_2O_3 Thermal Barrier Coatings", NASA TM-81480, 1980.

28. Bill, R.C., "A Sputtered Zirconia Primer for Improved Thermal Shock Resistance", NASA TM-81732, 1981.

29. Mullen, R.L., McDonald, G., Hendricks, R.C., and Hofle, M.M., "Correlation of Compressive Stress with Spalling of Plasma Sprayed Ceramic Materials", NASA TM-83406, 1983.

30. Watson, J.W., and Levine, S.R., "Deposition Stress Effects on Thermal Barrier Coating Burner Rig Life", NASA TM 83670, 1984.

31. 1983 Independent Research and Development Technical Plan, General Electric Company, Aircraft Engine Business Group, R83AEB263, Vol. V, 1983.

32. Siemers, P.A. and Hillig, W.B., "Thermal Barrier Coated Turbine Blade Study", NASA CR-165351, 1981.

33. Palko, J.E., Luthra, K.L., and McKee, D.W., "Evaluation of Performance of Thermal Barrier Coatings Under Simulated Industrial/Utility Gas Turbine Conditions", Final Report D.O.E., Contract NO. EC-77-C-05-5402, 1978.

34. Zaplatynsky, I., "Reactions of Yttria-Stabilized Zirconia With Oxides and Sulfates of Various Elements", NASA TM-78942, 1978.

35. Miller, R.A., "High Temperature Protective Coatings," S.C. Singhal, Editor, AIME, 1982.

36. Saegusa, F., "Failure Mechanism Studies on Thermal Barrier Coatings," GE TM 86-AMD-004, February, 1986.

37. Duderstadt, E.C., Pilsner, B.H., Torgesen, M., Groves, M.T., Nelson, W.A., and Butts, W.R., "Thermal Barrier Coating Technology," GE TM 86-348, 1986.

38. Spinner, S. and Tefft, W.E., ASTM Proc. 61, page 1221 - 1238 (1961).

39. DeMasi, J.T., and Sheffler, K.D., "Thermal Barrier Coating Life Prediction Model Development", Second Annual Report, NASA CR-179508, April, 1986.

40. Hebsur, M.G., and Miner, R.V., "High-Temperature Tensile and Creep Behavior of Low-Pressure Plasma-Sprayed NiCoCrAlY Coating Alloy," Journal of Materials Science and Engineering, Vol. 83, 1986.

41. Firestone, R. F., Logan, W. R., and Adams, J. W., "Creep of Plasma Sprayed Zirconia," NASA CR-167868, November, 1982.

42. Marin, J., Pao, Y.H., and Cuff, G., "Creep Properties of Lucite and Plexiglass for Tension, Compression, Bending, and Torsion," Trans. ASME, 1975.

43. Pugh, C.E., "Constitutive Equations for Creep Analysis of Liquid Moderated Fast Breeder Reactor (LMFBR) Components," Advances in Design for Elevated Temperature Environment, S.Y. Zamrik and N.I. Jetter, Eds., ASME, 1975.

44. McKnight, R.L., Laflen, J.H. and Spamer, G.T., "Turbine Blade Tip Durability Analysis," NASA CR-165268, 1982.

45. Andress, D.E., "Analytical Study of Thermal Barrier Coated First Stage Blades in F100 Engines," NASA CR-135359, 1978.

46. Lynch, J.F., Ruderer, C.G., and Duckworth, W.H., "Engineering Properties of Ceramics," AFML-TR-66-52, 1966.

D. L. Alger
NASA Lewis Research Center
21000 Brookpark Road M/S 301-2
Cleveland, OH 44135

L. F. Aprigliano
D.W. Taylor Naval Ship R&D Ctr
Annapolis, MD 21402

M. M. Bailey
NASA Lewis Research Center
21000 Brookpark Road (77-6)
Cleveland, OH 44135

Michael Bak
Williams International
P. O. Box 200 (5-16)
Walled Lake, MI 48088

Dr. Richard Barkalow
Government Product Division
Pratt & Whitney Aircraft
West Palm Beach, FL 33042

H. Beale
Applied Coatings, Inc.
775 Kaderly Drive
Columbus, OH 43228

Robert Beck
Teledyne - CAE
1330 Laskey Road
Toledo, OH 43612

E. J. Beltran
Materials & Process Tech. Lab.
General Electric Company
1000 Western Avenue
Lynn, MA 01905

Biliyar N. Bhat
NASA Marshall Space Flight Cen
ter
Huntsville, AL 35812

Stephen W. Blakely
Director - Market Analysis
The Unimar Group, Ltd.
513-515 Williams Street
Alton, IL 62002

N. Bornstein
High Temp. Materials Research
United Aircraft Research Lab.
400 Main Street
East Hartford, CT 06108

David Bott
Muscle Shoals Mineral Company
1202 East 2nd Street
Muscle Shoals, AL 35661

R. J. Bratton
Westinghouse Electric R&D
1310 Beulah Road
Pittsburgh, PA 15235

Walter Bryzik
U.S. Army Tank-Auto Command
Diesel Engine Research RMSTA
Warren, MI 48397

R. F. Bunshah
University of California
6532 Boelter Hall
Los Angeles, CA 90024

George C. Chang
Cleveland State University
Cleveland, OH 44115

Ted Chase
Elliot Support Services Div.
of United Technologies Corp.
2001 West Belt Drive North
Houston, TX 77043

Jerry Clifford
U.S. Army Applied Tech. Lab.
SAVDL-ATL-ATP
Fort Eustis, VA 23604

Dave Clingman
Detroit Diesel Allison - GMC
Engineering Operations
Indianapolis, IN 46206

Arthur Cohn
E P R I
3412 Hillview Avenue
Palo Alto, CA 94303

Thomas A. Cruse
Southwest Research Institute
P. O. Box 28510
San Antonio, TX 78284

Prof. Sherman D. Brown
University of Illinois
105 South Goodwin Avenue
Urbana, IL 61801

Dr. Michael A. Decrescente
High Temp. Materials Research
United Aircraft Research
400 Main Street
East Hartford, CT 06108

Mr. William Drawl
270 Materials Research Lab.
Penn State University
University Park, PA 16802

Keith Duframe
Battelle Laboratories
505 King Avenue
Columbus, OH 43216

Mrityunjoy Dutta
U.S. Army AMSAV-EAS
4300 Goodfellow Boulevard
St. Louis, MO 63120

D. S. Engleby
Naval Air Rework Facility
Mail Drop 9, Code 017
Cherry Point, NC 28533

John Fairbanks
Department of Energy
Office of Fossil Energy
Washington, DC 20545

N. Geyer
AFWAL/MLLM
Wright Patterson A.F.B.
Dayton, OH 45433

J. W. Glatz
NAPTC R&D Division
Naval Air Prop. Test Center
Trenton, NJ 08628

G. W. Goward
Coatings Technology Corp.
2 Commercial Street
Branford, CT 06405

Dr. H. C. Graham
Aerospace Research Laboratory
Building 450 (ARZ)
Wright Patterson A.F.B.
OH 45433

Prof. Otto J. Gregory
Dept. of Chemical Engineering
University of Rhode Island
Kingston, RI 02881

D. K. Gupta
Pratt & Whitney Group
400 Main Street
East Hartford, CT 06108

William K. Halman
Temescal
2850 Seventh Street
Berkeley, CA 94710

D. Hanink
Detroit Diesel Allison - GMC
Engineering Operations
Indianapolis, IN 46206

Doug Harris
APS - Materials, Inc.
153 Walbrook
Dayton, OH 45405

Mr. Ralph Hecht
Pratt & Whitney Aircraft
P. O. Box 2691
West Palm Beach, FL 33402

H. Herman
Detroit Diesel Allison - GMC
P. O. Box 894 (W-8)
Indianapolis, IN 46206

Harold Herman
Argonne National Laboratory
9700 South Cass Avenue
Argonne, IL 60439

M. Herman
Dept. of Materials Science
State Univ. of New York
Stonybrook, NY 11794

Frank Hermanek
Alloy Metals, Inc.
501 Executive Drive
Troy, MI 48084

R. V. Hillery
General Electric Company
EMTL
Cincinnati, OH 45215

J. Stan Hilton
University of Dayton
300 College Park
Dayton, OH 45469

Richard R. Holmes
NASA Marshall Space Flight Cen
ter
Huntsville, AL 35812

Lulu Hsu
Solar Turbines, Inc.
2200 Pacific Highway
San Diego, CA 92138

Information Center
Metals & Ceramics
Battelle Columbus Laboratories
505 King Avenue
Columbus, OH 43201

Dr. R. L. Jones
Chemistry Division
Naval Research Laboratory
Code 6170
Washington, DC 20375

Larry A. Junod
Allison Gas Turbine Division
P. O. Box 420, Plant 8-T12
Indianapolis, IN 46206

C. Kortovich
TRW, Inc.
23355 Euclid Avenue
Cleveland, OH 44117

I. Kvernes
Sentralinst. Industriell
Forskning
Blindern, Oslo 3
Forskingyeien 1,
NORWAY

Propulsion Laboratory
U.S. Army Research & Technolog
y Laboratory
21000 Brookpark Road (302-2)
Cleveland, OH 44135

H. C. Larson
Caterpillar, Inc.
Technical Center
Peoria, IL 61629

Sylvester Lee
AFWAL-MLTM
Wright Patterson A.F.B.
Dayton, OH 45433

A. V. Levy
Lawrence Berkeley Laboratory
University of California
Berkeley, CA 94720

Dr. W. W. Liang
Americom, Inc.
8928 Fullbright Avenue
Chatsworth, CA 91311

E. L. Long, Jr.
Oak Ridge National Laboratory
P. O. Box X, Bldg. 4508
Oak Ridge, TN 37831

Frank N. Longo
Metco, Inc.
1101 Prospect Avenue
Westbury, L.I., NY 11590

Dr. Krishan L. Luthra
Research & Development Center
General Electric Company
P. O. Box 8
Schenectady, NY 12301

Richard Martin
Boeing Commercial Airplane Co.
P. O. Box 3707 (9W-61)
Seattle, WA 98124

Prof. Gerald H. Meier
Dept. of Met. & Materials Eng.
University of Pittsburgh
848 Benedum Hall
Pittsburgh, PA 15261

T. E. Mitchell
Los Alamos Research Laboratory
P. O. Box 1663
Los Alamos, NM 87545

Michael L. Moore
Aircraft Propulsion Eng.
Trans World Airlines, Inc.
P. O. Box 20126
Kansas City, MO 64195

S. Naik
AVCO-Lycoming Division
550 South Main Street
Stratford, CT 06497

J. W. Patten
Cummins Engine Company
Box 3005
Columbus, IN 47202

Dr. F. S. Pettit
Department of Met. & Materials
University of Pittsburgh
848 Benedum Hall
Pittsburgh, PA 15261

Dr. B. Pletka
Michigan Technical University
Dept. of Metallurgical Eng.
Houghton, MI 49931

Ronne D. Proch
Corning Glass Works
31501 Solon Road
Solon, OH 44139

R. J. Quentmeyer
NASA Lewis Research Center
21000 Brookpark Road (500-200)
Cleveland, OH 44135

Prof. Robert A. Rapp
Department of Metals Eng.
Ohio State University
116 W. 19th Avenue
Columbus, OH 43210

Dr. Dasara V. Rathnamma
Chemist, Corrosion Branch
Ship Materials Eng. Dept.
D.T. Naval Ship Res. Center
Annapolis, MD 21402

Gopal Revanton
Deer & Company
3300 River Drive
Moline, IN 61265

David Rigney
General Electric Company
Cincinnati, OH 45215

Joseph Scricca
AVCO-Lycoming Division
550 South Main Street
Stratford, CT 06497

Ravi Shankar
Chromalloy R&T
Chromalloy Amer. Corp.
Orangeburg, NY 10962

Keith Sheffler
Pratt & Whitney Group
400 Main Street
East Hartford, CT 06108

T. P. Shyu
Caterpillar Tractor Company
100 N.E. Adams
Peoria, IL 61629

Dr. J. G. Smeggil
United Technology Research
Center
East Hartford, CT 06108

R. W. Soderquist
Pratt & Whitney Group
400 Main Street (165-03)
East Hartford, CT 06108

T. E. Strangman
Garrett Turbine Engine Company
111 South 24th Street
Phoenix, AZ 85034

Dr. John Stringer
Electric Power Research Inst.
P. O. Box 10412
3412 Hillview Avenue
Palo Alto, CA 94304

Mr. Thomas N. Strom
NASA Lewis Research Center
21000 Brookpark Road M/S 77-6
Cleveland, OH 44135

T. A. Taylor
Linde Division
Union Carbide Corporation
Indianapolis, IN 46224

Robert P. Tolokan
Brunswick Corporation
2000 Brunswick Lane
DeLand, FL 32724

F. C. Toriz
Rolls Royce, Inc.
1985 Phoenix Boulevard
Atlanta, GA 30349

Harvey E. Von Doering
Oxidation-Corrosion Lab.
Gas Turbine Department 55-337
General Electric Company
Schenectady, NY 12305

Donald Whicker
GM Research Laboratory
GM Technical Center
Warren, MI 48090

Prof. W. L. Worrell
University of Pennsylvania
School of Metallurgy and
Materials Science
Philadelphia, PA 19104

Dr. I. G. Wright
Battelle Memorial Institute
505 King Avenue
Columbus, OH 43201

Dr. T. Yonushonis
Cummins Engine Company, Inc.
Box 3005
Columbus, IN 47202

NASA Scientific And Tech. Info. Fac.
Attn: Acquisition Branch
Baltimore Washington Int'l
Airport
P. O. Box 8757
Baltimore, MD 21240 (25 copies)

Dr. Mark Van Roode
Solar Turbines, Inc.
2200 Pacific Highway
P. O. Box 85376
San Diego, CA 92138-5376

E. E. Bailey
AFAPL/DO
Wright Patterson AFB, OH 45433

NASA Lewis Research Center
Attn: Library (60-3)
21000 Brookpark Road
Cleveland, OH 44135 (2 copies)

NASA Lewis Research Center
Attn: Report Control Office (60-1)
21000 Brookpark Road
Cleveland, OH 44135

1. Report No.	2. Government Accession No.	3. Recipient's Catalog No.
NASA CR-180807		

4. Title and Subtitle	5. Report Date
Thermal Barrier Coating Life Prediction Model Development - Final Report	November 1988
	6. Performing Organization Code

7. Author(s)	8. Performing Organization Report No.
R.V. Hillery, B.H. Pilsner, R.L. McKnight, T.S. Cook, and M.S. Hartle	R87 AEB586
	10. Work Unit No.

9. Performing Organization Name and Address	11. Contract or Grant No.
General Electric Company Aircraft Engine Business Group Cincinnati, Ohio 45215-6301	NAS3-23943
	13. Type of Report and Period Covered
12. Sponsoring Agency Name and Address	Final Contractor Report
National Aeronautics and Space Administration Lewis Research Center 21000 Brookpark Road, Cleveland, Ohio 44135	14. Sponsoring Agency Code

15. Supplementary Notes

Project Manager: Dr. James A. Nesbitt
NASA Lewis Research Center
Cleveland, Ohio

16. Abstract

This report describes the work performed on a program to determine the predominant modes of degradation of a plasma sprayed thermal barrier coating system and to develop and verify life prediction models accounting for these degradation modes. The primary TBC system consisted of a low pressure plasma sprayed NiCrAlY bond coat, an air plasma sprayed ZrO_2-Y_2O_3 top coat, and a Rene' 80 substrate. The work was divided into three technical tasks.

It was established through a literature survey and through past experience that the primary failure mode that needed to be addressed was loss of the zirconia layer through spalling. Experiments were performed which showed that oxidation of the bond coat is a significant contributor to coating failure. It was evident from the test results that the species of oxide scale that is initially formed on the bond coat plays an instrumental role in coating degradation and failure. It was also shown that elevated temperature creep of the bond coat plays a role in coating failure.

Also as a part of the first task, several key properties of the bond coat and top coat were measured. These included tensile strength, elastic modulus, Poisson's ratio, and coefficient of thermal expansion. An empirical model was developed for predicting the test life of specimens with selected coating, specimen, and test condition variations.

In the second task, a coating life prediction model was developed based on the data from Task I experiments, results from thermomechanical experiments performed as part of Task II, and finite element analyses of the TBC system during thermal cycles. Both time-independent plastic flow and time-dependent creep deformation were included in the analyses. An inference method was used in the development of the model since the processes involved in TBC failure are not generally directly observable.

The effort in the third and final task attempted to verify the validity of the model developed in Task II. This was done by using the model to predict the test lives of several coating variations and specimen geometries, then comparing these predicted lives to experimentally determined test lives. It was found that the model correctly predicts trends, but that additional refinement is needed to accurately predict coating life.

17. Key Words (Suggested by Author(s))	18. Distribution Statement
Thermal Barrier Coating Life Prediction Methodology Failure Mechanisms Coating Properties	Unclassified - Unlimited

19. Security Classif. (of this report)	20. Security Classif. (of this page)	21. No. of Pages	22. Price*
Unclassified	Unclassified	142	

* For sale by the National Technical Information Service, Springfield, Virginia 22161